LONG-PERIOD GRATING PHOTONIC DEVICES FOR BIOSENSING

SENSITIVITY ENHANCED LONG-PERIOD FIBER GRATING BASED PHOTONIC DEVICES FOR BIOSENSING

By

JIAN YANG, M.SC. , B.SC.

A Thesis

Submitted to the School of Graduate Studies

in Partial Fulfillment of the Requirements

for the Degree

Doctor of Philosophy in Engineering Physics

McMaster University

DOCTOR OF PHILOSOPHY (2007) McMaster University

(Engineering Physics) Hamilton, Ontario

TITLE: Sensitivity Enhanced Long-Period Fiber Grating Based Photonic Devices for Biochemical Sensing

AUTHOR: Jian Yang, M.Sc. (Université Laval),
B.Sc. (Northeastern University)

SUPERVISOR: Professor Chang-Qing Xu, Professor Yingfu Li

NUMBER OF PAGES: xii, 117

ABSTRACT

Long-period fiber grating (LPG) sensors have been widely used as refractive index sensors due to their high sensitivity to the ambient refractive index change surrounding the fiber cladding of the LPG. Application of the LPG refractive index sensor has been found in chemical sensing and biochemical sensing, however for application of label-free dip and measure biosensors based on receptor immobilized LPG bio-sensor, the conventional fiber optic refractive index sensors are limited in the refractive index sensitivity, resolution, and operational range owing to the low sensitivity of the cladding mode effective index dependence on the ambient refractive index and the broad-spectrum feature of the LPG transmission spectrum. Low-cost, disposable fiber optic biochemical sensors with improved sensitivity, stability and resolution are needed to provide a high-sensitivity platform for immunology and DNA/aptamer biosensor.

In this work, a novel fiber optic biosensing platform based on the LPG and the LPG in-fiber Michelson interferometer is designed and fabricated. The sensitivity and operation range enhancement is optimized by modifying the fiber cladding structure through reducing the cladding layer radius and applying a high-refractive index overlay with appropriate refractive index and thickness. The resolution of the refractive index sensor is improved by adopting the LPG in-fiber Michelson interferometer which turns the wide-spectrum feature of the LPG transmission spectrum into a narrow spectrum feature on the reflection spectrum of the interferometer. The reflection spectrum nature of the LPG in-fiber Michelson interferometer turns the sensor head into a single-end optotrode. The optotrode coated with bio-recognition film thus physically constitutes a short piece of fiber with one section of cladding reduced fiber. With single strand DNA (ssDNA) immobilized on the surface of the fiber cladding through biotin-avidin bridge, detection of the antisense DNA for the immobilized ssDNA is demonstrated. Immunoassay based on capture of target antigen by covalently immobilized antibody shows that reduction of the fiber cladding not only improve the sensitivity of the long period grating in-fiber Michelson interferometric biosensor but also improves the assay time.

Acknowledgements

I would like to above all express my most sincere appreciation to my supervisors, Dr. Chang-Qing Xu and Dr. Yingfu Li, for giving me the chance to pursue my Ph. D. study with them, for bringing me knowledge from two completely different disciplines and guiding me to fuse them into a merging technology and providing me the freedom to exploiting and solving problem by myself. I would also like to thank them for their commitment in this new project, for the patience, encouragements and strong backup they gave to me at those most difficult times of this project and for their financial support during my Ph. D. study.

I would also like to appreciated Dr. Paul Jessop and Dr. Adrian H. Kitai for their guidance, comments, encouragement and willingness to serve in my supervisory committee. Special thanks would also go to Dr. Wei-Ping Huang for his insightful guidance and comment on the theoretical mode solving and simulation of multi-layer optical fiber waveguide.

I am deeply in debt to my colleagues, Dr. Wanguo Liang, Dr. Li Yang, Dr. Razvan Nutiui and Mr. Weian Zhao. Without their collaboration and help nothing can be achieved on such an inter-discipline project.

Thanks go to the staffs in the Center for Emerging Device and Technologies and Department of Engineering Physics; Dr. Zhilin Peng, Mrs. Doris Stevanovic, Dr. Doug Bruce, Mrs. Fran Allen, Mrs. Marilyn Marlow, and Mrs. Linda Wilson for their help and support in the past four years.

I would like to also extend my sincere thanks to all the former and current group members of Dr. Xu's group; Dr. Bo Chen, Dr. Honggang Yu, Mr. Jorge Fonseca Campos, Dr. Jiatong Luo, Mr. John Bracken, Mr. Jon Markle, Mr. Qingyang Xu, Mrs. Fangfang Zhang, Mrs. Juan Deng, Mr. Pawan Sahdus and Mr. Yi Gan for their friendship and help in my research. It is my great pleasure to work with them.

I should appreciate the Natural Sciences and Engineering Research Council of Canada for providing me the NSERC Postgraduate Scholarships for two-year period of time. Appreciation would also go to the Ontario Center of Excellence and the Ontario Photonic Consortium for their partial support of this project.

Finally, but most importantly, I would like to express my gratitude to my wife, Yan, for her support and understanding in my career and life. I own her and our lovely daughter, Diane so much time in the numerous night and weekends when I should stay with them. My gratitude also goes to my parents, Xiaoying Xu and Yuanyi Yang, for their continuous understanding, encouragement, and support in my life.

CONTENTS

List of Figures

List of Tables

Chapter 1
Introduction

The optical fiber based biosensor has made a big leap in the past decade due largely to the major advances made in optical fiber communications that have driven down the cost of high-quality fiber components. Since the optical fiber is of small size, chemically inert in harsh environments, immune to electromagnetic interference, and has the capability of signal multiplexing and carrying large amounts of information, the fiber optic biosensor has attracted much interest in many new areas of research.

In this work, a fiber optic long-period grating (LPG) based evanescent wave biosensor is studied both theoretically and experimentally. In this chapter, a brief overview of biosensors is given first, followed by the description of the current status of fiber optic biosensor research. Concluding the chapter is the motivation of this thesis followed by a list of research contributions, and finally an outline of this thesis is presented.

1.1 Introduction to Biosensors

1.1.1 General description of biosensors

Since its conception in the 1960s by the pioneering work of Clark [1], biosensors have attracted much interest as an important alternative to the conventional bio-analytic approaches.

According to the definition of Nutiu et al[2], "definition, a biosensor refers to an analytical device consisting of two important components: a molecular recognition element (MRE) for target (analyte) detection and a transducer that physically reports the MRE-analyte interaction." As illustrated by Figure 1.1, biosensors usually consist of two basic elements connected in series: a biological recognition element (reporter) and a physicochemical transducer. The biological recognition system translates the biological information of the analyte from the biochemical domain, usually an analyte concentration, into a chemical or physical output signal with a defined sensitivity. The function of the bio-recognition system in the sensor device is to provide the sensor with a high selectivity to the specific analytical information against the background of other biological, chemical and physical parameters. The physicochemical transducer in contact with the bio-recognition system transfers the chemical or physical output of the bio-recognition system into some other easy-to-measure physical signal, usually in the electrical or optical domain, for detection. Generally, biosensors are self-contained with all parts being packaged together in the same small unit.

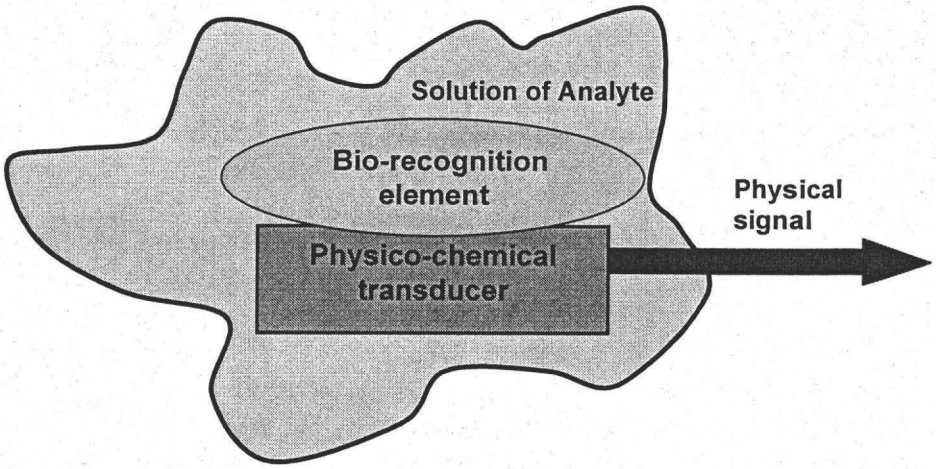

Figure 1.1 General structure of biosensor

The driving force for the development of biosensors is the ever present need for a simple, rapid and continuous in-situ measurement technique for a broad range of areas, e.g. medical, pharmaceutical, environmental, defense, bioprocessing, and food technology. Biosensors, because of their sensitivity, selectivity, versatility, ruggedness, and simultaneous multi-analyte monitoring capability, are regarded as an interesting alternative to conventional biosensing techniques. The applications of biosensors can be classified into three categories: health care, industrial process control, and environmental monitoring.

1.1.2 Classification of biosensors

Biosensors could be classified according to many different criteria, e.g. by the analyte, by the biological recognition mechanism, by the application, by the physicochemical transducer, etc. or a combination of any number of these. The most common criteria is the classification method suggested by the International Union of Pure and Applied Chemistry (IUPAC) [3], where the classification of biosensors are according to either the biological specificity conferring mechanism or to the mode of the signal transduction.

a. Classification according to the bio-recognition element

According to the biological recognition element (reporter), biosensors can be classified into two subcategories: biocatalytic recognition element sensors; and biocomplexing or bioaffinity recognition element sensors.

- Biocatalytic enzyme biosensors[4]: Biocatalytic biosensors, also called metabolism sensors, are based on a reaction catalyzed by an immobilized biocatalyst in which one or more analyte, also called substrate, interact and yield one or several products. The transient or steady state concentration of a transducer-detectable substance is measured to analyze the concentration of the analyte. Three types of biocatalysts are commonly used: Enzyme

(mono- or multi-enzyme); whole cell (micro-organisms); and tissues (plant or animal tissue slices).

- Affinity biosensors[5]. Affinity biosensors are based on the highly specific and strong binding of the immobilized reporter molecule with the analyte. In contrast to the catalytic biosensor, equilibrium is usually reached and there is no further net consumption of the analyte in the reaction. The chemical and/or physical property changes of the binding complexes are measured by the transducer. The most commonly used bioaffinity interaction systems are antibody-antigen interaction and nucleic acid conjugation.

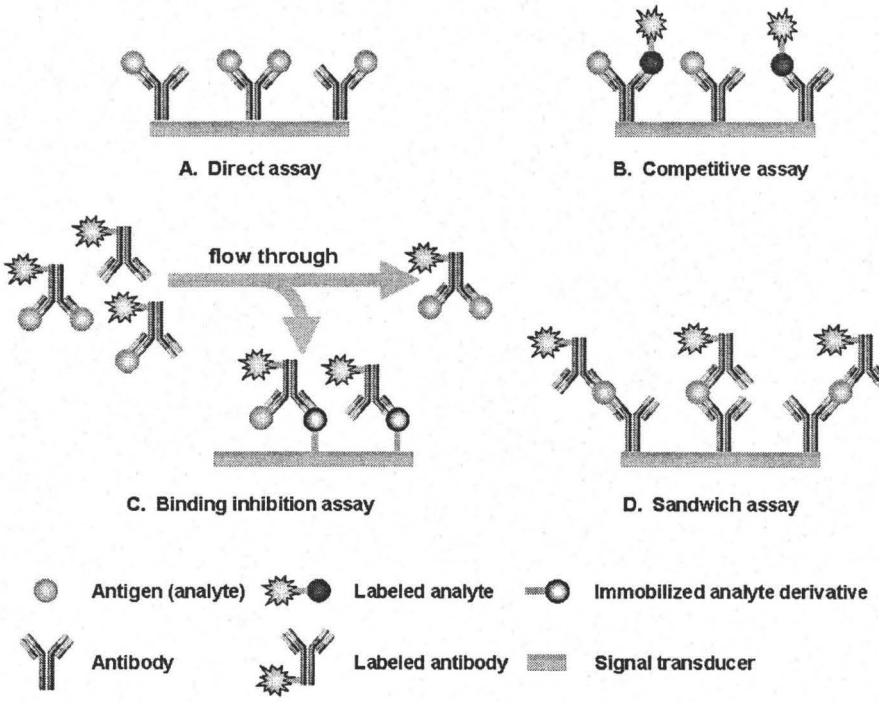

Figure 1.2 Assay formats employed in immunosensors: A. Direct assay; B. Competitive assay; C. binding inhibition assay; D. Sandwich assay.

Sensors utilizing the specific binding between antibody-antigen, also called immunosensors[6], are important and are the most developed class of biosensors. Immunosensors are based on the principle of solid-phase immunoassay in which either the antibody (or an analyte derivative) is immobilized on the signal transducer. The unique capacity of the antibody to bind specifically with the analyte of interest is the key factor in the immunosensor design. The higher the affinity of the antibody with the analyte, the higher the sensitivity the immunosensor can achieve. Figure 1.2 illustrates the frequently used assay format employed in immunosensors. In a direct assay (Figure 1.2 A), the antigen is directly bound to the antibody immobilized on the signal transducer and the interaction is monitored. The measured signal is a function of the amount of the antigen captured by the antibody. Competitive assay (Figure 1.2 B) is based on the competitive binding between the antigen (analyte) and an analyte derivative which is either labeled or immobilized to the limited number of binding sites provided by the

immobilized antibody. As another alternative, in a binding inhibition assay (Figure 1.2 C), the antibody and antigen is incubated first to form the antigen-antibody complex. The solution is then flow through the transducer immobilized with the antigen derivative. Only the unbounded antibody will bind to the transducer surface and thus produce a signal. In sandwich assay (Figure 1.2 D), the antigens are incubated with an excessive amount of first type of immobilized antibody, the antibody-antigen complex is then incubated in a second labeled antibody. The labeled antibody binds to the antigen at a second antigenic site and thus the amount of labeled antibody bounded to the transducer surface is related to the amount of the antigen (analyte) concentration.

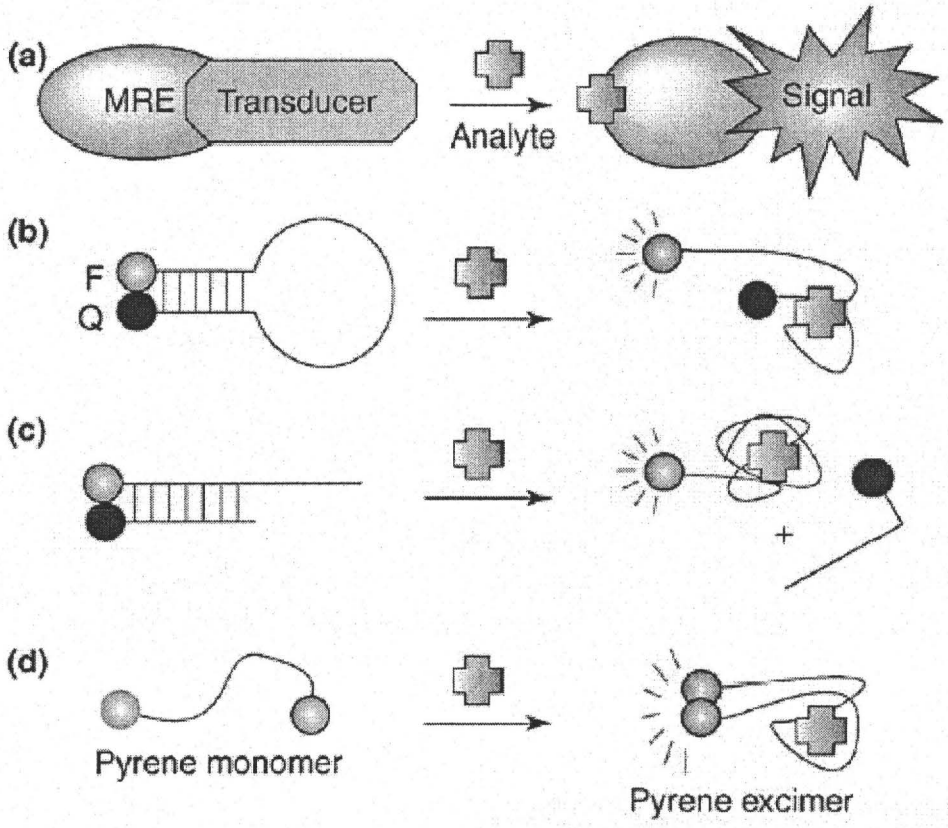

Figure 1.3 Sensing strategy employing in nucleic acid based biosensor [7].

Nucleic acid biosensors are based on specific affinity reactions involving DNA molecules. Some of this type of biosensors detects DNA or RNA targets due to their inherent ability to form Warson-Crick duplex. Beyond the detection of nucleic acid target, certain single strand DNA or RNA molecules termed "aptamer" can form defined terriary structure for binding nonnucleic acid targets. Over the past decade, it is becoming more and more apparent that DNA and RNA aptamers represent a ney type of molecular recognition elements for detection of a large variety of target molecule such as protein and metabolites. The format of the nucleic acid biosensor can be illustrated by the Figure 1.3 recently published by Navani *et al.* [7]. As shown in Figure 1.3 a, in a general nucleic acid biosensor format the immobilized oligonucleotide (single-strand DNA,

standard molecular beacon or aptamer) bind to the analyte (complementary DNA) and a signal is produced in the transducer. In the aptamer beacon format (Figure 1.3 b), an aptamer with one end labeled with a fluorophore (F) and the other end labeled with a quencher (Q) is designed into a hairpin structure. When the aptamer beacon captures the target, the Q and F at the pinpoint of the hairpin is separated and result in emission of fluorescence. In the structure-switching signaling aptamer format (Figure 1.3c), the sensing aptamer with one end immobilized on the transducer and the other end labeled with fluorophore is bonded with its antisense DNA. When the aptamer binds with its target, the structure of the DNA duplex structure is switched to the aptamer-target complex and the antisense DNA is pushed away with the quencher and a fluorescence signal is induced. As illustrated in Figure 1.3 d, in excimer aptamer format an aptamer is labeled with two pyrene molecules (monomer) at the two ends of the aptamer. Target binding facilitates the transformation of the monomer into an excimer, which emits fluorescence at a different wavelength and with different fluorescence life time as compared to the monomer.

b. Classification according to the physicochemical transducer

Biosensors may be classified according to the operation principle of the physico-chemical transducer [8-10]. In such a way the biosensor can be classified into four categories:

1) Electrochemical biosensors transform the effect of the electrochemical interaction from the analyte to the electrode as a useful signal. This category of biosensor includes four subcategories: potentialmetric biosensors[11-13]; amperometric biosensors[14]; conductance biosensors[15, 16]; capacitive biosensors[17].

2) Mass sensitive biosensors transform the mass change at a specially modified surface into a change of a property of the support material. The mass change is caused by the biorecogntion that happens on the transducer surface. The mass sensitive biosensor can be divided into three sub-categories: Piezoelectric biosensors[18, 19]; surface acoustic wave biosensors; micro cantilever biosensors[20-22].

3) Thermometric biosensors are based on the measurement of the heat of a specific biochemical reaction or absorption which involves the analyte. In this type of biosensor, the heat may be measured by a thermistor, or a pyroelectric or optothermal transducer.

4) Optical biosensors [23] detect optical changes, which are the result of the interaction between the BRE and the analyte. Optical biosensors are a large category of biosensor and may be further subdivided according to the type of optical properties, which have been applied in the biosensor: absorbance, reflectance, luminescence, fluorescence, refractive index change, optothermal effect, or light scattering.

1.2 Fiber Optic Biosensors

Fiber optic biosensors are optical biosensors in which optical fibers are used as part of the sensor structure. Soon after the invention of laser [24] and modern low-loss optical fibers [25], optical fibers have been used in chemical sensor structures. Since then the study and application of the fiber optic sensor has extended to health care, industrial processing, environmental monitoring and military applications. In fact for almost all sensing schemes where optical bio-sensing is employed, optical fibers can be found in the sensor design.

The wide application and acceptance of optical fibers for biosensors are because they can be used in very harsh or sensitive measurement environments, where use of a conventional sensor is neither available nor appropriate. Fiber optic sensors are compact and light weight, minimally invasive, immune to electromagnetic interference, require no electrical currents flowing at the sensing point, and can be multiplexed with a single optical fiber. The advantages of using optical fibers in biosensors are listed below [4]:

1. There are many optical phenomenon-based methods available for chemical analysis;
2. Due to the extremely low propagation loss of optical fibers, optical light waves can be transmitted over long distances without being seriously attenuated, enabling remote sensing without signal boosting;
3. Because of the high bandwidth provided by optical fibers, light waves with different wavelengths can be propagated in the same fiber simultaneously. Optical fibers can thus carry much more information than electrical wires, permitting multiplexing of sensing elements.
4. Optical fibers are compact and light weight and allow for easy miniaturization at low cost.
5. Optical fibers are chemically inert and durable, therefore chemically compatible with many bio-reagents, and thus have strong potential for in-*vivo* applications.
6. The high carrier frequency nature of optical fibers makes optical fiber biosensors immune to electromagnetic interference.
7. In the case of evanescent wave biosensing, the light wave in the analyte is highly bound to the proximity of the fiber waveguide and enables surface-specific analysis possible. In free space configuration, surface analysis is hard to realize and suffers from low signal to noise ratio (SNR).

Fiber optic biosensors can be classified into different categories according to different criteria. For example, based on whether the interaction between the light wave and the analyte happen within a element of the optical fiber, fiber optic biosensors can be classified into intrinsic fiber optic biosensors and extrinsic fiber optic biosensors. Alternatively, fiber optic biosensors can be categorized according to the classification of optical sensing mechanism given in section 1.1, i.e. absorbance, reflectance, luminescence, fluorescence, refractive index change, etc.. Among all optical phenomena utilized, fluorescence based and refractive index based fiber optic biosensors are most common.

Fluorescence is a luminescence optical phenomenon in cold bodies, in which the molecular absorption of a photon triggers the emission of another photon with a longer

wavelength. Fluorescence is widely used in biotechnology and thus is highly developed. The sensing scheme used in fluorescence based fiber optic biosensors can be categorized into two classes[26]: optrode based fiber optic biosensors and evanescent wave fiber optic biosensors.

In optrode based fiber optic biosensors, a BRE is immobilized on the end of an optical fiber. The excitation light is delivered from a light source to the BRE, and the light emitted from the BRE is then transmitted back to the photo detector via the same fiber or a different fiber [23]. The small dimension of the optrode biosensor allows measurement in very small sample volumes. Optrode biosensors have been miniaturized to submicron dimension for monitoring biomolecule concentrations inside a living cell [27].

Evanescent wave fluorescent fiber optic biosensors [23], also called Total Internal Reflection Fluorescence (TIRF) fiber sensors, are based on the evanescent field of the fiber guided light wave. The BRE is immobilized on the surface of the fiber core, where the light field of the guided mode is reflected due to total internal reflection at the core surface. The evanescent wave field couples light out of the fiber into the surrounding medium and thereby excite fluorophores bounded to or in close proximity to the fiber core surface within the penetration depth. Vice versa, the emission light from the BRE is coupled to the fiber core through the evanescent wave as well. The result of the excitation and emission coupling through the evanescent wave is that the sensor is relatively immune from interference in the bulk solution.

Refractive index based fiber optic biosensors rely on the change of the refractive index of the BRE upon bio-recognition. Refractive index change is the intrinsic physicochemical change associated with the bio-recognition thus labeling is not required, which in many applications is either inappropriate or interferes with the bio-recognition system. The most common types of refractive index based fiber optic biosensor are based on either of two sensing schemes: surface plasmon resonance (SPR), or wave coupling via a fiber grating.

Surface plasma resonance (SPR) [28] is a charge-density oscillation that may exist at the interface of two media with dielectric constants of opposite signs, for instance, a metal and a dielectric. The charge density wave is associated with the electromagnetic waves, the field vectors of which reach their maxima at the interface and decay exponentially into both media. This surface plasma wave (SPW) is a TM-polarized wave. The electromagnetic field of an SPW is distributed in a highly asymmetric fashion and the vast majority of the field is concentrated in the dielectric. Owing to high loss in the metal, the SPW propagates with high attenuation in the visible and near-infrared spectral regions. Excitation of SPW happens when the electromagnetic momentum of the excitation optical field matches the propagation constant of the SPW through the coupling mechanism; resonant transfer of energy from the optical excitation field to the SPW occurs and the absorption of the optical wave is observed. The high amplitude existence of the evanescent field in the dielectric makes the propagation constant of the SPW, and thus the resonance condition of SPR, very sensitive to the media adjacent to the metal film. In SPR biosensors, the dielectric adjacent to the metal film is the BRE, which changes its reflective index upon biorecognition and can be interrogated by the reflection amplitude at the resonance point, the angular spectrum of the excitation light, or the wavelength spectrum. SPR has been widely accepted in biological analysis and is

currently commercially available. Miniaturization efforts of the SPR biosensor were focused on realizing a fiber optic configuration. Optical fiber based SPR sensors represent the highest level of miniaturization of SPR devices, which allows for bio-sensing with minimal sample volume. Multimode fiber (MMF) SPR sensors based on white-light reflection spectra from SPR on structure modified fiber tips [29] and selective excitation of high order modes to excite a SPW either on the fiber cladding or on the fiber core [30, 31] have been studied. MMF SPR sensors, however, were not adopted in biosensing largely due to the instability in higher order mode excitation. Recently, fiber optic SPR sensors based on single mode fibers have been developed. In this type of configuration, the cladding of a single mode fiber is side-polished to expose the fiber core and a thin film of metal overlay is deposited on the polished surface. The surface plasmon is excited by the core mode of the single mode optical fiber [32]. However, given the TM mode nature of SPR, this type of fiber optic SPR sensor requires a reliable control of the polarization of the light propagating in the core [28]. Despite the large amount of biosensors based on SPR, to our knowledge no research on fiber optic SPR based biosensors has been reported.

1.3 Evanescent field based fiber grating sensor

A fiber grating is formed by inducing a periodic refractive index perturbation along the length of an optical fiber. The periodic perturbation of the refractive index diffracts the light wave propagating in the fiber into other mode(s) of propagation in a wavelength selective way. Besides the general advantages inherent in fiber optic sensors, the principle advantage of fiber grating based devices is that the measurand information is wavelength encoded, which is an absolute quantity and thereby making them self-referencing and thus immune to connection loss and fluctuations of the light source output level. For this reason fiber grating sensors have been extensively used in the measurement of strain, displacement, temperature, vibration and acoustic wave, pressure, refractive index, and chemical/biochemical parameters [33-35]. Label-free fiber grating biosensors are based on measurement of the BRE refractive index change with a fiber grating based refractometer.

The first study of fiber gratings for refractive index sensors was carried out by Bhatia *et al.* [36]. In their pioneering work, the dependence on ambient refractive index (RI) of a fiber optic LPG was studied. The LPG is a type of fiber grating for which the period of the refractive index perturbation is in the range between 100 μm and 500 μm. The LPG couples the fiber core mode to co-propagating cladding modes in a wavelength dependent manner. Coupling occurs when phase matching between the core mode and a cladding mode is satisfied with the assist of the periodical perturbation. Because of the direct contact of the cladding mode with the ambient medium, the effective index of the cladding is dependent on the RI of the ambient. LPG sensors may thus demonstrate high sensitivity to ambient RI. Patrick *et al.* [37] studied in detail the dependence of the sensitivity of a LPG RI sensor to the grating period and demonstrated its application as a chemical sensor. It was shown that the phase matching condition of a long period grating

is sensitive to the change in the ambient RI and can thus be used as a refractive index sensor in the range of n = 1.3~1.43. It is also observed that, the sensitivity of LPG RI sensor is a function of the grating period and the order of the resonant cladding modes. When the order and wavelength of the cladding mode resonance are large, the wavelength shift sensitivity is high. However, since the response of the cladding mode to the ambient RI is nonlinear, high sensitivity operation of the LPG RI sensor is located in a very limited RI range between $n = 1.40$ and $n = 1.44$.

Three types of techniques were utilized to improve the sensitivity of LPG refractive index sensors.

In the first technique, the dispersion characteristic of the phase matching curve (PMC) was utilized by Shu *et al.* [38] , Wang *et al.* [39] and Chen *et a.l* [40].. In their study, the grating period and the DC component of the refractive index modulation in the fiber core was carefully tuned so that the of PMC crosses the horizontal axis at the turn around point (TAP) where the phase matching wavelength is highly sensitive to refractive index due to the small slope of the PMC at TAP. The main drawback of this technique is that careful control of the grating period and the index modulation amplitude is simultaneously required, which is in practice difficult to maintain after the LPG is annealed in the fabrication process.

In the second type of sensitivity enhancement technique, the cladding layer diameter is reduced [41-43]. In this technique, hydrofluoric acid was used to partially etch away the cladding layer in order to decrease the normalized frequency of the cladding modes. Because the slope of the dispersion curve is higher when the normalized frequency is small, the dependence of cladding modes' effective indexes on the ambient RI is enhanced, which in turn boosts the sensitivity of the LPG to the ambient RI.

In the third sensitivity enhancement technique, a high RI overlay is deposited on top of the fiber cladding in order to promote cladding mode evanescence. Ree *et al.* [44] found that by changing the thickness of a high refractive index overlay on the cladding layer (deposited by the Langmuir-Blodgett method), tuning of the resonance band wavelength can be achieved. This effect quickly ignited intensive theoretical and experimental studies by other researchers and has been employed as a method to enhance the sensitivity of the LPG RI sensor [45-52]. Unlike the LPG RI sensors based on pristine fibers which are of high sensitivity only in the index range of $n = 1.40 \sim 1.44$, application of a high RI overlay not only enhances the sensitivity of LPG RI sensor, but also enables tuning of the high sensitivity range from $n = 1.00$ to $n = 1.44$. This is very important in bio-sensing applications, since the BRE film or the supporting membrane of the BRE quite often have RI lower than 1.4.

Soon after the initial study of the LPG RI sensor, the RI sensing mechanism was utilized for chemical/biochemical sensing. Delisa *et al.* studied the application of LPG in immunosensors based on antibody-antigen affinity binding [53]. In their study, Goat anti-human IgG (antibody) was immobilized on the cladding surface of a fiber inscribed with a LPG, and detection of the specific antibody-antigen binding was investigated. Human IgG binding was observed to be concentration dependent over a range of 2 - 100 $\mu g \cdot mL^{-1}$, and equilibrium bound antigen levels could be attained in approximately 5 min using an initial rate determination.

Subsequently, research on LPG based biosensors was focused on improving the performance in two aspects: enhance the sensitivity of the LPG biosensor in the RI change of the BRE and improve resolution of the spectroscopic signal.

Martin [54] used a composite film of TiO_2 nanoparticles and dextran hydrogel to improve the performance of the LPG antibody-antigen affinity biosensor. In the composite film the dextran hydrogel functions as a support for the nanoparticles, while the nanoparticles themselves provide higher antibody grafting surface area and raise the RI of the composite film, thereby increasing the sensitivity of the LPG sensor upon biorecognition. In a similar work, Tang *et al.* [55], modified the surface of the LPG with self-assembled gold colloids. The colloidal gold surface was then modified with a dinitrophenyl compound (DNP). Experimental results showed that the signal increased linearly with increasing analyte concentration, and the detection limit of the sensor for anti-DNP of 1 nM (9.5×10^{-10}) was demonstrated. The above mentioned LPG biosensors were all two-port devices needing lead-in and output fibers in operation. Such a configuration limits the operation of the sensor, since the simple design of micro-fluid control systems require single-ended detecting device. Jone *et al.* from Luna Innovations, Inc. issued a patent for a new design to turn the LPG sensor into a single-ended sensing device [56] utilizing a cladding mode stripper and a metallic reflector at the fiber tip. This configuration results in the reflection of the light wave in the fiber core back to the lead-in fiber.

Another approach for enhancing sensitivity of the LPG sensors is to improve on the signal interrogation method, and thus the resolution of the LPG spectrum. The broad-band nature of the resonance notch structure in the LPG transmission spectrum results in a high uncertainty in determining the notch wavelength. This drawback of LPG sensors can be overcome by incorporating an in-fiber interferometer in the device configuration. A LPG in-fiber Mach-Zehnder (M-Z) interferometer, first proposed by Dianov *et al.* in 1996 [57], was fabricated by forming two identical LPGs in series in an optical fiber. The LPGs function analogously to beam splitters of a conventional M-Z interferometer, with the core and cladding of the fiber functioning as the interferometer arms. The narrow features in the interference spectrum of the LPG in-fiber M-Z interferometer make it a very attractive device for RI sensing. In addition, the phase carrier modulation characteristic of the LPG in-fiber M-Z interferometer allows interrogation of the interference fringes with the heterodyne interrogation technique [58, 59]. Similar to the conversion of a two-port device into a single-ended optical probe in the single LPG sensor, Swart and his colleagues [60, 61] transformed the LPG in-fiber M-Z interferometer into a Michelson interferometer by replacing the second LPG with a high reflectivity metallic mirror.

Again, like the single LPG refractive index sensor, enhancement of the LPG in-fiber interferometer sensitivity is achieved by exploiting the cladding mode dependence on the cladding structure. Allsop *et al.* [62, 63] and Ding *et al.* [64] reduced the cladding diameter of the M-Z interferometer in order to strengthen the dependence of cladding mode effective index on the ambient RI, and thus enhance the phase shift of the interference spectrum. Most recently, James *et al.* [65] deposited a high RI overlay on the fiber cladding between the LPGs of the M-Z in-fiber interferometer. The turn-around-point technique used for enhancing sensitivity of the single LPG refractive index

sensor is not applicable in in-fiber interferometers since phase matching is not required in interferometry technology.

Despite the intensive study of the LPG in-fiber interferometer as a refractive index sensor, application of the LPG in-fiber M-Z interferometer as a biosensor has not yet been reported largely due to the drawbacks associated with two-ended optical fiber devices. Recently, almost in parallel to our work, Kim *et al.* [66] reported immobilization of rabbit immunoglobulin G (rabbit IgG) on the cladding layer of a LPG in-fiber Michelson interferometer which was subsequently used as an immunosensor. A fringe's shift towards shorter wavelength of $0.55nm$ was observed when the immobilized rabbit IgG captured its antisense (anti-rabbit IgG).

1.4 Motivation

The application of biotechnology in fields such as clinical diagnosis, pharmaceutical analysis and drug screening, environmental monitoring, and warfare chemical detection demands high sensitivity, high specificity, and *in situ* and fast detection biosensors of low cost and easy operation. Most conventional biosensors rely on a label attached to the bio-recognition system, typically a fluorescent dye. While labeling techniques have been successful, they require extra steps in sample preparation and in some cases bring in cross interactions. As previously stated in this chapter, despite the success of its application in laboratory analysis, label-free SPR biosensors based on RI measurement is too expensive for many applications. The planar waveguide nature of SPR makes both the sensing device and the interrogation system expensive to manufacture. Fiber-optic SPR biosensors have not been commercially implemented due to difficulties in device fabrication and operation.

In this thesis, fiber optic label-free biosensors based on LPG technology are studied. The target of this study is to 1) improve the performance of the LPG based RI sensor as a platform for biosensors by enhancing the sensitivity, spectral resolution and stability of the sensor device; and 2) engineer the device into a low cost single-end disposable fiber probe. The sensitivity of the LPG based RI sensor is enhanced by increasing the dependence of the cladding mode effective index on the ambient RI via modification of the fiber cladding structure, which includes high RI overlay deposition and cladding reduction. The LPG in-fiber Michelson interferometer configuration is adopted to enhance the spectral resolution of the sensor through fringe formation while converting the sensor into a single-ended probe.

1.5 Outline of thesis

In Chapter 2, mode theory for optical fibers along with the operating principles of optical long period fiber gratings are presented. A brief introduction of the working principles of LPG in-fiber interferometers is also given. Using the full-vector electromagnetic wave model, Chapter 3 presents a study of the enhancement of cladding

mode effective index dependence on ambient RI by forming a high RI overlay and reducing the cladding diameter. The enhancement of the sensitivity and expansion of operational range of the LPG RI sensor based on this cladding structure modification is then investigated. In Chapter 4, a cladding-reduced LPG interferometer is experimental constructed and experimentally examined. Chemical modification of the fiber surface and subsequent immobilization of antibody and single strand DNA on the fiber cladding is discussed in Chapter 5. A biosensor consisting of covalently immobilized antibodies as the BRE and a cladding-structure-modified LPG in-fiber Michelson interferometer is demonstrated. In Chapter 6, a conclusion of this research is drawn and future works are discussed.

Chapter 2
Optical Fiber Mode and Long Period Fiber Grating

The optical fiber is regarded to be one of the most important inventions of the 20th century. As suggested by Kao and Hockham [25] during the early development stages, the optical fiber has emerged to become undeniably the most important transmission medium for light wave delivery, and has revolutionized modern communications and optical science. In 1978, Hill *et al.* [67] demonstrated the formation of a permanent grating in an optical fiber by launching an intense Argon laser beam into a germanium (Ge) doped optical fiber, thereby generating a periodic refractive index modulation within the fiber core. Their method of grating inscription was later simplified and made more versatile by Meltz *et al.* [68] who used holographic illumination through the side of the fiber cladding to form the refractive index modulation within the core. Fiber gratings with periods in the order of 100 μm was found to be an effective method of coupling the input light wave to different modes and polarizations within the fiber waveguide [69].

This chapter is devoted to developing the fundamental theoretical framework for obtaining the core and cladding mode solutions of multi-layer dielectric fiber waveguides, as well as to the application of the couple mode theory in the study of long period gratings in optical fibers.

2.1 General description of an optical fiber

An optical fiber is a cylindrical dielectric waveguide which allows low loss propagation for optical frequency electromagnetic (EM) waves. EM waves in the fiber core are confined by the differential refractive index of the core and cladding; total internal reflection occurs at the interface between the high refractive index core and the low refractive index cladding. Similarly, propagation of modes within the cladding occurs by total internal reflection at the cladding-ambient interface. The core and cladding mode solutions can be obtained by modeling the fiber as a stratified cylindrical multilayer dielectric waveguide. An analytic full-vector optical fiber mode solver based on a transfer matrix method will be given.

2.1.1 Optical light waves in cylindrical dielectric waveguides [70]

Consider a cylindrical dielectric waveguide with a step-index profile as in Fig. 2.1. The radial distribution of the fiber refractive index is:

$$n(r)=\begin{cases} n_1 & 0<r<r_1 \\ n_2 & r_1<r<r_2 \\ \vdots & \\ n_{N-1} & r_{N-2}<r<r_{N-1} \\ n_N & r_{N-1}<r \end{cases} \tag{2.1}$$

where n_i and r_i are the refractive index of the i^{th} layer of the waveguide and r is the radius.

From waveguide theory, Maxwell's equations (in a cylindrical coordinate system) dictate that the azimuthal and radial components of the electric and magnetic fields for a uniform medium can be expressed in terms of the longitudinal components of the electric and magnetic fields as

$$E_r=-\frac{j}{q^2}\left(\beta\frac{\partial E_z}{\partial r}+\frac{\mu\omega}{r}\frac{\partial H_z}{\partial \phi}\right) \tag{2.2a}$$

$$E_\phi=-\frac{j}{q^2}\left(\frac{\beta}{r}\frac{\partial E_z}{\partial \phi}-\mu\omega\frac{\partial H_z}{\partial r}\right) \tag{2.2b}$$

$$H_r=-\frac{j}{q^2}\left(\beta\frac{\partial H_z}{\partial r}-\frac{\omega\varepsilon}{r}\frac{\partial E_z}{\partial \phi}\right) \tag{2.2c}$$

$$H_\phi=-\frac{j}{q^2}\left(\frac{\beta}{r}\frac{\partial H_z}{\partial \phi}+\omega\varepsilon\frac{\partial E_z}{\partial r}\right) \tag{2.2d}$$

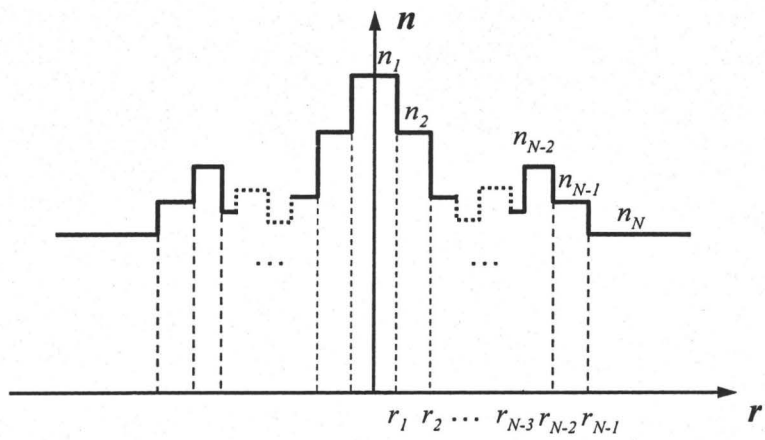

Figure 2.1 Radial index profile of an N-layer straight optical fiber

where $\beta = n_{eff} k_0$ is the propagation constant, n_{eff} is the effective index, $k_0 = \frac{2\pi}{\lambda}$ is the wave number in vacuum, ω is the angular frequency of the light wave, μ is the permeability of the medium, $\varepsilon = \varepsilon_r \varepsilon_0 = n^2 \varepsilon_0$ is the permittivity of the dielectric medium, ε_0 is the permittivity of free space, and $q^2 = \omega^2 \mu\varepsilon - \beta^2 = n^2 k_0^2 - \beta^2$.

The EM wave propagates along the length of the optical fiber, so that every field component has the form

$$\psi(r,\phi,z,t) = \psi_0(r) e^{jv\phi} \cdot e^{j(\omega t - \beta z)} \tag{2.3}$$

Where $\psi_0(r)$ is the radial distribution of the EM wave, $e^{jv\phi}$ is the azimuthal distribution of the EM wave, v the azimuthal mode number of the EM wave and take the value of non-negative integers.

The longitudinal components of the electric and magnetic fields, $E_z(r,\phi)$ and $H_z(r,\phi)$ satisfy the wave equations:

$$\frac{\partial^2 E_z}{\partial r^2} + \frac{1}{r}\frac{\partial E_z}{\partial r} + \frac{1}{r^2}\frac{\partial^2 E_z}{\partial \phi^2} + q^2 E_z = 0 \tag{2.4a}$$

$$\frac{\partial^2 H_z}{\partial r^2} + \frac{1}{r}\frac{\partial H_z}{\partial r} + \frac{1}{r^2}\frac{\partial^2 H_z}{\partial \phi^2} + q^2 H_z = 0 \tag{2.4b}$$

Given the fact that the wave equations for $E_z(r,\phi)$ and $H_z(r,\phi)$ take the same form, they can be mathematically represented by the same function. Substituting Eq. 2.3 into Eq. 2.4, results in the following equation for:

$$\frac{\partial^2 F_1}{\partial r^2} + \frac{1}{r}\frac{\partial F_1}{\partial r} + \left(q^2 - \frac{\upsilon^2}{r^2}\right) F_1 = 0. \tag{2.5}$$

Eq.2.5 is the well known Bessel Equation.

When $n^2 k_0^2 > \beta^2$, i.e. $q^2 > 0$, the solutions are the Bessel functions of the first and second kind:

$$F_1(r) = AJ_\upsilon(ur) + BY_\upsilon(ur), \tag{2.6}$$

where $u^2 = n^2 k_0^2 - \beta^2$ is the transverse propagation constant of the EM wave.

When $n^2 k_0^2 < \beta^2$, i.e. $q^2 < 0$, the solutions are modified Bessel functions of the first and second kind:

$$F_1(r) = AI_\upsilon(wr) + BK_\upsilon(wr) \tag{2.7}$$

where $w^2 = \beta^2 - n^2 k_0^2$ is now the transverse propagation constant of the EM wave.

According to the properties of the Bessel functions, allowing the propagation constants to be complex numbers results in both of the above situations being described as Eq. 2.6 for which $w = iu$. In the following discussion, we will use Eq. 2.6, as the field

expression, and use and expression in the form of Eq. 2.7 for the outermost layer only in order to emphasize the decay of the evanescent wave there.

By substitution of Eq. 2.6 into Eq. 2.2, the electric and magnetic fields of the light wave in the i^{th} layer of the stratified cylindrical waveguide can be expressed as:

$$E_z(r)=\left[A_i J_v(u_i r)+B_i Y_v(u_i r)\right]e^{jv\phi} \tag{2.8a}$$

$$E_r(r)=\left[-\frac{j\beta}{u_i}J'_v(u_i r)\cdot A_i-\frac{j\beta}{u_i}Y'_v(u_i r)\cdot B_i+\frac{vk_0 z}{u_i^2 r}J_v(ur)\cdot C_i+\frac{vk_0 z}{u_i^2 r}Y_v(u_i r)\cdot D_i\right]e^{jv\phi} \tag{2.8b}$$

$$E_\phi(r)=\left[\frac{\beta v}{u_i^2 r}J_v(u_i r)\cdot A_i+\frac{\beta v}{u_i^2 r}Y_v(u_i r)\cdot B_i+\frac{jk_0 z}{u_i}J'_v(u_i r)\cdot C_i+\frac{jk_0 z}{u_i}Y'_v(u_i r)\cdot D_i\right]e^{jv\phi} \tag{2.8c}$$

and

$$H_z(r)=\left[C_i J_v(u_i r)+D_i Y_v(u_i r)\right]e^{jv\phi} \tag{2.9a}$$

$$H_r(r)=\left(-\frac{j\beta}{u_i}J'_v(u_i r)\cdot C_i-\frac{j\beta}{u_i}Y'_v(u_i r)D_i-\frac{vk_0 n_i^2}{zru_i^2}J_v(u_i r)A_i-\frac{vk_0 n_i^2}{zru_i^2}Y_v(u_i r)B_i\right)e^{jv\phi} \tag{2.9b}$$

$$H_\phi(r)=\left(-\frac{j\beta v}{u_i^2 r}J_v(u_i r)\cdot C_i-\frac{j\beta v}{u_i^2 r}Y_v(u_i r)\cdot D_i+\frac{jk_0 n_i^2}{uz}J'_v(u_i r)\cdot A_i+\frac{jk_0 n_i^2}{uz}Y'_v(u_i r)\cdot B_i\right)e^{jv\phi} \tag{2.9c}$$

where $\mu\omega = k_0 z$ and z = 377Ω.

The boundary conditions at $r=r_i$ are that the tangential components of the electric and magnetic fields, E_z, H_z, E_ϕ and H_ϕ are continuous at the interface. In the following section we will apply a 4×4 transfer matrix method in order to find the solutions of the light wave with the above mentioned boundary conditions.

2.1.2 Mode solving with transfer matrix method [70]

Consider a field strength vector consisting of the tangential components of the EM wave, H_z, H_ϕ, E_z, and E_ϕ, in the *i*th layer of the cylindrical waveguide:

$$F(r)=\begin{pmatrix}E_z(r)\\H_z(r)\\E_\phi(r)\\H_\phi(r)\end{pmatrix} \tag{2.10}$$

along with the field coefficient vector in the *i*th layer, written as:

$$COE^i=\begin{pmatrix}A_i\\B_i\\C_i\\D_i\end{pmatrix}. \tag{2.11}$$

The field strength vector can be expressed as the product of a matrix of Bessel functions, and the coefficient vector:

$$\begin{pmatrix} E_z(r) \\ H_z(r) \\ E_\phi(r) \\ H_\phi(r) \end{pmatrix} = \begin{pmatrix} J_\nu(u_i r) & Y_\nu(u_i r) & 0 & 0 \\ 0 & 0 & J_\nu(u_i r) & Y_\nu(u_i r) \\ \frac{\beta\nu}{u_i^2 r} J_\nu(u_i r) & \frac{\beta\nu}{u_i^2 r} Y_\nu(u_i r) & \frac{jk_0 z}{u_i} J'_\nu(u_i r) & \frac{jk_0 z}{u_i} Y'_\nu(u_i r) \\ -\frac{jk_0 n_i^2}{u_i z} J'_\nu(u_i r) & -\frac{jk_0 n_i^2}{u_i z} Y'_\nu(u_i r) & \frac{j\beta\nu}{u_i^2 r} J_\nu(u_i r) & \frac{j\beta\nu}{u_i^2 r} Y_\nu(u_i r) \end{pmatrix} \begin{pmatrix} A_i \\ B_i \\ C_i \\ D_i \end{pmatrix}. \quad (2.12)$$

Order:

$$M_i = \begin{pmatrix} J_\nu(u_i r) & Y_\nu(u_i r) & 0 & 0 \\ 0 & 0 & J_\nu(u_i r) & Y_\nu(u_i r) \\ \frac{\beta\nu}{u_i^2 r} J_\nu(u_i r) & \frac{\beta\nu}{u_i^2 r} Y_\nu(u_i r) & \frac{jk_0 z}{u_i} J'_\nu(u_i r) & \frac{jk_0 z}{u_i} Y'_\nu(u_i r) \\ -\frac{jk_0 n_i^2}{u_i z} J'_\nu(u_i r) & -\frac{jk_0 n_i^2}{u_i z} Y'_\nu(u_i r) & \frac{j\beta\nu}{u_i^2 r} J_\nu(u_i r) & \frac{j\beta\nu}{u_i^2 r} Y_\nu(u_i r) \end{pmatrix} \quad (2.13)$$

Eq. 2.12 can now be written as:

$$F(r) = M_i(r) \cdot COE_i \quad (2.14)$$

At the two interfaces of the i^{th} layer, r_{i-1} and r_i, the field expressions are:

$$F^i(r_i) = M_i(r_i) COE^i \quad (2.15)$$

$$F^i(r_{i-1}) = M_i(r_{i-1}) COE^i \quad (2.16)$$

We can relate the field strength $F^i(r_i)$ to $F^i(r_{i-1})$ by eliminating the coefficient vector from Eqs. 2.15 and 2.16 to give

$$F^i(r_i) = M_i(r_i) M_i^{-1}(r_{i-1}) F^i(r_{i-1}) \quad (2.17)$$

By defining a new matrix, $T_i(r_i, r_{i-1})$,

$$T_i(r_i, r_{i-1}) = M_i(r_i) M_i^{-1}(r_{i-1}), \quad (2.18)$$

Eq. 2.17 becomes

$$F^i(r_i) = T_i(r_i, r_{i-1}) F^i(r_{i-1}). \quad (2.19)$$

The boundary conditions for the EM field require the continuity of the tangential components at the interface of the two dielectric media, i.e. the interface between the two layers. This gives:

$$F^{i+1}(r_i) = F^i(r_i). \quad (2.20)$$

We can then omit the layer superscript i and write

$$F(r_i) = T_i(r_i, r_{i-1}) F(r_{i-1}). \quad (2.21)$$

By substituting the $(i-1)^{th}$ field expression into the i^{th} field expression and repeating the operation for each layer, the field strength on the outer most interface $F(r_{N-1})$ (N is the total number of layers in the fiber structure) can be expressed as a function of the field strength of the inner most interface $F(r_1)$:

$$F(r_{N-1}) = T_{N-1}T_{N-2}\cdots T_2 F(r_1) \tag{2.22}$$

or

$$F(r_{N-1}) = TF(r_1), \tag{2.23}$$

where

$$T = T_{N-1}T_{N-2}\ldots T_2. \tag{2.24}$$

Due to the nature of Bessel functions of the second kind, $Y_v(ur)$ goes to infinity when $r \to 0$, therefore the field coefficient for this term must be equal to zero, i.e. $B_1 = D_1 = 0$. The field at the first dielectric interface r_1 is then expressed as

$$\begin{pmatrix} E_z(r_1) \\ H_z(r_1) \\ E_\phi(r_1) \\ H_\phi(r_1) \end{pmatrix} = \begin{pmatrix} J_v(u_1r_1) & 0 & 0 & 0 \\ 0 & 0 & J_v(u_1r_1) & 0 \\ \frac{\beta v}{u_1^2 r} J_v(u_1r_1) & 0 & \frac{jk_0 z}{u_1} J'_v(u_1r_1) & 0 \\ -\frac{jk_0 n_1^2}{u_1 z} J'_v(u_1r_1) & 0 & \frac{\beta v}{u^2 r} J_v(u_1r_1) & 0 \end{pmatrix} \begin{pmatrix} A_1 \\ 0 \\ C_1 \\ 0 \end{pmatrix} \tag{2.25}$$

At the outer most layer of the fiber, the radius becomes large and the electric field must tend toward zero. Because the modified Bessel function of the first kind, $I_\upsilon(ur)$, goes to infinity when $r \to \infty$ the field coefficients of $I_\upsilon(ur)$ must be zero, i.e. $B_N = D_N = 0$. In this case, the field expression at the outer most interface of the outer most layer is expressed as

$$\begin{pmatrix} E_z(r_{N-1}) \\ H_z(r_{N-1}) \\ E_\phi(r_{N-1}) \\ H_\phi(r_{N-1}) \end{pmatrix} = \begin{pmatrix} K_\upsilon(wr_{N-1}) & 0 & 0 & 0 \\ 0 & 0 & K_\upsilon(wr_{N-1}) & 0 \\ -\frac{\beta v}{w^2 r_{N-1}} K_\upsilon(wr_{N-1}) & 0 & -\frac{jk_0 z}{w} K'_\upsilon(wr_{N-1}) & 0 \\ \frac{jk_0 n_n^2}{wz} K'_\upsilon(wr_{N-1}) & 0 & -\frac{\beta v}{w^2 r_{N-1}} K_\upsilon(wr_{N-1}) & 0 \end{pmatrix} \begin{pmatrix} A_N \\ 0 \\ C_N \\ 0 \end{pmatrix} \tag{2.26}$$

Substituting Eq. 2.25 and Eq. 2.26 into Eq. 2.23 gives

$$\begin{pmatrix} K_v(w_N r_{N-1}) & 0 & 0 & 0 \\ 0 & 0 & K_v(w_N r_{N-1}) & 0 \\ -\frac{\beta v}{w_N^2 r} K_v(w_N r_1) & 0 & -\frac{jk_0 z}{w_N} K'_v(w_N r_1) & 0 \\ \frac{jk_0 n_n^2}{w_N z} K'_v(w_N r_1) & 0 & -\frac{\beta v}{w^2 r} K_v(w_N r_1) & 0 \end{pmatrix} \begin{pmatrix} A_N \\ 0 \\ C_N \\ 0 \end{pmatrix}$$

$$= T \cdot \begin{pmatrix} J_v(u_1 r_1) & 0 & 0 & 0 \\ 0 & 0 & J_v(u_1 r_1) & 0 \\ \frac{\beta v}{u_1^2 r} J_v(u_1 r_1) & 0 & \frac{jk_0 z}{u_1} J'_v(u_1 r_1) & 0 \\ -\frac{jk_0 n_1^2}{u_1 z} J'_v(u_1 r_1) & 0 & \frac{\beta v}{u^2 r} J_v(u_1 r_1) & 0 \end{pmatrix} \begin{pmatrix} A_1 \\ 0 \\ C_1 \\ 0 \end{pmatrix}, \tag{2.27}$$

and we can define a new matrix,

$$MT = T \cdot \begin{pmatrix} J_v(u_1 r_1) & 0 & 0 & 0 \\ 0 & 0 & J_v(u_1 r_1) & 0 \\ \frac{\beta v}{u_1^2 r} J_v(u_1 r_1) & 0 & \frac{jk_0 z}{u_1} J'_v(u_1 r_1) & 0 \\ -\frac{jk_0 n_1^2}{u_1 z} J'_v(u_1 r_1) & 0 & \frac{\beta v}{u_1^2 r} J_v(u_1 r_1) & 0 \end{pmatrix}. \tag{2.28}$$

From the properties of matrix products, in particular because the 2nd and the 4th column of the inner most expression are all zero, we know that ***MT*** must take the form:

$$MT = \begin{pmatrix} MT_{11} & 0 & MT_{13} & 0 \\ MT_{21} & 0 & MT_{23} & 0 \\ MT_{31} & 0 & MT_{33} & 0 \\ MT_{41} & 0 & MT_{43} & 0 \end{pmatrix} \tag{2.29}$$

Eq. 2.29 can be rewritten as

$$\begin{pmatrix} K_\upsilon(wr_{N-1}) & 0 & 0 & 0 \\ 0 & 0 & K_\upsilon(wr_{N-1}) & 0 \\ -\frac{\beta v}{w^2 r_{N-1}} K_\upsilon(wr_{N-1}) & 0 & -\frac{jk_0 z}{w} K'_\upsilon(wr_{N-1}) & 0 \\ \frac{jk_0 n_n^2}{wz} K'_\upsilon(wr_{N-1}) & 0 & -\frac{\beta v}{w^2 r_{N-1}} K_\upsilon(wr_{N-1}) & 0 \end{pmatrix} \begin{pmatrix} A_N \\ 0 \\ C_N \\ 0 \end{pmatrix} = \begin{pmatrix} MT_{11} & 0 & MT_{13} & 0 \\ MT_{21} & 0 & MT_{23} & 0 \\ MT_{31} & 0 & MT_{33} & 0 \\ MT_{41} & 0 & MT_{43} & 0 \end{pmatrix} \begin{pmatrix} A_1 \\ 0 \\ C_1 \\ 0 \end{pmatrix}. \tag{2.30}$$

The result of Eq. 2.30 is the following set of equations:

$$\begin{aligned}
&MT_{11}A_1 + MT_{13}C_1 - K_\upsilon(wr_{N-1})A_N + 0 = 0 \\
&MT_{21}A_1 + MT_{23}C_1 + 0 - K_\upsilon(wr_{N-1})C_N = 0 \\
&MT_{31}A_1 + MT_{33}C_1 + \frac{\beta v}{w^2 r_{N-1}} K_\upsilon(wr_{N-1})A_N + \frac{jk_0 z}{w} K'_\upsilon(wr_{N-1})C_N = 0 \\
&MT_{41}A_1 + MT_{43}C_1 - \frac{jk_0 n_n^{\,2}}{wz} K'_\upsilon(wr_{N-1})A_N + \frac{\beta v}{w^2 r_{N-1}} K_\upsilon(wr_{N-1})C_N = 0
\end{aligned} \quad . \tag{2.31}$$

In order that (A_1, C_1, A_N, C_N) have non-trivial solutions, the determinant of the matrix must equal to zero:

$$\det\begin{pmatrix}
MT_{11} & MT_{13} & -K_\upsilon(wr_{N-1}) & 0 \\
MT_{21} & MT_{23} & 0 & -K_\upsilon(wr_{N-1}) \\
MT_{31} & MT_{33} & \frac{\beta v}{w^2 r_{N-1}} K_\upsilon(wr_{N-1}) & \frac{ik_0 z}{w} K'_\upsilon(wr_{N-1}) \\
MT_{41} & MT_{43} & -\frac{ik_0 n_n^{\,2}}{wz} K'_\upsilon(wr_{N-1}) & \frac{\beta v}{w^2 r_{N-1}} K_\upsilon(wr_{N-1})
\end{pmatrix} = 0 \tag{2.32}$$

Eq. 2.32 is the eigenvalue equation of the multilayer optical fiber based on a full vector model. The effective index of the modes of a circular optical fiber can then be obtained by solving this eigenvalue equation.

Once the effective index is solved, we can substitute it into the transfer matrix and obtain the coefficients of the electric field in different layers. The field strength at different radial and azimuthal position can then be obtained by multiplying the expression matrix by the coefficient vector using Eq. 2.14, Eq. 2.8 and Eq. 2.9.

The field is then normalized by constraining the power carried by each mode to 1 Watt:

$$P = \frac{1}{2}\mathrm{Re}\int_0^{2\pi} d\phi \int_0^{\infty} rdr\left(E_r H_\phi^* - H_r^* E_\phi\right) = 1W \; . \tag{2.33}$$

2.1.3 Modal field profiles in a three-layer pristine fiber

In this section we examine the intensity distribution of the core and cladding modes in a three-layer straight optical fiber waveguide. Figure 2.2 shows the radial intensity distribution profiles of the eight lowest $HE_{1\nu}$ modes for a three-layer straight optical fiber waveguide, obtained using the mode solver outlined above. The figures' insets show 2-dimensional intensity maps of the modes. For better visualization, the radial refractive index profile for the three-layer structure is also shown in the figures.

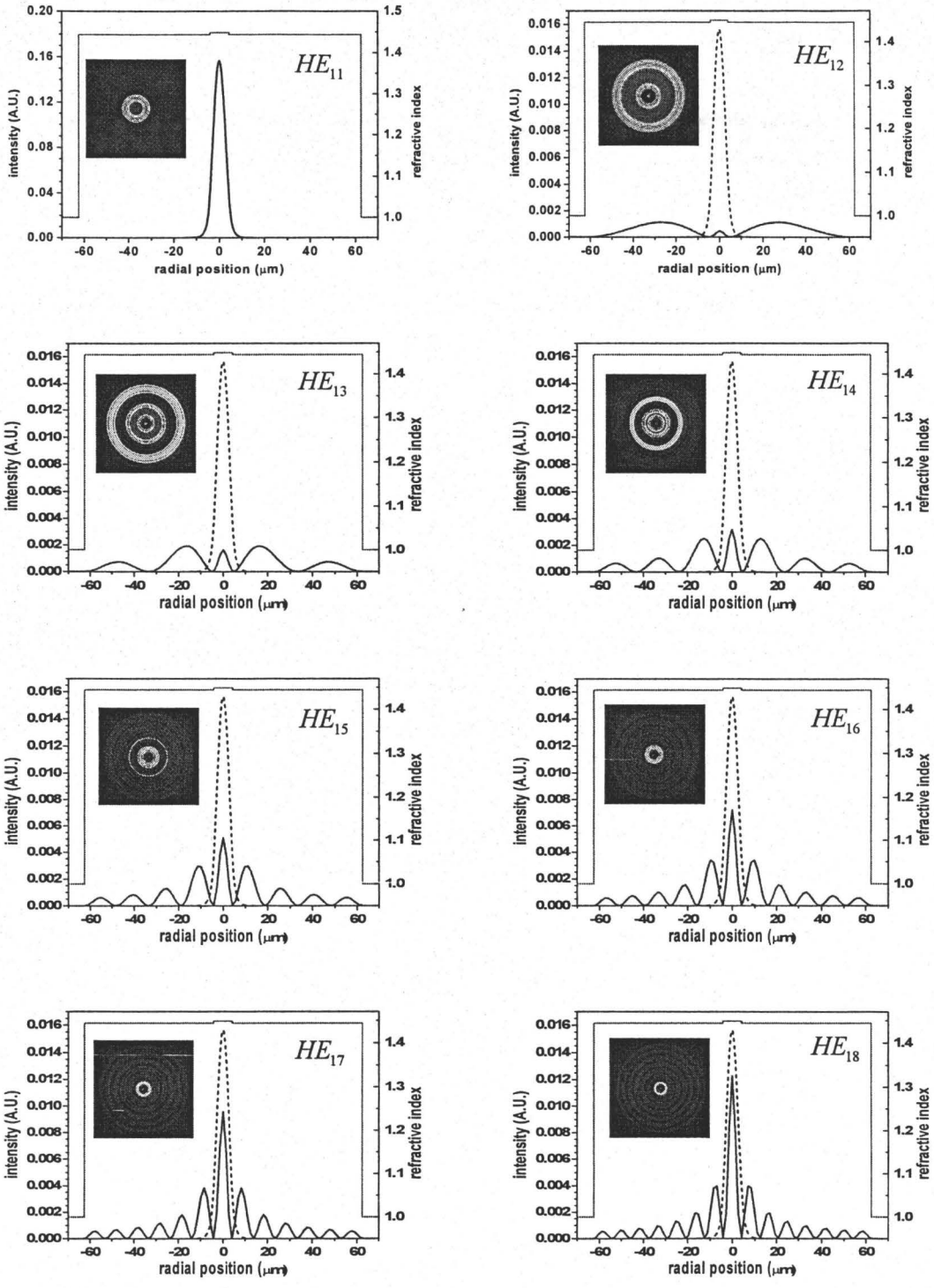

Figure 2.2 Radial intensity profiles of the first eight $HE_{1\nu}$ modes in a three-layer fiber waveguide

The parameters used in the simulation are as follows: fiber core radius, $r_1 = 4.15\mu m$; fiber core refractive index, $n_1 = 1.448933$; cladding radius $r_2 = 62.5\mu m$; fiber cladding refractive index $n_2 = 1.444024$; ambient medium refractive index $n_3 = 1$; and the wavelength of the light field, $\lambda = 1550nm$.

As can be seen from Figure 2.2, the fundamental mode HE_{11} has a non-oscillatory intensity distribution and is mostly confined to within the core of the optical fiber, i.e. the fundamental mode of the three-layer fiber is the core mode. The higher order $HE_{1\nu}$ modes display the same azimuthal symmetry as the core mode, but their radial components oscillate across the entire cross-section of the fiber resulting in significant field amplitude within the cladding. The higher order $HE_{1\nu}$ modes are thus, more accurately, cladding modes.

To compare the cladding mode intensity profiles of Fig. 2.2, the intensity of the fundamental HE_{11} mode (dashed line), scaled down by a factor of 10, is plotted together with the cladding modes. Clearly, the maximum amplitudes of the cladding modes are far lower than the core mode amplitude. However, the diameter of the center lobe of the intensity distribution, defined by the first zero intensity point on the radial axis, is comparable with the fiber core diameter, indicating that the single-core-mode waveguide structure induces a higher core mode amplitude than a two-layer large core diameter ($r = 62.5\mu m$) multi-mode fiber [71]. In addition, the penetration depth of the cladding mode fields into the surrounding medium (air $n_3 = 1$) increases with mode order, resulting in stronger evanescent fields spilling into the ambient. Thus, higher order cladding modes have greater sensitivity to changes in the ambient refractive index.

2.2 Cladding mode coupling by long period gratings

2.2.1 Theory of long period gratings

A fiber grating is a photonic device that is realized by inducing a periodic refractive index perturbation along the axis of an optical fiber. The most popular method of manufacturing fiber gratings is by illuminating the side of a fiber with a spatially varying ultraviolet (UV) field [68, 69, 72]. The result of the UV exposure is a refractive index change in the fiber core due to the photosensitivity of the Ge doped silica there, while the refractive index of the cladding layer remains unchanged. The axial index modulation profile due to the UV exposure can be expressed as:

$$n_1(z) = n_1\left\{1+\sigma(z)\left[1+m\cos\left(\frac{2\pi}{\Lambda}z\right)\right]\right\} \tag{2.34}$$

where n_1 is the unperturbed refractive index of the fiber core, m is the visibility of the induced refractive index modulation ($0 \le m \le 1$), Λ is the period of the grating, and $\sigma(z)$ is the refractive index modulation envelope (also called apodization function).

In the ray optics picture of diffraction from an inscribed grating, Fig. 2.3, the incident and the diffracted light rays satisfy the familiar diffraction equation:

$$n_2 \sin\theta_2 = n_1 \sin\theta_1 + q\frac{\lambda}{\Lambda} \tag{2.35}$$

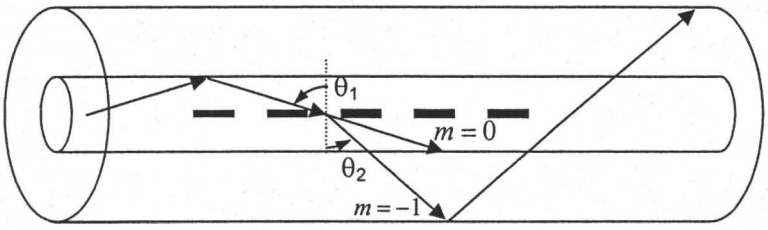

Figure 2.3 Ray optics illustration of core-cladding mode coupling by a long period grating.

where n_1 is the core refractive index, n_2 is the cladding refractive index, q is the order of diffraction, λ is the wavelength of the light, Λ is the period of the diffraction grating, θ_1 is the angle of incidence, and θ_2 is the angle of diffraction. In the case of a transmission grating, the prominent diffraction order is $q = -1$, and since $n_{eff,co} = n_{co}\sin\theta_1$ and $n_{eff,cl} = n_{cl}\sin\theta_2$, Eq.2.34 can be rewritten as

$$\lambda = \left(n_{eff,co} - n_{eff,cl}\right)\Lambda . \tag{2.36}$$

Eq.2.35 is the phase matching condition for co-directional mode coupling. Since the difference in the effective indices of the core and cladding for typical commercial fibers are small, the grating period must be large (as compared with fiber Bragg gratings) in order to push the resonant wavelength into typical communications wavelength, and thus fiber transmission gratings are known as long period gratings (LPG).

The ray optics model of core-cladding mode coupling is insufficient for detailed analysis. The mode coupling process by a fiber grating can be more thoroughly described using the couple mode theory. The refractive index modulation across a long period grating fiber inscribed in the fiber core can be regarded as uniform. Because of mode orthogonality, mode coupling occurs only between modes with the same azimuthal mode order. According to Erdogan [73], the coupled mode equations that describe the amplitude change in the core mode (HE_{11} mode) and the co-propagating cladding modes ($HE_{1\nu}$ modes) in an optical fiber long period grating with a uniform refractive index modulation across the fiber core cross section can be written as:

$$\frac{dA^{co}}{dz} = j\kappa_{11-11}^{co-co} A^{co} + j\sum_{\nu} \frac{m}{2} \kappa_{1\nu-11}^{cl-co} A_{\nu}^{cl} \exp\left(-j2\delta_{1\nu-11}^{cl-co} z\right) \tag{2.37}$$

$$\sum_{\nu}\left[\frac{dA_{\nu}^{cl}}{dz} = j\frac{m}{2}\kappa_{1\nu-11}^{cl-co} A^{co} \exp\left(j2\delta_{1\nu-11}^{cl-co} z\right)\right] \tag{2.38}$$

where A^{co} the amplitude of the core mode (HE_{11} mode); A_{ν}^{cl} the amplitude of the ν^{th} order cladding mode; κ_{11-11}^{co-co} is the core-core self coupling coefficient of the fundamental HE_{11} mode and can be expressed as

$$\kappa_{11-11}^{co-co}(z) = \frac{\omega\varepsilon_0 n_1^2 \sigma(z)}{2} \int_0^{2\pi} d\phi \int_0^{r_1} r dr \left(\left|E_r^{co}\right|^2 + \left|E_{\phi}^{co}\right|^2\right); \tag{2.39}$$

$\kappa_{01-0\nu}^{co-cl}$ is the HE_{11} - $HE_{1\nu}$ coupling coefficient,

$$\kappa_{1\nu-11}^{cl-co}(z) = \frac{\omega\varepsilon_0 n_1^2 \sigma(z)}{2} \int_0^{2\pi} d\phi \int_0^{r_1} r dr \left(E_r^{\nu,cl} E_r^{co*} + E_{\phi}^{\nu,cl} E_{\phi}^{co*}\right); \tag{2.40}$$

and $\delta_{11-1\nu}^{cl-co}$ is the detuning parameter

$$\delta_{11-1\nu}^{cl-co} = \frac{1}{2}\left(\beta_{11}^{co} - \beta_{1\nu}^{cl} - \frac{2\pi}{\Lambda}\right), \tag{2.41}$$

where $\beta_{11}^{co} = n_{eff,11}^{co} k_0$ is the core mode propagation constant and $\beta_{1\nu}^{cl} = n_{eff,1\nu}^{cl} k_0$ is the ν^{th} cladding mode propagation constant.

Eq.2.37 and Eq. 2.38 are coupled first order differential equations, and given the large number of cladding modes the solution to Eq. 2.37 and Eq. 2.38 is complicated and difficult to obtain. However, by noting that only one of the cladding modes is near to the resonance to the core mode at a wavelength, the solution can be greatly simplified by neglecting all of the other resonances. In a uniform grating, the amplitude of the index modulation is constant

$$\sigma(z) \equiv \sigma n_1 . \tag{2.42}$$

Analytical solutions for Eq. 2.37 and Eq. 2.38 exist and are

$$A_{11}^{co}(L/2) = \left[\cos(\gamma_c L) + j\frac{\hat{\sigma}}{\gamma_c}\sin(\gamma_c L)\right] A_{11}^{co}(-L/2) + j\frac{\kappa_{1\nu-11}^{cl-co}}{\gamma_c}\sin(\gamma_c L) A_{1\nu}^{cl}(-L/2) \tag{2.43}$$

$$A_{1\nu}^{cl}(L/2) = j\frac{\kappa_{1\nu-11}^{cl-co}}{\gamma_c}\sin(\gamma_c L) A_{11}^{co}(-L/2) + \left[\cos(\gamma_c L) - j\frac{\hat{\sigma}}{\gamma_c}\sin(\gamma_c L)\right] A_{1\nu}^{cl}(-L/2), \tag{2.44}$$

where

$$\gamma_c \equiv \sqrt{\kappa_{1\nu-11}^{cl-co2} + \hat{\sigma}^2} \tag{2.45}$$

$$\hat{\sigma} \equiv \delta_{11-1\nu}^{cl-co} + \frac{\kappa_{11-11}^{co-co} - \kappa_{1\nu-1\nu}^{cl-cl}}{2} \tag{2.46}$$

$$\kappa_{1\nu-1\nu}^{cl-cl}(z) = \frac{\omega\varepsilon_0 n_1^2 \sigma(z)}{2} \int_0^{2\pi} d\phi \int_0^{r_1} r dr \left(\left| E_r^{cl} \right|^2 + \left| E_\phi^{cl} \right|^2 \right). \tag{2.47}$$

The boundary conditions for a long period grating of length L are $A_{11}^{co}(-L/2) = 1$ and $A_{1\nu}^{cl}(-L/2) = 0$. The transmission spectrum of long period grating can be calculated using

$$T(\lambda) = \frac{A_{11}^{co2}(L/2)}{A_{11}^{co2}(-L/2)} \tag{2.48}$$

Plug Eq. 2.42 into Eq. 2.47, and

$$T = \frac{\left| A_{11}^{co}(L/2) \right|^2}{\left| A_{11}^{co}(-L/2) \right|^2} = \frac{\delta_{11-1\nu}^{cl-co2}}{\gamma_c^2} \sin^2(\gamma_c L) + \cos^2(\gamma_c L) \tag{2.48}$$

At the resonance wavelength, where

$$\delta_{11-1\nu}^{cl-co} = \frac{1}{2}\left(\beta_{11}^{co} - \beta_{1\nu}^{cl} - \frac{2\pi}{\Lambda} \right), \tag{2.49}$$

the maximum loss in the transmission spectrum is:

$$T_{\min}^{11-1m} = 1 - \sin^2 \kappa_{11-1m} L. \tag{2.50}$$

when $\delta_{11-1\nu}^{cl-co} = 0$.

2.2.2 Long period grating spectra

Typical transmission spectra of a uniform long period grating are shown in Fig. 2.4. As can be seen, the six notches correspond to coupling from the HE_{11} mode to the HE_{12}, HE_{13}, HE_{14}, HE_{15}, HE_{16}, and HE_{17} cladding modes. The transmission spectrum of the long period grating is fitted using the formulas given in Section 2.2.1. and is

plotted as a dotted line in Fig. 2.4. The parameters used for the grating transmission synthesis are: $r_1 = 4.15\mu m$; $r_2 = 62.5\mu m$; cladding refractive index is determined by a three-term Sellmeier equation for fused silica; $(n_1 - n_2) = \Delta n = 0.0034$; $n_3 = 1$; $\Lambda = 256\mu m$; grating $L = 12.5mm$; and the amplitude of the AC component of the refractive index modulation, $m\sigma n = 6.6\times10^{-4}$; and the DC component of the refractive index modulation, $\sigma n = 1.88\times10^{-3}$. The experimental and simulated results match very well, as shown in the figure. Note that the notch depths increase with the order of the cladding mode. This is due to the increase in the cladding mode field amplitude within the core with increasing mode order (see Fig. 2.2), which according to Eq.2.39 results in an increase in the $HE_{11} - HE_{1\nu}$ mode coupling coefficient, $\kappa_{1\nu-11}^{cl-co}$. From Eq.2.50, for weak long period gratings and as long as $\kappa_{1\nu-11}^{cl-co} L < \frac{\pi}{2}$, the notch depths in the transmission spectrum increase with the cladding order. However, it is worth noting that when the order of the cladding mode is sufficiently high ($\nu > 12$ in Corning™ SMF-28 fiber), the coupling coefficient starts to decrease with cladding mode order, as a result of the reduction in the cross-sectional radius of the first lobe of the field distribution in the fiber core. Further more, when the grating is too strong or too long ($\kappa_{1\nu-11}^{cl-co} > \frac{\pi}{2}$) so that the core mode is completely coupled into the cladding mode, a smaller notch depth in the transmission spectrum is also observed.

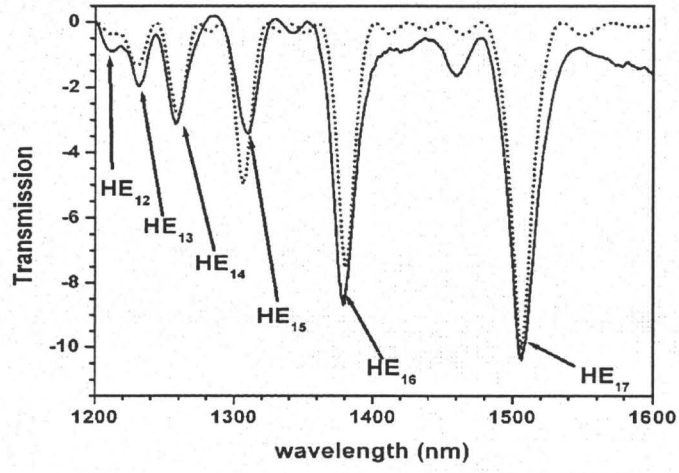

Figure 2.4 Experimental transmission spectrum of a long period grating (solid line) and the simulated transmission spectrum utilizing the analytic solution for a uniform long period grating (dotted line).

In this chapter, we have described the basic theory of optical fiber waveguides and long period gratings. The optical modes propagating in a single-mode optical fiber without an absorbing jacket consist of a fundamental mode confined in the fiber core and a series of cladding modes confined by the interface between the cladding layer and the ambient. Using a transfer matrix method, the formulation for solving the mode effective indices and mode profiles based on a full-vector model has been given. When a periodic

refractive index perturbation with an appropriate period is induced along the fiber axis, a light wave in the fundamental HE_{11} mode can be coupled to the corresponding $HE_{1\nu}$ cladding modes in a wavelength dependent fashion which leaves notches in the transmission spectrum of the long period grating. The analytic solution of a uniform long period grating based on two-mode coupling has also been given. The transmission spectrum simulated using this method matches well with the experimental transmission data, indicating that the analytic solution is a precise description of the co-directional coupling in a long period grating.

Chapter 3
Enhancement of Sensitivity through Waveguide Structure Modification

In the continuous endeavor to improve the performance of biosensor, people look for fast and easy-to-operate sensing technique with high sensitivity, high selectivity, high analyte concentration resolution and large dynamic range of detection. As has been stated in Chapter 1, while other parameters are largely determined by the biorecognition material, the physico-chemical transducers, together with the sensing material, determine the sensitivity and resolution of the biosensor in principle. For the fiber optic label-free biosensors, the refractive index change of the biorecognition film is modulated to the light wave propagating in the fiber. In the current project, such a transducing mechanism first relies on dependence of the effective indices of the eigen mode of the fiber waveguide on the refractive index of the ambient medium. The mode effective index modulations are then converted to other measurable physicsl parameters. In order to enhance the sensitivity of the fiber optic label free biosensor, we first try to enhance the dependence of the fiber mode effective indices to the refractive index of the surrounding medium which is carried out by modifying the waveguide structure of the optical fiber.

In the proceeding chapters we have studied the theory of the optical light field in the cylindrical multi-layer dielectric waveguide and the co-directional coupling between the core mode and cladding modes in a single mode optical fiber through a long-period grating. Because the core mode is isolated from the ambient, a long period grating based refractive index sensors are based on modulation of the cladding modes by the ambient refractive index change through the evanescent wave. To boost the sensitivity of the long period grating based fiber optic refractive index sensor, it is necessary to enhance the dependence of the cladding modes on the ambient refractive index by enhancing existence of the evanescent wave of the cladding modes in the ambient medium. In this chapter, two strategies are taken to enhance the existence of the evanescent wave of the cladding mode in the ambient medium and thus increase the dependence of the cladding modes on ambient refractive index change. All these methodologies are systematically examined with the full vector fiber mode theory for straight multi-layer dielectric fiber, which is solved with the transfer matrix method given in Chapter 2.

The rest of this chapter is organized in the following way: In Section 3.1, reduction of the cladding layer diameter is utilized to set the cladding modes closer to cutoff of the modes and thus increase its sensitivity to the ambient refractive index. Section 3.2 examines in detail the mode reorganization induced by the application of a layer of high refractive index material on top of the fiber cladding, called high refractive index overlay, and its effect on enhancing the dependence of the cladding modes effective index upon ambient refractive index. Based on the cladding mode analysis given in Section 3.1 and Section 3.2, Section 3.3 theoretically proposes a method to enhance the sensitivity of a long period grating biosensor with a low refractive index bio-recognition film. By introduce a layer of high refractive index overlay beneath the bio-

recognition film, the sensitivity of the cladding modes on the bio-recognition film can be enhanced by changing the refractive index and/or thickness of the overlay. At last, as an application of the cladding layer structure modification, a long period grating refractive index sensor is theoretically studied by reducing the cladding layer diameter, applying a high refractive index overlay and keeping the grating period as an adaptive parameter in the sensor design. The result of these measurements is a long period grating with high sensitivity and wider operational range.

3.1 Fiber cladding reduction

As has been described in Chapter 2, when studding the cladding modes of an optical fiber, the optical waveguide provided by an optical fiber without application of overlay is a three-layer fiber waveguide consists of a fiber core, a fiber cladding and the ambient medium (see Fig. 3.1). The effective index of the fiber modes is a function of all the fiber parameters specified in Fig. 3.1. For a commercial available step-index single-mode optical fiber, the refractive index of the fiber core n_1 and fiber cladding n_2 and the radius of the fiber core r_1 are constant. In the theoretical study for enhancing the dependence of the fiber cladding modes on the ambient refractive index through cladding reduction, the ambient refractive index is an independent variable, while the cladding

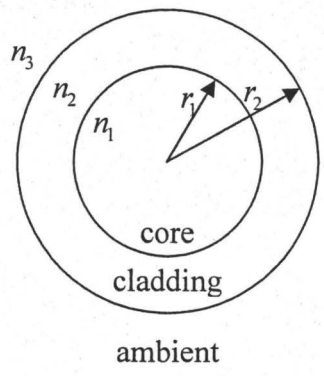

Figure 3.1 Schematic cross sectional structure of a fiber without overlay

radius is a variable parameter for the sensitivity optimization. The enhancement of the cladding mode dependence on ambient refractive index is characterized by a partial differential of the effective index of the cladding modes against the ambient refractive index as a function of the cladding radius. Fig. 3.2 presents the effective indices of the core mode (HE_{11} mode) and the first eight cladding modes as a function of the ambient refractive index $n_{eff,cl}\left(n_{amb}\right)\Big|_{r_2}$ and the differential of the effective index of the cladding modes against the ambient refractive index $dn_{eff,cl}\left(n_{amb}\right)/dn_{amb}\Big|_{r_2}$. The fiber under study is based on Corning SMF-28™ fiber, for which the parameters of the fiber are: fiber core radius $r_1 = 4.15\mu m$, refractive index of the cladding $n_2 = 1.44024$, the refractive index of

the fiber core $n_1 = 1.448933$, wavelength of the light wave $\lambda = 1550nm$. To study the

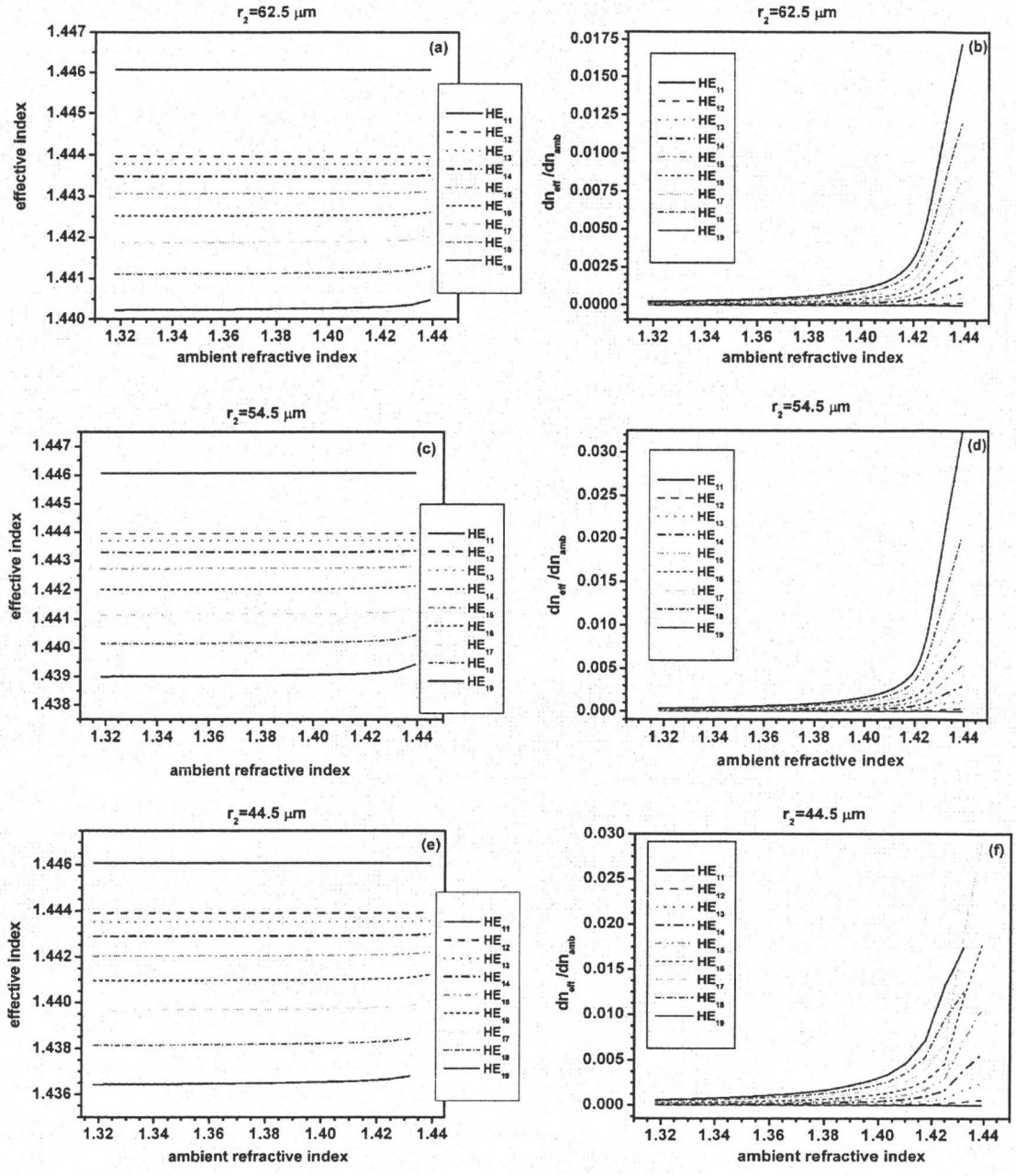

Figure 3.2 Effective indices of the cladding modes (a, c, e, g, i, k, l, m) and the differentials of the effective indices against ambient refractive indices (b, d, f, h, j, l, n) as a function of the ambient refractive index.

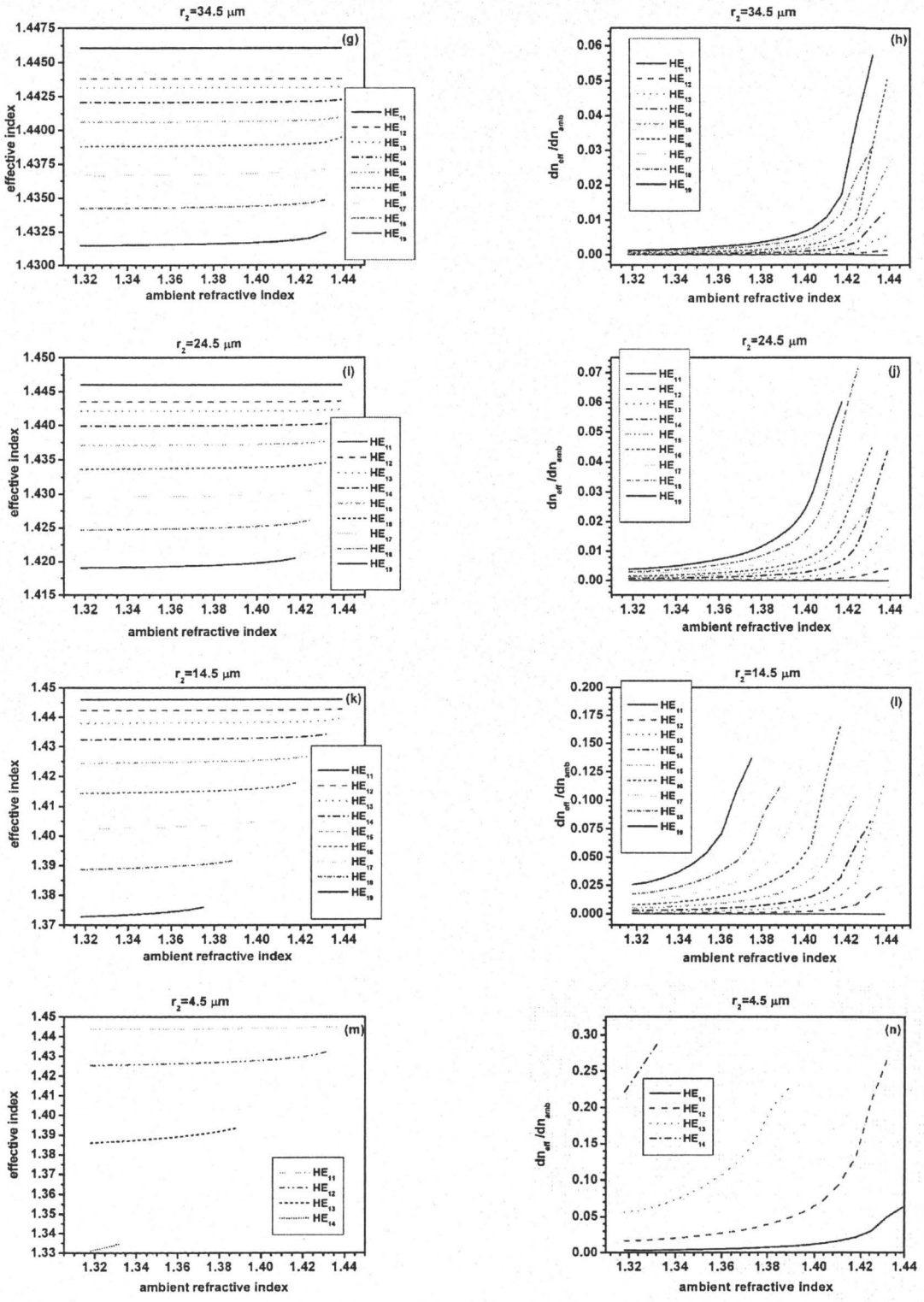

Figure 3.2 Effective indices of the cladding modes (a, c, e, g, i, k, l, m) and the differential of the effective indices against ambient refractive indices (b, d, f, h, j, l, n) as a function of the ambient refractive index. (continue)

dependence of the cladding modes on the ambient refractive index at different cladding radius, we set the cladding radius to $62.5\mu m$, $54.5\mu m$, $44.5\mu m$, $34.5\mu m$, $24.5\mu m$, $14.5\mu m$ and $4.5\mu m$ respectively and studied the change of the cladding mode effective index when the ambient refractive index varies between $n_3 = 1.318$ and $n_3 = 1.44$.

Notice the vertical scale difference among the sub-figures in Fig. 3.2, it can be found that: First, when the cladding layer is thick enough ($r_2 > 14.5\mu m$), the effective index of the fundamental HE_{11} mode is independent on the ambient refractive index change. However, as the cladding radius is reduced to be so small (below $14.5\mu m$) that the evanescent wave of the HE_{11} mode penetrates to ambient medium, the effective index of the HE_{11} mode turns to be dependent on the ambient refractive index. When the cladding radius is reduced to small value, the effective index of the HE_{11} mode turns to be dependent on the ambient refractive index. Based on this property fiber Bragg grating refractive index sensor with etched cladding layer was demonstrated [43]. On the other hand, given the fact that the cladding modes are directly modulated by the refractive index change of the ambient medium through the evanescent wave, the effective indices of the cladding modes are highly dependent on the ambient refractive index change. The dependence of the cladding modes indices on the ambient refractive index varies with the ambient refractive index as well. When the ambient refractive index is far below the refractive index of the cladding layer ($n_2 = 1.444024$), the dependence of the effective indices are low. As the ambient refractive approaches the cladding layer refractive index, the dependence of the cladding modes effective indices increases quickly with the ambient refractive index. In the meantime, the dependence of the effective indices on the ambient refractive index depends on the order of the cladding modes as well, the higher the cladding modes, the higher the dependence. It is for this reason that high order cladding modes are desirable in ambient refractive index sensing from the view point of the cladding mode effective index dependence on the ambient refractive index. At last, when the ambient refractive index reaches certain value, the cladding modes reaches their cutoff and thus are not supported by the cladding waveguide, which lays an upper limit of the operational range on the ambient refractive index axis.

When the diameter of the cladding is reduced, three phenomenons can be observed: First of all, the changes of the cladding modes effective indices upon the ambient refractive index change are greatly enhanced. Next, the effective index difference between neighboring cladding modes increases with reduction of the cladding radius. At last, as the radius of the cladding layer is reduced, cutoff of all the cladding modes move towards the lower index side on the ambient refractive axis. The higher the order of the cladding modes, the faster the cladding modes reach their cutoff.

The dependence of the cladding mode effective index upon the ambient refractive index and the cladding radius can be explained by mimic the waveguiding of the cladding layer to a large core two-layer optical fiber. It should be mentioned that according to Erdogan [73] and our calculation, the mode field distributions and effective index of the cladding modes are profoundly different from a two-layer optical fiber with the core radius equal to the cladding radius of a three-layer optical fiber (A direct proof of the difference is the field distribution of the fundamental HE_{11} mode in a three-layer optical fiber, which is confined to the inner core, while for the mimic two-layer fiber model, the

fundamental HE_{11} mode spread all over the large core area with its radius equal to the radius of the three-layer fiber cladding). However, given the refractive index difference between the fiber core and fiber cladding and the fiber radius is fixed, one can define the normalized frequency of the cladding layer waveguide V_{cl} as:

$$V_{cl} = \frac{2\pi r_2}{\lambda}\sqrt{n_2^2 - n_3^2} \tag{3.1}$$

where λ is the wavelength of the light wave. Similarly, we define the normalized propagation constant of the cladding modes as:

$$b_{cl} = \frac{n_2^2 - n_{eff,cl}^2}{n_2^2 - n_3^2} \tag{3.2}$$

Converting the data presented in Fig. 3.2 (a, c, e, g, i, k, l, m) into b_{cl} and V_{cl} respectively, Fig. 3.3 presents the $b_{cl} - V_{cl}$ curve of the first eight cladding modes. The curves shown in the figure are made by stitching the dispersion curves of the cladding mode with different cladding radius together. It is obvious that if the parameters of the core are fixed, overall, the dispersion of the cladding modes follow the dispersion of two-layer multimode fiber, in which the normalized propagation constant b_{cl} changes from 0 to 1 with the increase of normalized frequency V_{cl}. The slope (i.e. the dependence) of the $b_{cl} - V_{cl}$ curve goes up quickly as the normalized frequency of the cladding modes approaches their cutoff. In the meantime, with the existence of the fiber core, the precision of traditional $b - V$ relationship built on the two-layer fiber waveguide mode degrade, which is reflected in the discrepancy between the curves obtained with different cladding layer radius. Though, given the small discrepancy between the b_{cl} obtained with different cladding radius as compared to the b_{cl} difference between neighboring cladding modes, it is safe for us to discuss the dispersion of the cladding modes with the $b_{cl} - V_{cl}$ curve.

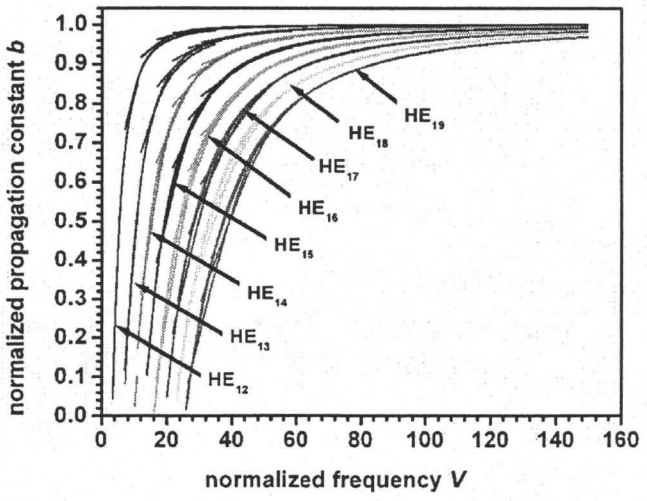

Figure 3.3 Normalized propagation constant of the first eight cladding modes b_{cl} as a function of the normalized frequency of the cladding mode V_{cl}.

From Fig. 3.3, the slopes of the $b_{cl} - V_{cl}$ curves increase when the value of V_{cl} move toward their cutoff. According to Eq. 3.1, the normalized frequency of the cladding waveguide is a function of both the cladding radius and the refractive index between the cladding and the ambient medium. When the refractive index of the ambient increases from a low value to a value of the cladding layer, the value of V_{cl} decreases. As a consequence the normalized propagation constant b_{cl} of the cladding modes decrease. Plug the value of b_{cl} into Eq.3.2 and taking into account of the increase of n_3, the effective index of the cladding modes increase with the increase of n_3. When $n_3 \to n_2$, the value of $\sqrt{n_2^2 - n_3^2}$ brings V_{cl} close to the cutoff of the cladding modes and the dependence of b_{cl} on V_{cl} steps up, i.e. the dependence of cladding effective index on the ambient refractive index $dn_{eff,cl}(n_{amb})/dn_{amb}$ in Fig. 3.2 rises up quickly.

By reducing the cladding radius r_2 in Eq.3.1, one diminishes the value of V_{cl}. From Fig. 3.3, it can obviously be observed that: First, the difference of value between neighboring normalized propagation constant is enlarged. Secondly, once the value of V_{cl} is brought down towards the cladding mode cutoff by reducing the cladding radius, the slope of the $b - V$ curve is boosted, as a consequence, $dn_{eff,cl}(n_{amb})/dn_{amb}$ is enhanced.

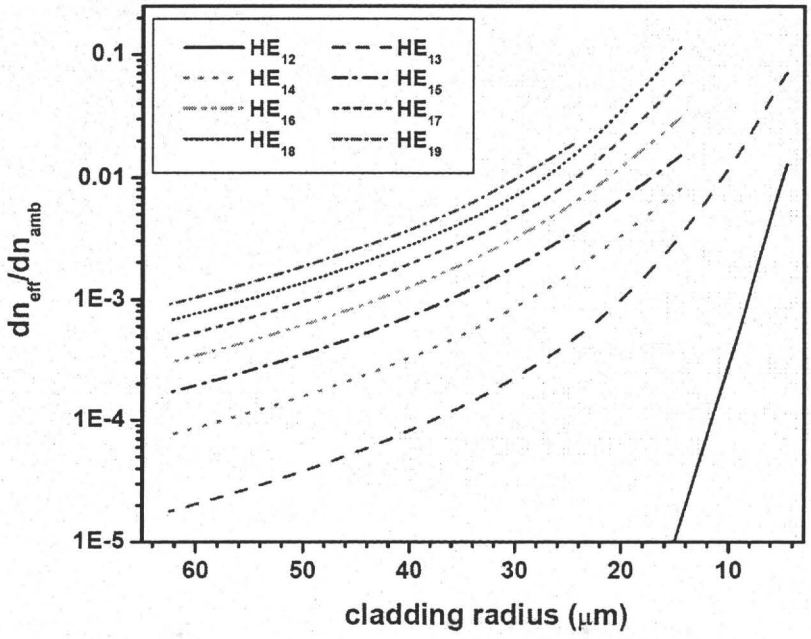

Figure 3.4 Dependence of the cladding mode effective indices on the refractive index as a function of the cladding radius. The calculation is carried out when the ambient refractive index is around 1.4035.

To study the enhancement of the dependence of the cladding mode effective indices on the ambient refractive index, in Fig. 3.4, $dn_{eff,cl}(n_{amb})/dn_{amb}$ of the first 8 cladding modes are plotted against the cladding radius. The parameters of the fiber used

in the calculation are the same as specified above and the calculation is carried out with an ambient refractive index around 1.4035. From Fig. 3.4, the relationship between the enhancement of $dn_{eff,cl}(n_{amb})/dn_{amb}$ and the cladding reduction can easily be observed. When the fiber cladding is not reduced, i.e. $r_2 = 62.5\mu m$, the value of $dn_{eff,cl}(n_{amb})/dn_{amb}$ is very small. As r_2 is reduced to smaller value, the dependence of the cladding mode on the ambient refractive index keeps low till $r_2 = 30\mu m$, where $dn_{eff,cl}(n_{amb})/dn_{amb}$ boost up quickly as the cladding radius is further reduced. The lower limit of cladding reduction is around $r_2 = 15\mu m$. When $r_2 < 15\mu m$, the cladding modes under current study start to reach their cutoff in sequence, from high order mode to lower order modes.

In this section, we have studied enhancing the dependence of the cladding modes on the ambient refractive index change by reducing the radius of the cladding layer. The physics of the enhancing mechanism is given by studying the dispersion relation of the cladding waveguiding and its dependence on the normalized frequency of the cladding waveguide. At last, we studied quantitatively the amount of the dependence enhancement on the cladding diameter. It is found that the cladding reduction works in the range when r_2 is between $15\mu m$ and $30\mu m$.

3.2 Mode reorganization induced by high refractive index overlay

In Section 3.1, we have studied the dependence of the effective indices of the cladding modes upon the ambient refractive index based on a three-layer fiber waveguide structure and the effect of cladding radius reduction. In this section, we study the change of the cladding modes in a four-layer fiber waveguide, where a layer of material with refractive index higher than the refractive index of the cladding is applied on top of the cladding. Application of high refractive index overlay on top of the fiber cladding was originally experimentally studied by Rees et. al. [44]. It was found that when the thickness and refractive index of the applied high refractive index overlay satisfy certain conditions, a redistribution of the low-order cladding mode field in the cladding waveguide would be induced. The outer most "lobes" of the cladding modes field were "sucked" into the high refractive index overlay. As a consequence, the effective indices of the cladding modes rapidly shifted to higher values, in some cases even higher than the core mode. Such a phenomenon was named as mode reorganization [51, 74].

3.2.1 Mode reorganization

The four-layer optical fiber waveguide under study is depicted in Fig. 3.5. The four-layer fiber waveguide consists of a fiber core-cladding structure and a layer of high refractive index material deposited directly on top of the fiber cladding. Outside of the high refractive index overlay is the ambient medium as the case in many applications. To study the behavior of the cladding modes as a function of the overlay parameter, we first

fixed the parameters of the fiber structure defined in Figure 3.5 as: $r_1 = 4.15\mu m$, $n_1 = 1.448933$, $n_2 = 1.444024$, $n_4 = 1$, and varied n_3 and d in studies.

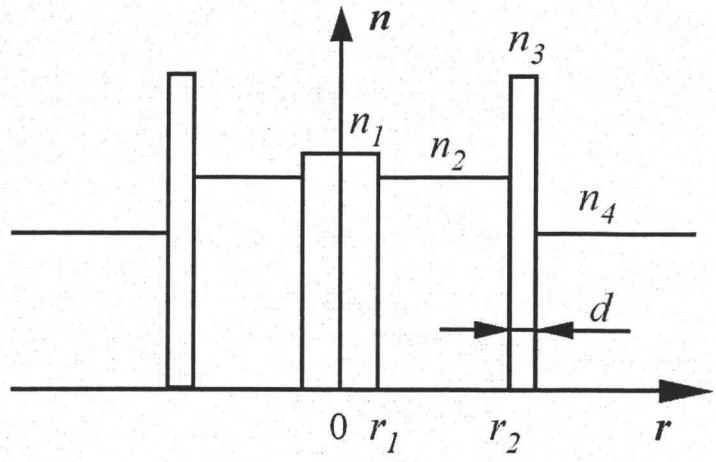

Figure 3.5 Radial refractive index profile of a structure modified long period grating refractive index sensor.

We first studied the change of the effective index of the cladding modes as a function of the overlay thickness by setting the refractive index of the overlay $n_3 = 1.7$. Simulation results are plotted in Fig. 3.6. As expected, given the fact the HE_{11} core mode is far away from the overlay, its effective index keeps independent on the overlay parameter. In the meantime, the effective indices of the cladding modes shift to higher values as the thickness of the overlay increase (see Fig. 3.6a). When the thickness of the overlay is below a "threshold" value (a dependent of the refractive index of the overlay, $d < 180nm$, in the our study), the effective indices of the cladding modes have low sensitivity to the change of the overlay thickness change. At the threshold thickness value, the slope of the cladding modes $n_{eff} - n_{amb}$ curves changes abruptly. When the overlay thickness is larger than the "threshold" thickness, the effective index of the HE_{12} mode jumps to a value greater than the effective index of the HE_{11} mode with large slope. It is well known that the value of the effective index of a guided mode is between the refractive indices of the guiding layer and the cladding layer. An effective index higher than the refractive index of the fiber cladding associated with the HE_{12} mode implies that the HE_{12} mode is not guided by the cladding layer any more. Instead, as shown in Fig. 3.6b, when n3>1,7, one finds that $n_4 < n_2 < n_{eff,HE_{12}} < n_3$ and the $n_{eff,HE_{12}} - d$ curve resembles the dispersion relation of an asymmetric three-layer slab waveguide, indicating the HE_{12} mode is guided by the overlay only. We nominate the HE_{12} mode in this case as an overlay mode. In the meantime, the effective indices of the higher cladding modes

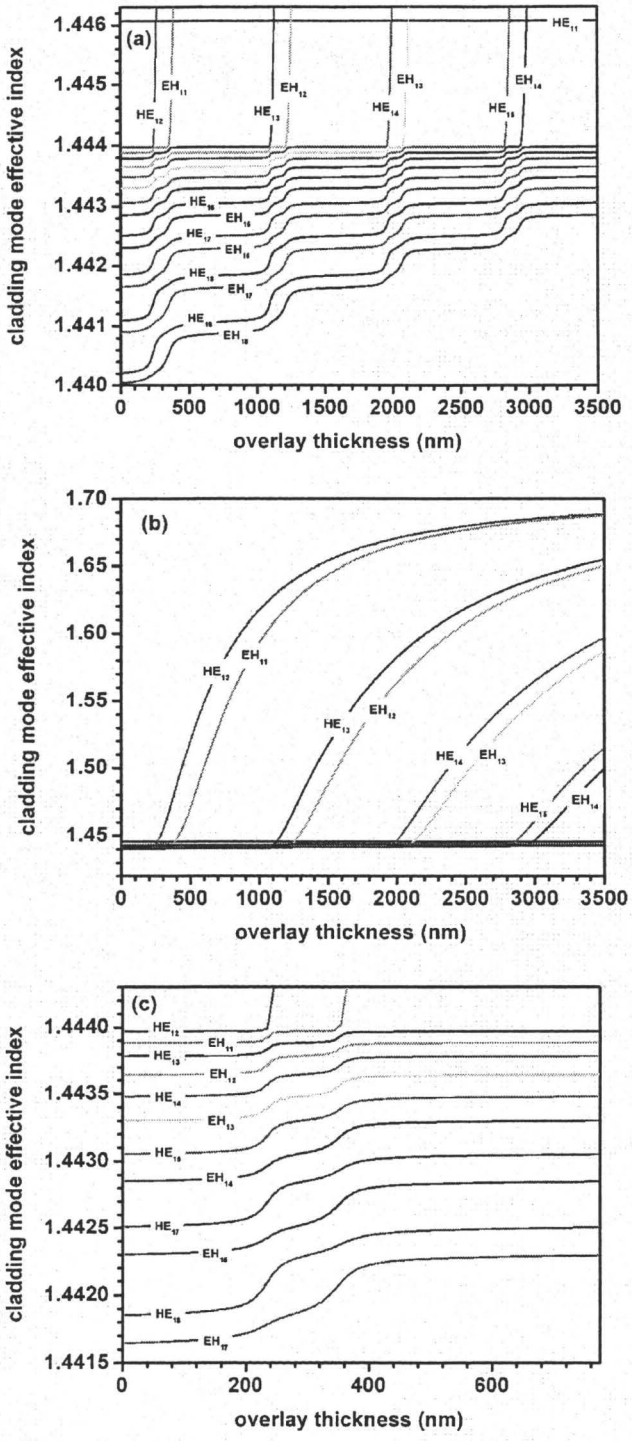

Figure 3.6 Effective indices of the fiber mode as a function of overlay thickness in an optical fiber with a high refractive index overlay. (a) effective index shift of the core mode and the cladding modes; (b) effective index change of the cladding-overlay modes; (c) zoom-out of the effective index shift curve of cladding modes present a two-step transition of the effective index, corresponding the cladding mode to cladding-overlay mode transition of the HE mode and EH mode respectively.

rapidly increase to the value of the adjacent lower order cladding modes. The phenomenon that when the guidance of the lowest cladding mode shifts from the cladding to the overlay, the high order cladding mode effective index shifts to the value of the adjacent lower cladding mode before the transition is called mode reorganization [51, 74]. Furthermore, as shown in Fig. 3.6c, as the overlay thickness increases further to another overlay thickness threshold, the effective index of the EH_{11} mode, like the HE_{12} mode, shifts to a value higher than the HE_{11} mode as well. Along with this transition, the effective indices of all the higher order cladding modes shifts to the lower adjacent modes again. As a result, the effective index shift of the high order cladding mode in the mode reorganization presents a two-step feature as shown in Fig. 3.6b, which corresponds to the guidance transition of the HE_{12} mode and the EH_{11} mode, respectively. When the thickness of the overlay increases further ($d > 400nm$), the effective index change of the cladding modes upon the overlay thickness change decreases again. The $n_{eff,cl} - d$ curve keeps flat till another overlay thickness threshold around $1150nm$ is reached and the cladding mode to overlay mode transition happens sequentially for the HE_{13} mode and the EH_{12} mode. As a result, another round of mode reorganization happens to the higher order cladding modes.

3.2.2 Dependence of mode reorganization on overlay refractive index

Once the mode reorganization of the cladding mode in a fiber with high refractive index overlay was revealed, we examined the dependence of the mode reorganization upon the refractive index of the overlay. In Fig. 3.7, the effective index shift as a function of the cladding thickness for a refractive index of the overlay $n_3 = 1.45$ (Fig. 3.7a), $n_3 = 1.55$ (Fig. 3.7b), $n_3 = 1.65$ (Fig. 3.7c), $n_3 = 1.75$ (Fig. 3.7d), and $n_3 = 1.85$ (Fig. 3.7e) is shown. The overlay thickness ranges from 0 to $1000nm$. In addition, as has been pointed out in Chapter 2, only the HE mode has significant energy coupling with the HE_{11} mode when the mode order is low (< 20), we omit the EH mode and plot only the curves associated with the HE modes.

The effect of the overlay refractive index on the $n_{eff,cl} - d$ curve lies in that it displaces the mode reorganization zone on the overlay thickness axis. When the overlay refractive index is low ($n_3 = 1.45$, Fig. 3.7a), it needs a very thick overlay to reach the mode reorganization threshold. In the 0 to $1000nm$ range of study here, the overlay thickness is far below the threshold and the increase of the overlay thickness only raise the effective index of the cladding modes slightly. As the refractive index of the overlay increases to $n_3 = 1.55$ (Fig. 3.7b), and $n_3 = 1.65$ (Fig. 3.7c), the location of the mode reorganization zone moves into the overlay thickness range of the study and shifts from large overlay thickness to smaller values. This means that increasing the refractive index of the overlay (thus the refractive index difference between the overlay and the cladding)

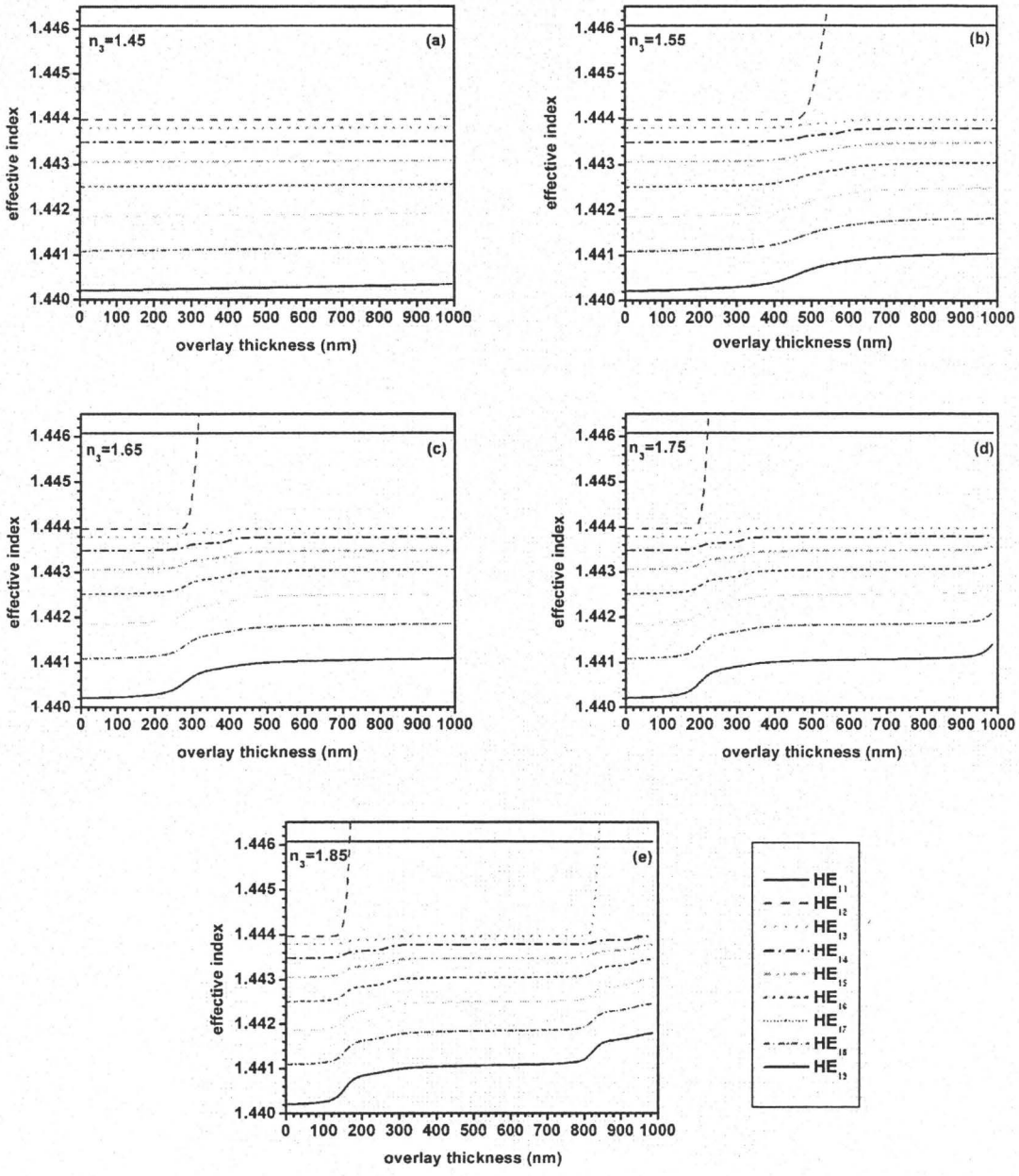

Figure 3.7 Effective indices of the lowest 9 light wave modes in an optical fiber with a high refractive index overlay on top of the fiber cladding where the refractive index of the overlay is $n_3 = 1.45$ (Fig. 3.7a), $n_3 = 1.55$ (Fig. 3.7b), $n_3 = 1.65$ (Fig. 3.7c), $n_3 = 1.75$ (Fig. 3.7d), and $n_3 = 1.85$ (Fig. 3.7e).

increases the wave guidance of the overlay which consequently induces mode reorganization at lower overlay thickness. When the refractive index of the overlay is increased further ($n_3 = 1.75$,Fig. 3.7d and $n_3 = 1.85$,Fig. 3.7e), the refractive index

contrast on the overlay is so large that it support the second mode reorganization zone in 0 to $1000nm$ overlay thickness range of the study.

3.2.3 Physics of mode reorganization

In order to have a better understanding on physics of the fiber guidance mode transition in the process of mode reorganization, we plot the amplitude of the transverse component of the electric field of the first nine HE_{1n} modes before the mode reorganization, during the time of the mode reorganization and after the mode reorganization. According to Fig. 3.7c, when the thickness of the overlay $d = 250\mu m$, the fiber waveguide works at a point before mode reorganization. In Fig. 3.8a, the mode distribution is similar to the mode distribution of a three layer fiber without the application of the high refractive index overlay. Except for the HE_{11} core mode, which locates only in the fiber core, all the cladding modes get their electric field distributed in both the fiber core and the fiber cladding with a small evanescent wave penetrating to the overlay and the ambient medium. Once the thickness of the overlay is increased to $300\mu m$, the cladding waveguide works right in the mode reorganization zone. As can be observed in Fig. 3.8c, the electric field of the HE_{12} mode migrates from the core-cladding region to the high refractive index overlay. In the meantime, the electric field distribution of all the higher order cladding modes shifts outwards from the cladding region to the high refractive index but is still confined by the cladding-overlay interface. There exist high amplitudes of the cladding modes at the interface of the cladding and the overlay and the electric field dropdown quickly in the overlay and the ambient medium. As a consequence, comparing Fig. 3.8d with Fig. 3.8b, when the fiber waveguiding condition is in the mode-reorganization, the amplitude of the electric field in the overlay is much higher than the time the fiber work point is out of the mode reorganization zone. When the thickness of the overlay increases further (see Fig. 3.8e), the outer most lobe of the cladding modes electric field migrates out of the cladding completely and are guided by the overlay. However, the amplitude of the electric field in the overlay and in the ambient turns out to be very small.

Based on the discussion above, the physical process of the mode reorganization in an optical fiber with a high refractive index overlay can be described as follows: When a high refractive index overlay is formed on top of the cladding, it provides a waveguiding channel for the lightwave. While the effective index of the overlay is small, or the overlay is not thick enough, the waveguiding provided by the overly somehow "sucks" the light wave field outward from the fiber cladding but is not sufficient to change significantly the field distribution of the cladding modes and change their effective index. As the refractive index and thickness increase to the value that bring the fiber to work in the mode reorganization zone, the waveguiding provided by the overlay has increased to be high enough so that it draws lots of the mode field to its region but was not able to support the field "oscillation" within it. The resulted high existence of the mode field in the overlay and the neighboring ambient means the effective index of the cladding modes are highly sensitive to the refractive index and thickness of the overlay as has been presented in Fig. 3.6 and Fig. 3.7. When the refractive index and/or thickness increase

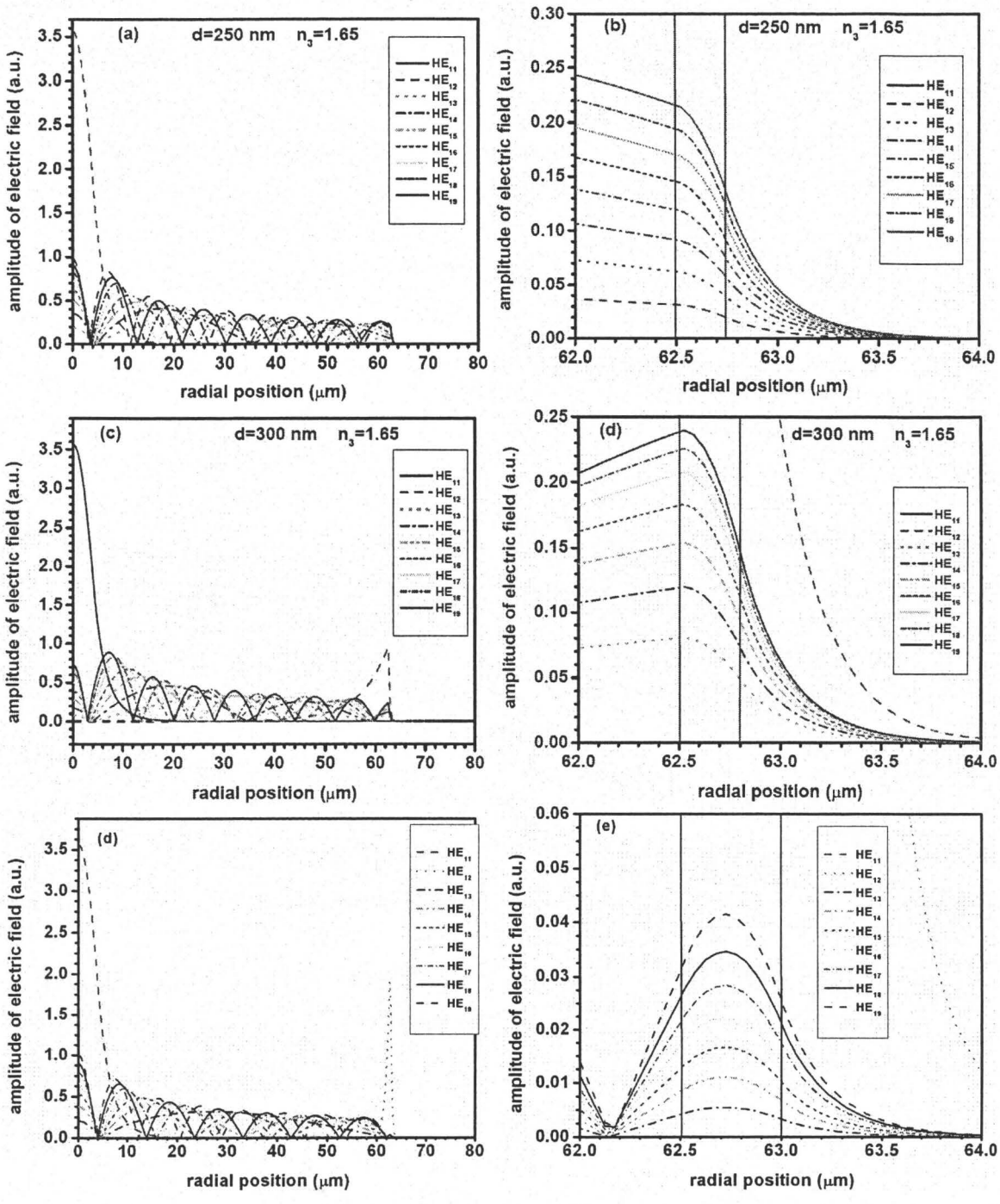

Figure3.8 Radial distribution of the amplitude of the electric field of the fiber mode in an optical fiber with a high refractive index ($n_3 = 1.65$) overlay of $250\mu m$ (a), $300\mu m$ (b) and $500\mu m$ (c) thick. Fig. 3.8b, Fig. 3.8d, and Fig. 3.8f are zoom in of Fig. 3.8a, Fig. 3.8c, Fig. 3.8e at the interfaces of the fiber cladding, the overlay and the ambient medium respectively. The black lines in Fig. 3.8b, Fig. 3.8d, and Fig. 3.8f represent the interfaces between the fiber cladding and the overlay, and the interface between the overlay and the ambient.

further and pass the mode reorganization zone, the overlay is then able to support the guiding of a complete "lobe" of the cladding field but the mode field relaxed to low amplitude in the overlay and in the ambient. As a consequence the dependence of the effective index of the cladding modes on the refractive index and thickness of the overlay drops off. At last, comparing Fig. 3.8e with Fig. 3.8a, one may find that the cladding mode field distribution of the HE_{1n+1} mode in the fiber core and cladding after mode reorganization highly resembles the mode field distribution of the HE_{1n} mode in the fiber core and cladding before mode reorganization. In other word, when the outer most "lobe" of the cladding mode field migrates to the overlay, the remained "lobes" of the mode field redistribute themselves in the fiber core and fiber cladding just like the distribution of the adjacent lower order cladding mode therein. Given the small amplitude of the outermost "lobe" of the field, the effective indices of the cladding modes (after mode reorganization) shift to the effective indices of the adjacent lower order cladding modes before mode reorganization.

3.3 Enhancement of cladding mode dependence on ambient refractive index with cladding structure modification

In Section 3.2, we have studied the dependence of the effective indices of fiber modes in an optical fiber with a high refractive index overlay and the mode reorganization therein. In this section we study the overlay application on enhancing the cladding mode dependence on the ambient refractive index. We first discuss the ambient refractive index dependence of the effective indices of the cladding modes of a fiber waveguide with an overlay of appropriate refractive index and thickness. Then, we will examine the outcome of a structure modification based on application of a high refractive index overlay on a cladding radius reduced fiber. At last, targeting at biochemical/chemical sensing, the enhancement of cladding modes dependence on the refractive index and thickness of bio-recognition film will be discussed.

3.3.1. Dependence of the effective indices of cladding modes on ambient refractive index in a fiber with overlay

As discussed in Section 3.1, to boost the dependence of the cladding modes on the ambient refractive index, it is necessary to intensify the evanescent wave of the cladding modes in the ambient refractive index. It has been noticed in Fig. 3.8d that when the fiber is set to work in the mode reorganization zone by selecting proper refractive index and thickness of the overlay, the mode field distribution in the overlay and in the ambient medium reaches high amplitude. The high existence of the evanescent wave in the ambient opens up the possibility of constructing a fiber waveguide with its cladding

mode highly dependent on the ambient refractive index. Therefore, one can increase the dependence of the cladding mode effective index on the ambient refractive index by applying an overlay to set the fiber work in the mode reorganization zone.

We assume an overlay with a refractive index of 1.65 is applied on top of a conventional fiber ($r_1 = 4.15\mu m$, $r_2 = 62.5\mu m$, $n_1 = 1.4448933$ and $n_2 = 1.444024$) and study the effective indices of the cladding modes as a function of the ambient refractive index. The simulation was carried out with the thickness of the overlay set between $100nm$ and $220nm$ to demonstrate fine-tune of the cladding mode dependence on the ambient refractive index with respect to the overlay parameter. The results of the simulation are presented in Fig. 3.9. For the purpose of clearance, Fig. 3.9 presents the effective index shift of the HE_{17} mode $n_{eff,HE_{17}}$ vs. the ambient refractive index (Fig. 3.9a)

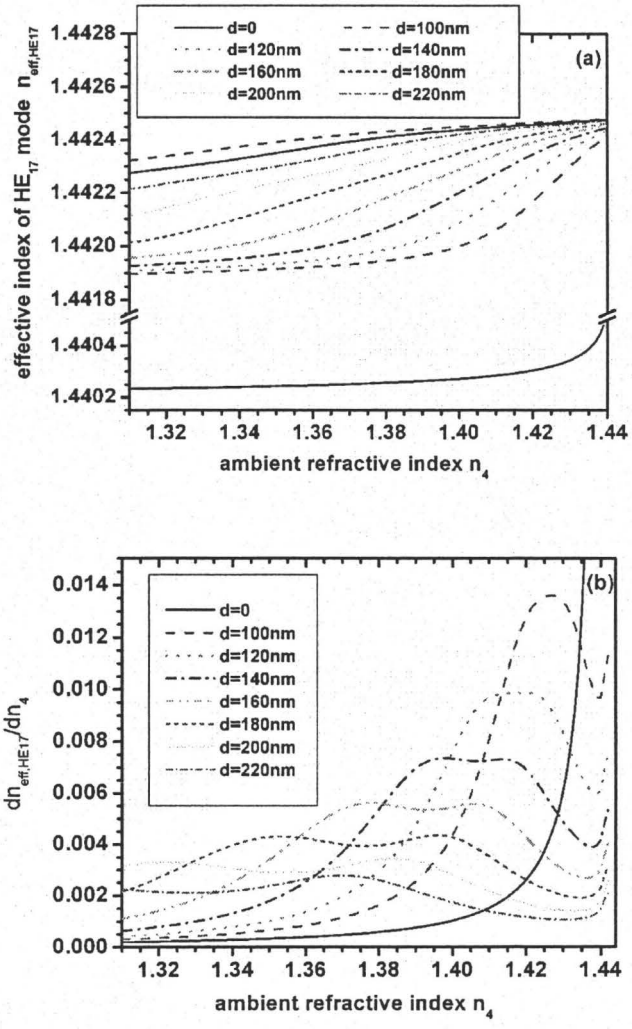

Figure 3.9 (a) Effective index of the HE_{17} mode in a fiber with an overlay of refractive index $n_3 = 1.65$ as a function of the ambient refractive index n_4, (b) differential of the effective index of the HE_{17} mode against ambient refractive index.

and the differential of $n_{eff,HE_{17}}$ against n_4 (Fig. 3.9b). The other cladding modes follow the same trend and are thus omitted here. It can be found in Fig. 3.9a that, similar to the case of changing the thickness and refractive index, when the ambient refractive index changes from 1.31 to 1.44, the waveguiding capability of the overlay changes. As a result, mode reorganization takes place when the ambient refractive index changes. By changing the thickness of the overlay from $100nm$ to $220nm$, the starting and ending effective index of the HE_{17} mode does not change with the overlay thickness, but the onset of the mode reorganization can be offset from $n_4 \approx 1.4$ (when $d = 100nm$) to $n_4 \approx 1.31$ ($d = 180nm$) and even further as the thickness of the overlay d increase further to $200nm$ and $220nm$. When the overlay thickness is small, the mode reorganization happens in a very small ambient refractive index range with high refractive index value close to the cladding layer (see Fig3.9b). As the thickness of the overlay increase, two phenomena can be observed: First, the mode reorganization zone shifts to the lower value on the ambient refractive index axis. Secondly, the span of the mode reorganization zone on the ambient refractive index axis is broadened. The dependence of the cladding effective indices to the change of the ambient refractive index at low ambient refractive index can thus be enhanced by application of an overlay with proper thickness and refractive index. In the study presented in Fig. 3.9, as compared to a bare fiber without overlay, when the cladding radius is set to $220\mu m$, the dependence of the effective index of the HE_7 mode on the ambient refractive index is enhanced by 15 folds.

3.3.2. High refractive index overlay on a cladding radius reduced fiber

In 3.3.1, we have theoretically presented that the change of the ambient refractive index can change the waveguiding capability of the overlay and thus induce mode reorganization of the cladding modes. The large effective index shift of the cladding modes in the mode reorganization zone enables ambient refractive index sensing based on the cladding mode effective index dependence on the ambient refractive index. For a lot of applications further boosting of such dependence is demanded. In this part of study, further enhancement is done by reducing the cladding layer radius beneath the overlay. Recall the study carried out in Section 3.1, reducing of the cladding layer radius not only increases the dependence of the cladding mode effective index on the ambient refractive index but also enlarges the difference of the effective indices between neighboring *HE* modes. We have concluded that the mode reorganization of the cladding modes is largely determined by the waveguiding capability of the overlay. Therefore, the reduction of the cladding layer radius will not change the start and end point of the mode reorganization, but increase the starting and ending value of the effective indices. As a result, the dependence of the cladding mode indices will be further enhanced. In Fig. 3.10, the effective index shift of the HE_{17} mode $n_{eff,HE_{17}}$ with the ambient refractive index (Fig. 3.10a) and the differential of $n_{eff,HE_{17}}$ against n_4 (Fig. 3.10b) are presented. All the parameters used in the simulation are the same as those used in 3.3.1 except that the

cladding layer radius is reduced from $62.5\mu m$ to $22.5\mu m$. Comparing Fig. 3.10 with Fig. 3.9, the enhancement of the dependence of the effective index of HE_{17} mode on the

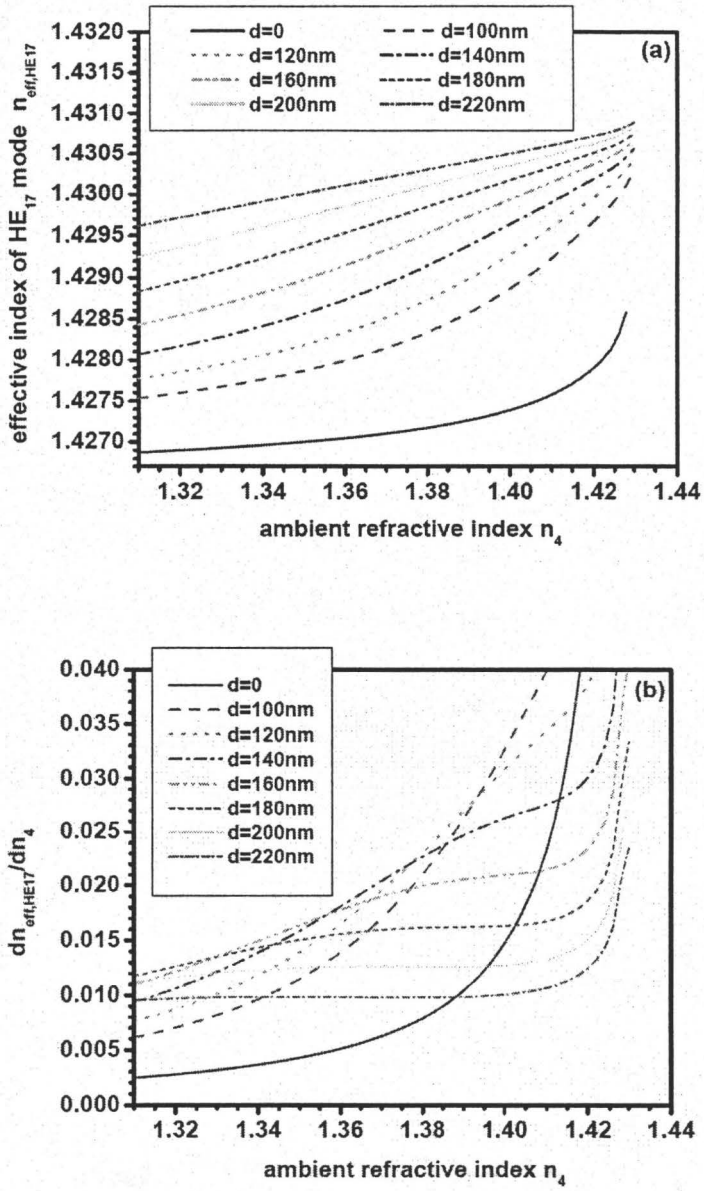

Figure 3.10 (a) Effective index of the HE_{17} mode in a fiber with an overlay of refractive index $n_3 = 1.65$ on a cladding reduced fiber ($r_2 = 22.5\mu m$) as a function of the ambient refractive index n_4, (b) differential of the effective index of the HE_{17} mode against ambient refractive index.

ambient refractive index is obvious. For ambient refractive index $n_4 = 1.318$ the differential of the effective index of HE_{17} mode against the ambient refractive index n_4 is 0.0118, which represent 3.7 folds enhancement as compared to the dependence achieved by a fiber without cladding reduction (0.00316). Combining the dependence enhancement obtained by application of high refractive index overlay and by reducing the fiber

cladding radius to $22.5\mu m$, a total enhancement of 60 folds is achievable for the HE_{17} mode.

3.3.3. Refractive index sensing of chemical/biochemical recognition film with cladding structure modified fiber

As has been described in Chapter 1, for chemical/biochemical sensing, a layer of bio-recognition is usually applied on top of the chemical-physical transducer to capture the target molecule in the analyte. In evanescent wave based optical biosensor, the confinement factor of the mode field in the sensing layer determines the sensitivity of the sensor. However, because of the nature of the bio-recognition film, the thickness of the sensing film is often small, which brings in small existence of the evanescent wave in the film and limit the dependence of the cladding modes on the film parameter (thickness and/or refractive index) change. According to our analysis above, its has been revealed that the dependence of the effective indices of the cladding modes on the ambient refractive index can be greatly enhanced by properly select the thickness and refractive index of the overlay to bring the cladding modes work in the mode reorganization zone and by reducing the cladding layer radius to increase the neighboring cladding effective index difference. The same principle can be applied to the detection of the refractive index or thickness of the bio-recognition sensing layer immobilized on the fiber surface as well. To examine the effect, we assume a bio-recognition film has a thickness of $10nm$ and a refractive index will change in a range of 1.45 ~1.65 and study the dependence of the effective indices on the film refractive index change. Four situations were studied: 1. direct immobilization on pristine fiber without structure modification, 2. immobilization on a fiber with cladding radius reduced to $22.5\mu m$, 3. immobilization on an overlay on top of a pristine fiber, 4. combination of 2 and 3. To keep consistency with the simulations described above and to make the results comparable to the study of ambient refractive index change, we keep all the parameters of the fiber the same as stated before unless otherwise mentioned.

Simulation results are given in Fig. 3.11. It can be found in Fig. 3.11a, since the thickness of the sensing film is small, the existence of the evanescent wave in the sensing layer is small, and thus modulation of the effective indices by the sensing layer refractive index is week. As a consequence, the response of the cladding modes effective indices to the sensing film refractive index change is extremely low (at $10^{-6} \sim 10^{-5}$ level). In addition, the curve showing dependence of the effective indices of the cladding modes on the ambient refractive index is quite flat across the whole range of the sensing layer refractive index under study. When the radius of the cladding layer is reduced to $22.5\mu m$ (Fig. 3.11b), or by applying the high refractive index overlay (Fig. 3.11c), the dependence of the effective indices of the cladding modes to the sensing layer index change are greatly enhanced. Combining these two effects (Fig. 3.11d), the dependence of the effective indices on the sensing layer refractive index change is further enhanced. However, it can be found that because the enhancement is greater to the lower order modes, the effective index of the lower order modes is scaled up and the dependence of the 5^{th}, 6^{th}, 7^{th}, 8^{th} and 9^{th} mode on the sensing film refractive index becomes very small. In other word, with both cladding reduction and overlay application, all these modes have

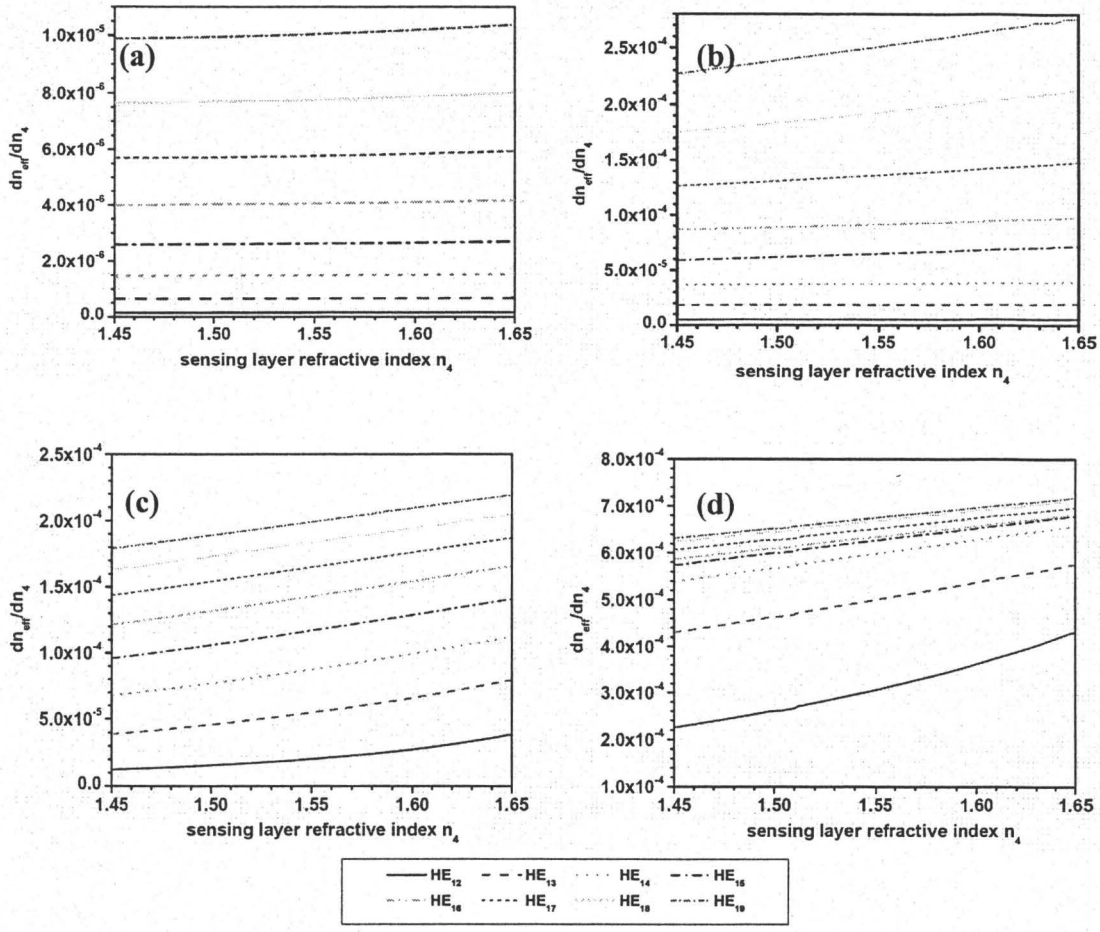

Figure 3.11 Dependence of the cladding mode effective indices on the refractive index change of the sensing layer immobilized on the surface of the fiber. (a) sensing layer immobilized on pristine fiber; (b) sensing layer immobilized on a fiber with the cladding layer radius reduced to $22.5\mu m$; (c) sensing layer immobilized on top of overlay; (d) sensing layer immobilized on top of an overlay ($n_3 = 1.65$, $d = 180nm$) formed on a cladding layer reduced fiber ($22.5\mu m$). The sensing layer is assumed to have a thickness of $10nm$.

similar dependence on the sensing film index change. The value of the dependence of the effective index on the sensing film refractive index change achieved by combining those two techniques is $\sim 6.00\times10^{-4}$.

In conclusion, in this section we have systematically studied the dependence of the effective indices of the cladding modes on the refractive index of the ambient and the sensing layer. The dependence is enhanced by modification of the cladding structure through reducing the radius of the cladding layer and applying a high refractive index overlay. The physics behind the dependence enhancement is explained by studying the mode field distribution in the ambient and the sensing layer. The existence of the mode

field in the medium to be analyzed is responsible to the dependence of the effective indices of the cladding modes on the refractive index change to be measured.

3.4 Application of cladding structure modification to long period grating refractive index sensor.

In a fiber optic sensor, the effective indices of cladding modes of the optical fiber are intrinsic parameters and cannot be physically measured. In order to experimentally characterize the dependence of the effective indices of the cladding modes, the change in the effective index must be converted to measurable physical parameters such as wavelength. In the long period grating based fiber sensor, this is realized by two means. In the first method, the effective index change is converted to the resonance wavelength of the core mode-cladding mode resonance by the phase matching condition given by Eq. 2.35. In the second method, the effective index change of cladding modes is converted to the relative phase shift between the cladding modes and the core mode. In this section, as an application of the results obtained in Section 3.1 and Section 3.2, we study the effect of the cladding modification on the sensing properties of a long period grating with a cladding modified structure.

For a wavelength modulated long period grating , the sensitivity of the sensor is evaluated by the resonant wavelength shift $d\lambda_{notch}$ against the refractive index change of the analyte $n_{analyte}$:

$$S = \frac{d\lambda_{notch}}{dn_{analyte}} \tag{3.3}$$

When the long period grating is used to measure the refractive index of the ambient, the analyte is the ambient medium, and the sensitivity of the notch wavelength shift to the ambient index change can thus be written as:

$$S_{amb} = \frac{d\lambda_{notch}}{dn_{amb}} \tag{3.4}$$

Substituting Eq. 2.35 into Eq.3.4 (note that because of the large cladding radius as compared to the core mode radius, the core mode is hardly affected by the ambient refractive index), the sensitivity of the long period grating refractive index sensor can be represented as:

$$\begin{aligned} S_{amb} &= \left| d\lambda_{11-1m}^{co-cl} / dn_{amb} \right| \\ &= \Lambda \cdot dn_{eff,1m} / dn_{amb} \end{aligned} \tag{3.5}$$

From Eq. 3.5, to optimize the sensitivity of long period grating refractive index sensor, one need to increase the dependence of the cladding mode effective indices on the ambient refractive index, and the period of the long period grating. However, considering practical applications, two prerequisites are applied in the sensitivity optimization: first, the notch wavelength must be in the 1000 *nm*-1610 *nm* wavelength range, where the fiber optic component and measurement instrument are most available; second, the depth of

the notch must be large enough for the notch wavelength detection. The parameters that can be used in the sensitivity optimization process include the period of the long period grating Λ, the cladding layer radius r_2, and the order of cladding mode m.

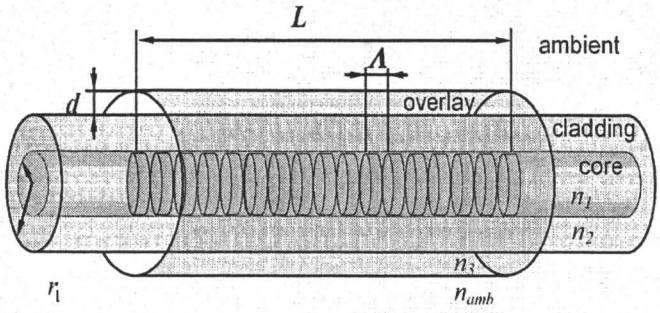

Figure 3.12 Schematic structure of the modified long period grating refractive index sensor.

3.4.1. Enhancing sensitivity of long period grating refractive index with cladding structure modification

The structure of the long period grating refractive index sensor under study is defined in Fig. 3.12. Given the broadband spectrum feature of the long period grating, material and waveguide dispersion properties of the optical fiber is considered. The refractive index of fiber core and fiber cladding is given by the Sellmeier equation for GeO_2-SiO_2 glass system [75], where the fiber cladding is pure SiO_2 and the fiber core is doped with 3.27 mole % GeO_2 . The radius of the fiber core was fixed at $4.15\mu m$. The other parameters of the fiber, i.e. cladding radius r_2, refractive index and thickness of the overlay, and refractive index of the ambient were set as variables in our previous study.

We first studied the dependence of the sensitivity on the grating period. According to Eq. 3.5, the sensitivity of the long period grating is proportional to the period of the long period grating. In other words, the larger the grating period, the higher the sensitivity produced by the long period grating sensor is. Based on Eq.2.35, however, the notch wavelength increases with the grating period as well. As restricted by prerequisite 1, the notch wavelength of the notch structure under study must be within the 1000 nm ~1600 nm wavelength range as the ambient refractive index varies in its entire range of 1.0 ~ 1.4. In this study we set the period of the grating as an adaptive parameter in the optimization so that when the $n_{amb} = 1.318$, the notch wavelength of the cladding mode under study is equal to $1550nm$. In such a case, the grating period is given by:

$$\Lambda = 1550nm \Big/ \left(n_{eff,11} - n_{eff,1m} \right) \Big|_{n_{amb}=1.318} \tag{3.6}$$

TABLE 3.1 Optimized parameters for different order cladding mode resonance

Cladding mode order	3	4	5	6	7
dn_{eff}/dn_{amb} ($\times 10^{-3}$)	1.65	2.04	2.44	2.79	3.07
Grating period (μm)	693.2	620.0	538.9	460.7	391.2
Sensitivity (*nm/refractive index*)	1148	1263	1316	1287	1203

Furthermore, unless otherwise specified, the grating period adaptation is always taken in the rest of this section. Next, we examined the effect of the order of the cladding mode on the sensitivity of the long period grating sensors. Table 3.1 shows the slope of the effective index response curve of a long period grating sensor on the ambient refractive index change, the calculated value of the grating period Λ from Eq. 3.57, and the corresponding sensitivity of the $HE_{13} - HE_7$ cladding modes. Here, $r_2 = 62.5\mu m$ and the ambient refractive index $n_{amb} = 1.33$ were assumed, with which the long period grating sensor works in the mode reorganization zone. All the other parameters used in the calculations were the same as those specified in Section 3.3. Note in Table 3.1 that, as expected, the slope of the cladding mode effective index curve dn_{eff}/dn_{amb} increases with the ascendance of the order of the cladding mode. However, after the grating period adaptation is applied, the grating periods decrease with the increase of the cladding mode order. As has been studied in Section 3.3, the inter-modal effective index difference increases with the order of the cladding modes. Consequently, the effective index shifts as a result of the mode reorganization is enhanced, leading to a higher slope in the $n_{eff} - n_{amb}$ curve. On the other hand, the difference between the effective index of the core mode and the effective indices of the cladding modes increase with the order of the cladding mode. After the grating period adaptation, the optimal grating period for high order cladding mode is smaller than the optimal grating period for the low order cladding mode. Since the sensitivity is proportional to the product of the grating period and the slope of the $n_{eff} - n_{amb}$ curve (see Eq. 3.5), the highest sensitivity is obtained from the 5th order cladding mode. This result is contrary to the case with a fixed grating period in which the highest sensitivity is achieved for the highest cladding mode [37].

Furthermore, to gain a clear understanding of the dependence of the optimized parameters on the cladding radius, evolution of the slope of the $n_{eff} - n_{amb}$ curve was investigated when the cladding radius was varied. In the simulations, all the long period grating parameters were the same as those used in the cladding mode order study except that this time the cladding radius r_2 varied from $62.5\mu m$ to $10\mu m$. The calculated results of dn_{eff}/dn_{amb}, the grating periods, and the sensitivities of the cladding modes are shown in Fig. 3.13a, Fig. 3.13b and Fig. 3.13c respectively. As shown in Fig. 1.13a, when the radius of the cladding layer r_2 is reduced from $62.5\mu m$ to $10\mu m$, the optimized grating periods for all orders of cladding mode decrease with r_2. On the other hand, it can be seen from Fig. 3.13b, the dependence of the slope of the $n_{eff} - n_{amb}$ curve increases with the reduction of r_2. As a result, it is found from Fig. 3.13c that when the radius of the cladding layer is reduced from $62.5\mu m$ to $10\mu m$, for each of the cladding modes, there exists an optimized cladding radius, at which the sensitivity of the corresponding cladding mode notch wavelength shift reaches a maximum. The sequence for the cladding modes to reach the optimized point with the reduction of the cladding radius is in reverse to the order of the cladding mode, i.e. the higher order cladding mode reaches the optimized operation cladding radius at a larger cladding radius. In the meantime, the maximum value of the optimized sensitivities for each cladding mode decreases with the

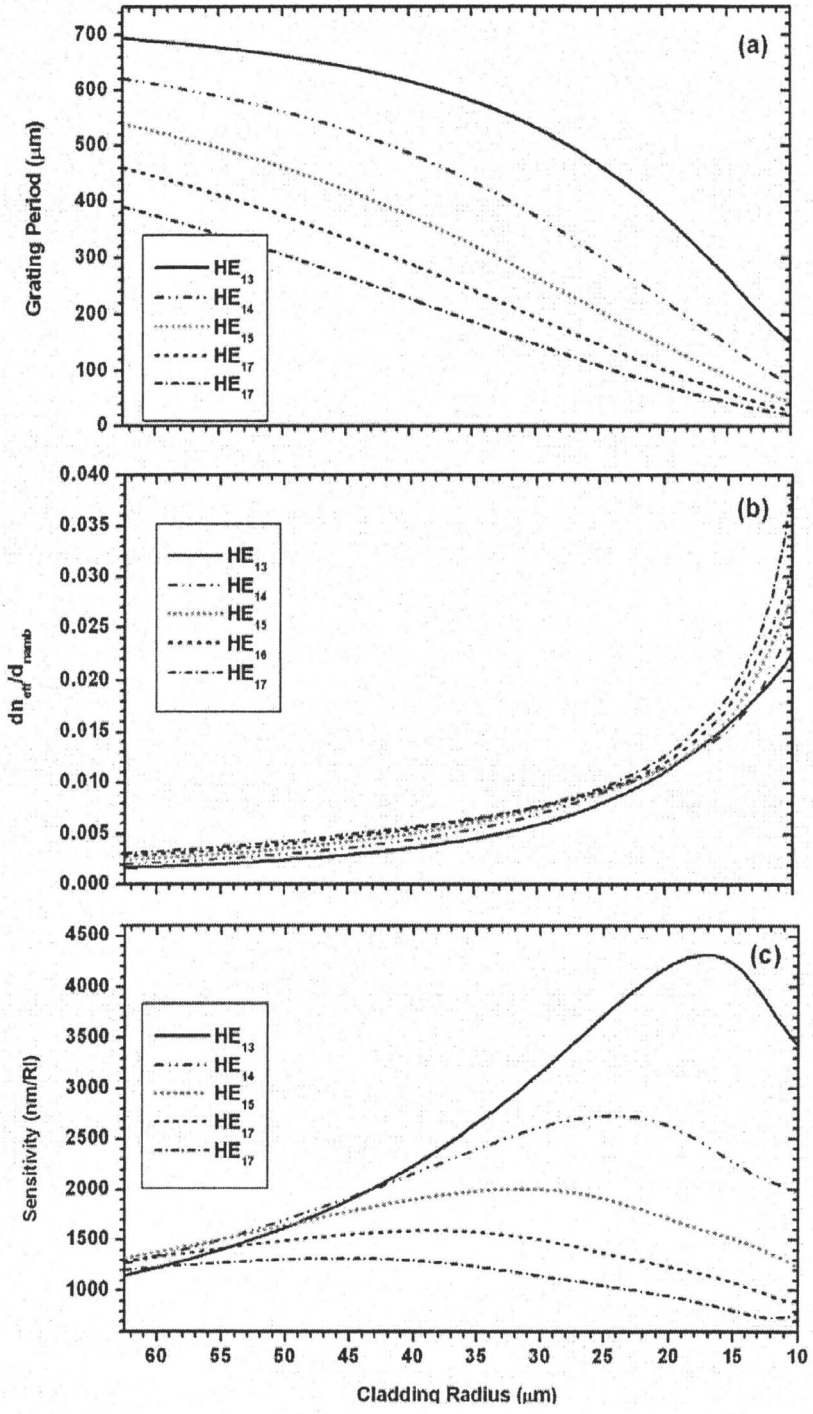

Figure3.13 Evolution of (a) grating period, (b) dn_{eff}/dn_{amb}, (c) sensitivity of long period grating refractive index sensor to ambient refractive index for a structure modified long period grating sensor with different cladding layer radius r_2.

the increase of the order of cladding mode, indicating that by utilizing the period adaptation technique, higher sensitivity can be obtained from the lower order cladding mode resonance of the structure modified long period grating in which the cladding radius is reduced. For example, in Fig. 3.13c, the HE_{17} mode reaches its maximum sensitivity when $r_2 = 45.5\mu m$, the corresponding maximum sensitivity is $1314.9nm/RI$, while for the HE_{16}, HE_{15}, HE_{14} and HE_{13} mode notch wavelength shift, the maximum sensitivity is obtained at $38.5\mu m$, $31.5\mu m$, $24.5\mu m$, and $17.5\mu m$ with a maximum sensitivity of $1331.0nm/RI$, $2005.8nm/RI$, $2728.8nm/RI$, $4309.2nm/RI$ respectively. Obviously, $4309.2nm/RI$ (obtained from the HE_{13} mode notch wavelength) is the largest value achievable from the structure modified long period grating refractive index sensors.

Based on the simulation results described above, a process to optimize a structure modified long period grating refractive index sensor is summarized as follows. First, based on the refractive index of the overlay and the approximate value of the ambient refractive index, the overlay thickness is calculated to tune long period grating sensor to work in the mode reorganization zone. Second, the effective index of the HE_{13} mode as the function of the cladding radius and the ambient refractive index is calculated. Third, the sensitivity of the HE_{13} mode notch wavelength to the ambient refractive index is calculated with Eq. 3.5, where the grating period Λ is obtained with the grating period adaptation expressed in Eq. 2.35. The cladding layer radius can thus be optimized by setting the cladding radius to a value so that the maximum sensitivity can be achieved.

3.4.2. Material dispersion and phase match condition

To rigorously determine the notch wavelength of the long period grating refractive index sensor and its sensitivity on the ambient refractive index, the notch wavelength of the long period grating is obtained by solving the phase matching condition (Eq. 2.35), taking into account the material dispersion. Fig. 3.14 shows graphic solution of the phase match condition. In Fig. 3.14, the calculated value of function $F(\lambda) = \Lambda\left[n_{eff,co}(\lambda) - n_{eff,cl}(\lambda)\right] - \lambda$ is plotted as a function of wavelength. The resonant notch wavelength is given by the zero-cross points where the curves cross-over the horizontal axis $F(\lambda) = 0$. Figure 3.14a gives the curves that determine the notch wavelength of the HE_{17} mode with the cladding radius equal overlay. In Fig. 3.14b the curves of the HE_{17} mode resonance with the cladding radius value set at 17.5 μm is given.

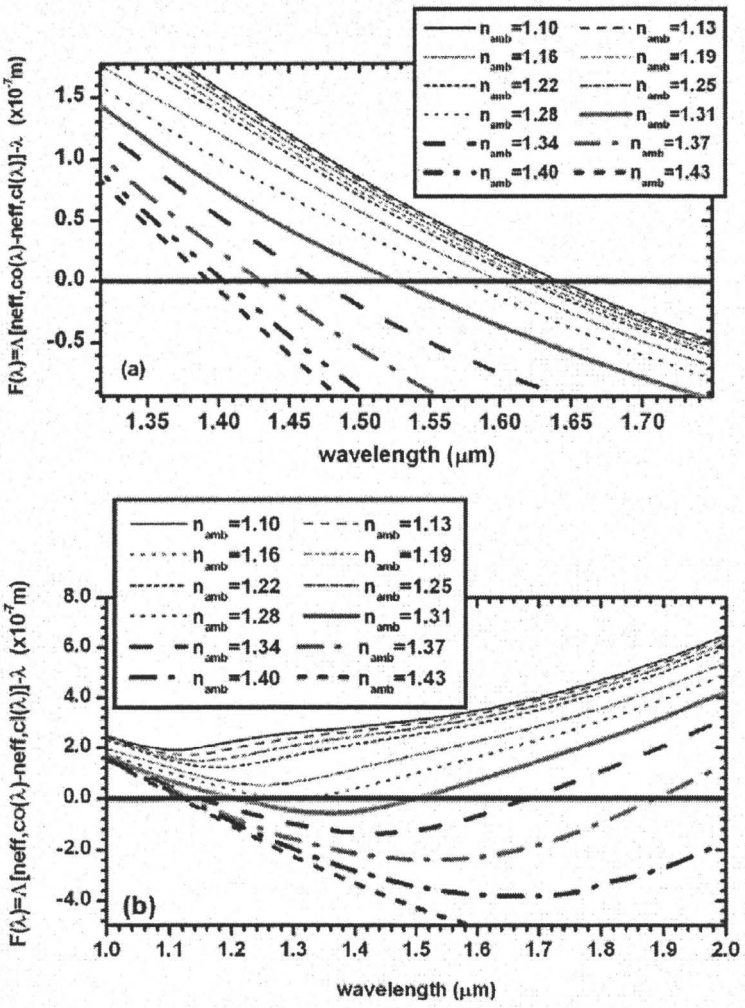

Figure 3.14 Graphic solution of the phase match condition equation with different ambient refractive index. (a). HE_{17} mode with $r_2 = 62.5\mu m$, and $\Lambda = 391\mu m$, (b) HE_{17} mode with $r_2 = 17.5\mu m$, and $\Lambda = 325\mu m$. The resonant wavelength is given by the zero-cross point of function $F(\lambda) = \Lambda\left[n_{eff,co}(\lambda) - n_{eff,cl}(\lambda)\right] - \lambda$.

According to the simulation results shown in Section 3.4.1, this cladding radius gives the maximum sensitivity to the HE_{13} mode resonance. The grating period of the HE_{17} mode resonance and the HE_{13} mode resonance in Fig. 3.14a and Fig. 3.14b are adapted to $391\mu m$ and $325\mu m$ respectively. As shown in Fig. 3.14a, when the ambient refractive index increases from 1.1 to 1.44, the calculated phase matching wavelength curve shift down on the vertical axis. Consequently, the resonant wavelength of the long period grating on the horizontal axis shifts from $1642nm$ to $1392nm$. The mode reorganization due to the ambient refractive index change is represented by the large down shift of the curves when the ambient refractive index is around 1.28-1.37. As a result, the notch wavelength shifts to the short wavelength quickly, leading to a high sensitivity region. In the meantime, due to dispersion, the phase matching wavelength curves in Fig. 3.14b

does not have intersection with the bold line, when the ambient refractive index is less than 1.28. No phase matching between the HE_{13} mode and the HE_{11} mode can be established and thus no notch structure corresponding to the $HE_{13} - HE_{11}$ mode resonance can be observed on the transmission of the long period grating. When the ambient refractive index is greater than 1.28, each phase matching wavelength curves has two cross point with the horizontal axis. Each of the cross point is corresponding to one notch structure in the transmission spectrum of long period grating and thus two notch structure due to the HE_{13} cladding mode resonance is observed in the transmission spectrum [39]. As the ambient refractive index increases from 1.28 to 1.43, the resonant notch with shorter wavelength experiences a blue shift from $1295nm$ to $1115nm$ and the resonant notch of the longer wavelength shows a red shift from $1295nm$ to more than $2000nm$. Noting the scale difference between Fig. 3.14a and Fig. 3.14b, the red shift of the long wavelength branch of the HE_{13} mode resonance in Fig. 3.16b as a function of the ambient refractive index in the structure modified long period grating is much faster than the blue shift of HE_{17} mode in the conventional long period grating refractive index sensor, indicating sensitivity enhancement by the structure modification.

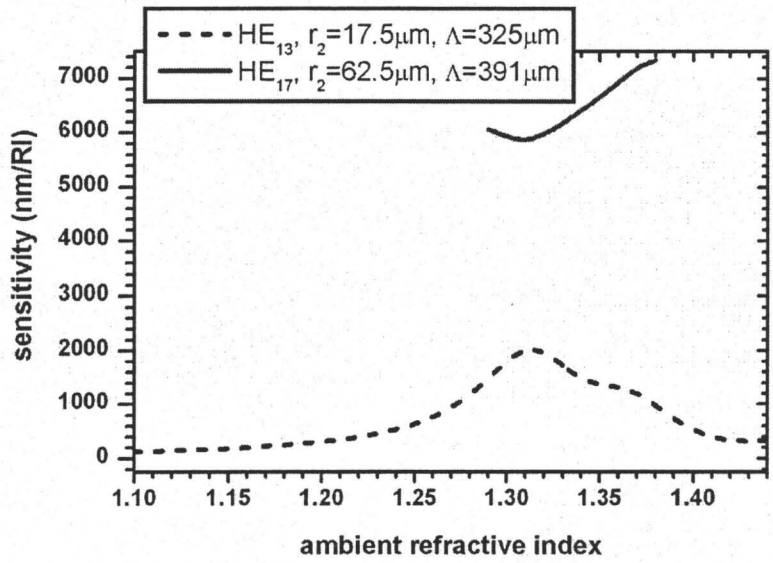

Figure3.15 Dependence of sensitivity of notch wavelengths shift of the HE_{13} mode on the ambient RI for a cladding layer radius reduced LPG (solid line) and dependence of sensitivity of notch wavelengths shift of HE_{17} mode on the ambient refractive index for a cladding layer unreduced long period grating.

Figure 3.15 demonstrates the effects of an optimized long period grating refractive index sensor is plotted as a solid line, in which the sensitivity-ambient refractive index curve of the HE_{13} mode in a cladding reduced long period grating sensor with a high refractive index overlay.. As a comparison, the sensitivity-ambient refractive index curves obtained from HE_{13} mode by the long period grating structure reported in [37] is plotted in the same graph as well. Obviously, with the cladding layer radius reduction and the grating

period adaptation, the sensitivity of the long wavelength branch of the HE_{13} mode notch wavelength shifting to the ambient refractive index is greatly enhanced as compared to the HE_{17} mode notch wavelength shifting in the reported conventional long period grating refractive index sensor [37]. For the structure under our study, a sensitivity as high as $5980nm/RI$ can be obtained from the HE_{13} mode resonance, which is 3 times higher than the value obtained from the HE_{17} mode resonance (i.e. $1989nm/RI$) with the reported long period grating sensor structure.

It is worth noting that in the conventional long period grating sensors, the coupling between the core mode and the low order cladding mode (i.e. HE_{12}, HE_{13} modes) is so low that the notch of the low order cladding mode is very shallow (~0.5dB). In real experiments, a shallow resonance notch structure produces a large noise and thus results in low sensing accuracy. It is thus a logical concern if the coupling between the core mode and the low order cladding mode is strong enough to generate a deep enough notch for experimental detection. To justify the use of the low order cladding mode resonance in long period grating refractive index sensing, the depth of the notches was studied by calculating the coupling constant between the core mode and the corresponding cladding mode. In most of weak long period grating ($\kappa_{11-1m}L < \pi/2$), the notch depth is an increasing function of the coupling constant, thus it can be used as the parameter to evaluate the notch depth. The coupling constant variation between the core mode and the HE_{13} to HE_{17} cladding mode as a function of the ambient refractive index in a cladding reduced long period grating sensor ($r_2 = 30\mu m$) is shown in Fig. 3.16a, which is given in a form of coupling constant/Δn, where Δn is the amplitude of refractive index modulation in the fiber core. As a comparison, the coupling constant of a cladding radius unreduced long period grating sensor ($r_2 = 62.5\mu m$) is also provided in Fig. 3.16b. Comparing Fig. 3.16a with Fig. 3.16b, it is found that when the cladding radius is reduced to $30\mu m$, the coupling constant for the low order cladding modes (HE_{13}, HE_{14} mode) are boosted by 2 folds. This indicates that cladding radius reduction not only enhances the sensitivity of the long period grating, but also deepens the notch structure for easy detection. Additionally, unlike the cladding unreduced long period grating sensor, where the coupling constants of all the cladding modes drop toward the adjacent lower cladding mode, the coupling of the low order cladding mode with the core mode intensifies with the ambient refractive index, giving rise to a deeper notch structure until the cladding mode reach its cutoff. It is worth noting that it has been observed experimentally that for a long period grating coated with a high refractive index overlay, when the long period grating refractive index sensor with a high refractive index overlay works in the most sensitive range, the notch depth drops so severely that the notch structure disappears in the long period grating transmission spectrum. The discrepancy between the results obtained in experiments and simulations might be attributed to the high loss of the coated overlay used in the experiments and the loss in the ambient material as pointed out by Cusano et al [74].

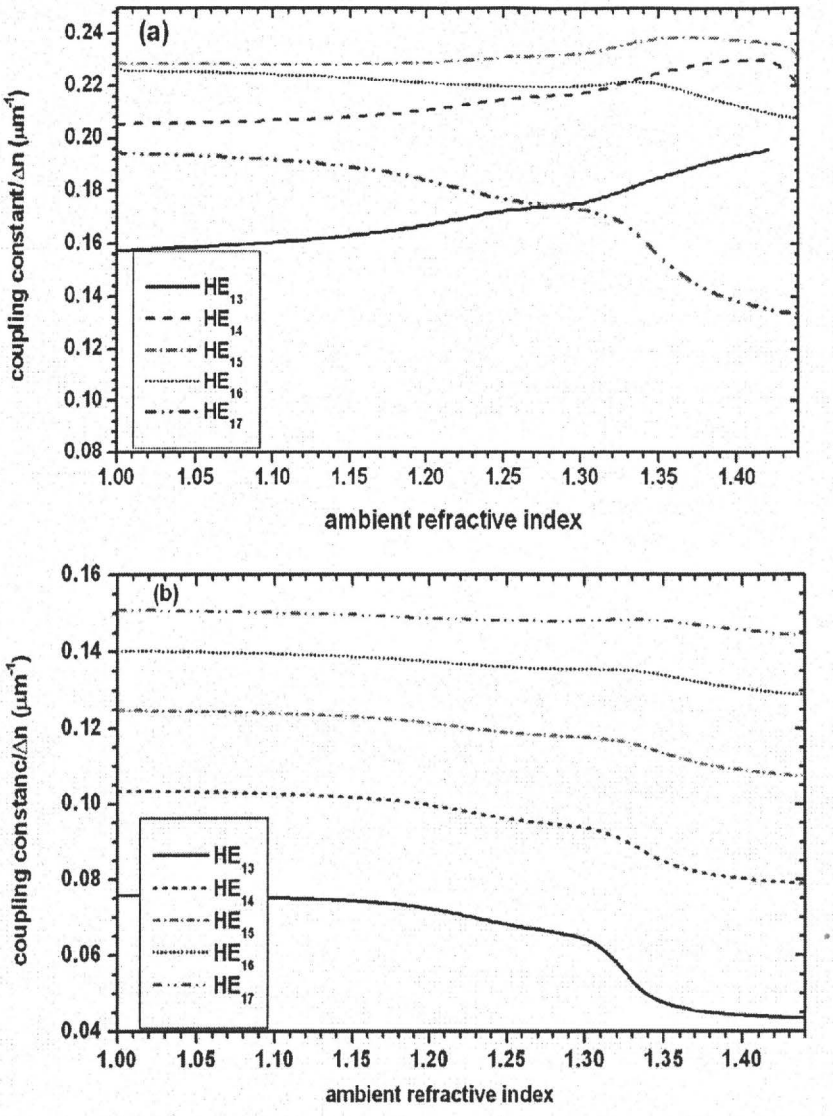

Figure3.16 Coupling constant κ_{11-1m} divided by the core refractive index modulation Δn of the $HE_{13} \sim HE_{17}$ cladding modes over the change of refractive index as a function of the ambient refractive index in a fiber long period grating with a cladding radius (a), $r_2 = 30.0\mu m$, and (b) $r_2 = 62.5\mu m$.

In this section we propose a new process to optimize the sensitivity of a structure modified long period grating sensor to the ambient refractive index. By reducing cladding radius, keeping the grating period as an adaptive parameter and employing the HE_{13} mode notch wavelength shift, the sensitivity of a long period grating refractive index sensor coated with high refractive index overlay is greatly enhanced. It is shown that an ambient refractive index sensitivity as large as $5980nm/RI$ can be achieved with a structure modified long period grating refractive index sensor, representing a 3-folds sensitivity enhancement as compared to the best result obtained from reported structures in which the high order HE_{17} mode resonate notch wavelength was employed. In addition, the low order cladding mode resonance notch depth has been examined by studying the coupling constant between the core mode and the cladding mode. The results suggest that the low order cladding mode resonance notch structure should be measurable if a low-loss overlay is employed in the experiment.

Chapter 4
Long-Period Grating in-fiber Michelson Interferometer

4.1 Introduction

In Chapter 2 and Chapter 3, we have studied the theory of long period grating and the dependence of the cladding mode effective indices on the refractive index of the ambient medium and the sensing layer immobilized on the surface of the fiber. Combining the knowledge obtained from the cladding mode study with fiber grating theory, we were able to study the notch wavelength dependence of the cladding mode resonance and thus its sensitivity to refractive index change. However, associated with the nature of long period grating, there are several drawbacks of long period grating in the application as a refractive index sensor. First, a long period grating is a two-port device, meaning that the characterization must be carried out by measuring the transmission spectrum of the device. Because of the high sensitivity of its transmission spectrum to mechanical bending, application of long period grating such as refractive index measurement needs complex fixture and fluid manipulation apparatus to inject the measurand on the fiber surface and lead the optical lightwave in and out of the sensor. Second, the refractive index change of the measurand is modulated on the center wavelength of the absorption notch in the transmission spectrum of the long period grating, which is a broadband notch structure. Due to the existence of spectral intensity noise from either the light source intensity fluctuation or the detector noise, accuracy of the notch wavelength determination is low due to the relatively flat bottom of the notch structure in the transmission spectrum of long period grating. At last, the mechanism of direct application of long period gratings in sensing is based on the shift of the phase matching condition, i.e. the resonant notch wavelength. As has been analyzed in Section 3.4, when cladding structure modification is applied to the long period grating device to enhance the sensitivity, the notch wavelength will be displaced out of the conventional optical communication wavelength window, where the fiber optic component is most available. In an ideal case, a mechanism to dissociate the link between the sensitivity enhancement and the notch wavelength is preferred.

The long period grating in-fiber Michelson interferometer studied in this chapter is based on low coherence reflection spectrum formed by the interference between the light waves from the core mode and the cladding mode. Because the signal is modulated in reflection spectrum, the sensor is a single-end device and thus easy to be configured into an optrode for refractive index based chemical/biochemical sensor. In addition, the narrow spectrum feature of the interference fringe in the low coherence reflection spectrum improves the resolution of the wavelength shift in the signal interrogation. At last, the Michelson interferometer works on the relative phase change between the core

mode and the cladding modes in which the long period grating only functions as a beam splitter in the interferometer and not involved in the signal transducing. There are two benefits from this configuration: first, when the long period grating is not involved in the signal transducing, modification of the cladding layer structure in the arms of the in-fiber Michelson interferometer does not affect the resonance wavelength of the long period grating. As a result, one can utilized high order cladding mode and do the cladding layer structure modification simultaneously. Secondly, separation of the sensing fiber from the long period grating make it possible to engineering the sensor head of the in-fiber Michelson interferometer into a disposable parts for chemical/biochemical sensor since the expensive long period grating is not part of the sensor head any more.

The rest of the chapter will be organized in the following way: In Section 4.2, the working principle of the long period grating in-fiber Michelson interferometer is given, followed by the theoretical simulation of the device. The experimental fabrication of the device is presented in Section 4.3. At last, Section 4.4 studies the responses of the refractive index sensor fabricated in Section 4.3 to the refractive index change of the ambient by immerse the sensor head in aqueous solution of glycerin with different concentration.

4.2 Operation principle and modeling of long period grating in-fiber Michelson interferometer

4.2.1 Operation principle of long period grating in-fiber Michelson interferometer

The structure and optical path of a long period grating in-fiber Michelson interferometer is depicted in Fig. 4.1. A long period grating in-fiber Michelson interferometer consists of a long-period grating (usually with a transmission ~3 dB at designated wavelength) followed by a mirror formed on the distal end of the fiber after the long period grating. When the lightwave propagating in the fiber core encounters a long period grating with 3 dB coupling strength from the left, part of the light is coupled into the cladding while the remaining light wave continues to travel in the core of the fiber. Upon impinging the metallic mirror formed on the cleaved tip of the fiber, the light wave propagating in both the fiber core and the fiber cladding are reflected back towards the long period grating following their incoming route. At the long period grating, part of the light wave of the core mode is coupled from the fiber core to the cladding mode while others remain in the core mode. In the similar way, the light wave of the cladding mode is spitted into core mode propagation and cladding mode propagation as well. Both waves propagating in the fiber core originate from the injected light wave from the fiber core but propagate through different path and thus interfere with each other in the fiber core. As a consequence, the reflection spectrum of a long period grating consists of a fast oscillating pattern due to the phase difference between the core mode and the cladding mode, and a slow varying envelope determined by the cross coupling strength. It is worth to mention that although the light wave coupled from the core mode to the cladding and the light wave remained in the cladding mode interfere with each, the interference fringe

formed by the cladding mode interference will be lost due to high loss in cladding mode propagation.

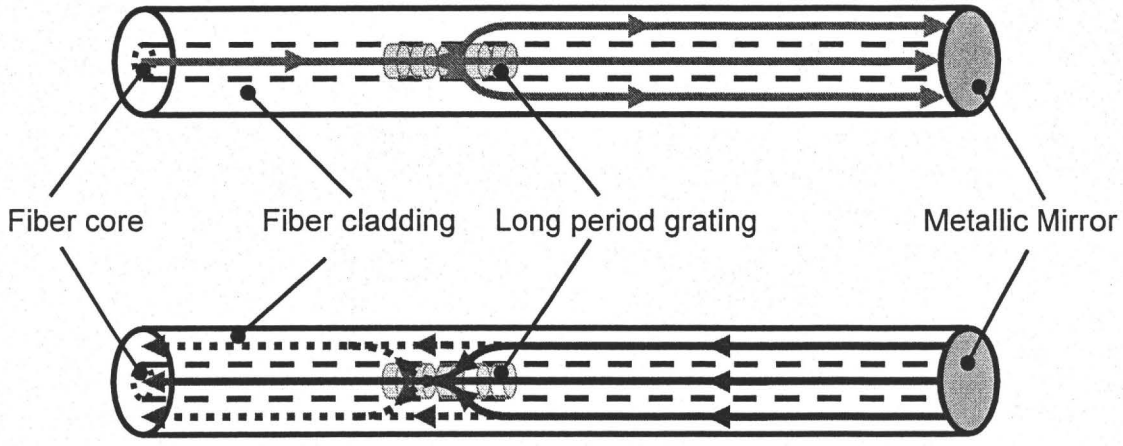

Figure 4.1 Schematic configuration and light wave path in a long period grating in-fiber Michelson interferometer.

4.2.2 Synthesis of the reflection spectrum of long period grating in-fiber interferometer with transfer matrix method

To simulate the behavior of long period grating in-fiber Michelson interferometers, we first synthesize the reflection spectrum of the interferometer. The light wave propagation in a long period grating in-fiber Michelson interferometer can be described by a typical non-uniform fiber grating model. Two methods exist for solving the two-mode resonance in non-uniform fiber grating [76]. The first method is the direct integration of the mode coupling equation (Eq.2.36 and Eq.2.37), which is simple and straight forward. However, from simulation point of view, this approach is not computational efficient. In the second method, the complex beam path in the fiber core and cladding is divided into piecewise uniform sections and solution of the core mode and cladding mode propagation in the device is calculated by multiplying the transfer matrix of each uniform grating section. As has been validated in Chapter 2, because of the large interval between neighboring resonance wavelength, the mode coupling between the core mode and the cladding modes in a long period grating can be simplified to two-mode resonance at the proximity of the resonance wavelength of the resonating cladding mode. Given the fact that the analytical solution of uniform long period grating exist for two-mode coupling, the transfer matrix is simple and computational efficient. For this reason, in the study, we chose the transfer matrix to synthesis the reflection spectrum of the long period grating in-fiber Michelson interferometer.

Following the notation in Chapter 2, the electric field of the core mode and cladding are A_{co} and A_{cl} respectively. The propagation of the light wave in each of the uniform piece of the interferometer can be expressed as:

$$\begin{pmatrix} A_{co}^{i} \\ A_{cl}^{i} \end{pmatrix} = F^{i} \begin{pmatrix} A_{co}^{i-1} \\ A_{cl}^{i-1} \end{pmatrix} \tag{4.1}$$

For the beam propagation in the interferometer (see Fig. 4.1), we divide the beam path in the interferometer into five sections: long period grating coupling, interferometer arm propagation, metallic mirror reflection, interferometer arm back propagation, and long period grating re-coupling. The output of the Michelson interferometer can thus be expressed as:

$$\begin{pmatrix} A_{co}^{ref} \\ A_{cl}^{ref} \end{pmatrix} = F_{LPG} F_{arm} F_{reflect} F_{arm} F_{LPG} \begin{pmatrix} A_{co}^{i-1} \\ A_{cl}^{i-1} \end{pmatrix} \tag{4.2}$$

Order the overall transfer matrix of the interferometer as:

$$F = F_{LPG} F_{arm} F_{reflect} F_{arm} F_{LPG} \tag{4.3}$$

Eq. 4.2 can be rewritten as:

$$\begin{pmatrix} A_{co}^{ref} \\ A_{cl}^{ref} \end{pmatrix} = F \begin{pmatrix} A_{cl}^{0} \\ A_{cl}^{0} \end{pmatrix} \tag{4.4}$$

The initial condition of the device is:

$$A_{co}^{0} = 1 \tag{4.5}$$

$$A_{cl}^{0} = 0 \tag{4.6}$$

The transfer matrix of each section of the optical path is given as follows:

For the uniform long period grating (from Eq. 2.43 and Eq. 2.44):

$$F_{LPG} = \begin{bmatrix} \cos(\gamma_c \Delta L) + i\frac{\hat{\sigma}}{\gamma_c}\sin(\gamma_c \Delta L) & i\frac{\kappa}{\gamma_c}\sin(\gamma_c \Delta L) \\ i\frac{\kappa}{\gamma_c}\sin(\gamma_c \Delta L) & \cos(\gamma_c \Delta L) - i\frac{\hat{\sigma}}{\gamma_c}\sin(\gamma_c \Delta L) \end{bmatrix} \tag{4.7}$$

Where ΔL is the length of the long period grating.

For the interferometer arm propagation:

$$F_{arm} = \begin{bmatrix} e^{i\beta_{co} D} & 0 \\ 0 & e^{(-\alpha_{cl} + i\beta_{cl})D} \end{bmatrix} \tag{4.8}$$

Where D is the length of the interferometer; $\beta_{co} = n_{eff,co} k_0$ is the propagation constant of the core mode, $\beta_{cl} = n_{eff,cl} k_0$ is the propagation of the cladding mode,

For the reflection at the metallic mirror:

$$F_{reflect} = \begin{bmatrix} \sqrt{R} & 0 \\ 0 & \sqrt{R}\Gamma_{cl} \end{bmatrix} \tag{4.9}$$

Where R is the reflectance of the metallic mirror and Γ_{cl} is the power confinement factor of the cladding mode in the fiber core and cladding and can be calculated by:

$$\Gamma_{cl} = \frac{\int_0^{r_{cl}} rdr\left(E_r H_\phi^* - H_r^* E_\phi\right)}{\int_0^{\infty} rdr\left(E_r H_\phi^* - H_r^* E_\phi\right)} \tag{4.10}$$

The reflection of the interferometer is:

$$R = \frac{\left|A_{co}^0\right|^2}{\left|A_{co}^{ref}\right|^2} \tag{4.11}$$

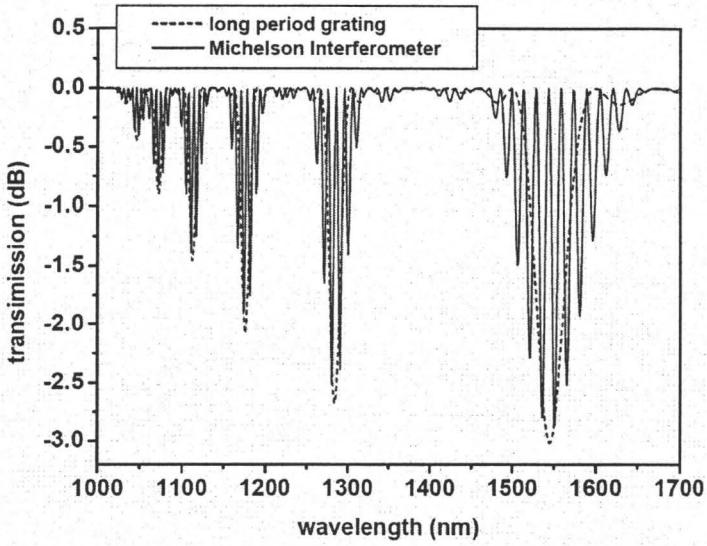

Figure 4.2 Reflectance spectrum of long period grating in-fiber Michelson interferometer simulated with transfer matrix method ($\Lambda = 300\mu m$, $L = 10mm$, $\Delta n_{DC} = 6\times10^{-5}$, $\Delta n_{AC} = 2.55\times10^{-4}$, $D = 25mm$, $R = 100\%$, $\alpha = 0$).

Figure 4.2 presents a reflection spectrum of a long period grating in-fiber Michelson interferometer simulated by the transfer matrix method. The fiber used in the simulation is a pristine Corning SMF28™fiber (whose parameter has been given in Chapter3); the grating period is set at $\Lambda = 300\mu m$ in order to set the resonance wavelength of the HE_{18} mode at $1550nm$. The amplitude of AC component of the refractive index modulation Δn_{AC} and grating length L are set at 2.55×10^{-4} and $10mm$ respectively to set the HE_{18} mode resonance notch ~3dB while keeping the notch width large. The transmission spectrum of the long period grating is plotted as the short dash line in Fig. 4.2. The cavity length of the Michelson interferometer is set at $D = 25mm$. In order to simplify the picture, we assume $R = 100\%$ and $\alpha = 0$, which is ideal situation for the interferometer. It is obvious that the interference fringe is presented in all the notch structure. The fringe visibility is a function of the notch depth. When the notch depth approaches $3dB$, the fringe visibility goes up. In the meantime, the fringe spacing change with the order of the cladding mode in resonance. The higher the order of the cladding mode, the larger the fringe spacing in the interference fringe is. The dependence of the

fringe spacing on the order of cladding mode reflects the dispersion of the cladding mode, which increases with the order of the cladding mode.

4.2.3 Dependence of the interference fringe to the ambient refractive index

The application of the long period grating in-fiber Michelson interferometer relies on dependence of the wavelength shift of the fringe on the ambient refractive index. The Wavelength shift of the fringe can be calculated by a phenomenological model based on calculating the relative phase between the core mode and the cladding mode.

In a long period grating in-fiber Michelson interferometer, the phase difference between the light waves propagates in the fiber core and the light wave re-coupled back to the core mode from the cladding propagation can be written as [77]:

$$\Psi = 2\Phi_{LPG}(\lambda, L) - 2\left[\beta_{co}(\lambda) - \beta_{cl}(\lambda)\right]D \tag{4.12}$$

Where Φ_{LPG} is the phase difference between the core mode and the cladding mode in the long period grating generated in the long period grating and, from Eq. 4.7, it can be expressed as:

$$\Phi_{LPG} = \arctan\left(\frac{\hat{\sigma}}{\gamma_c}\tan(\gamma_c L)\right) \tag{4.13}$$

The interference finger reaches maximum when the phase difference between the core mode and the cladding mode is integral times of 2π, i.e.:

$$\Phi_{LPG}(\lambda, L) - \left[\beta_{co}(\lambda) - \beta_{cl}(\lambda)\right]D = m\pi \tag{4.14}$$

The spacing of the fringe can be calculated using [78]:

$$S = \frac{\pi}{\frac{d\Phi_{LPG}}{d\lambda} - D\frac{d(\beta_{co} - \beta_{cl})}{d\lambda}} \tag{4.15}$$

It has been proved that when the cavity length of the interferometer is long enough ($D \gg L$), the phase difference generated in the long period grating is much less than the phase difference accumulated in the interferometer arm propagation and thus can be omitted in Eq. 4.12:

$$\Psi \cong -2\left[\beta_{co}(\lambda) - \beta_{cl}(\lambda)\right]D \tag{4.16}$$

In the same way, Eq. 4.15 can be rewritten as:

$$S \cong \frac{\pi}{D\frac{d(\beta_{co} - \beta_{cl})}{d\lambda}} \tag{4.17}$$

Since the propagation constant of the core mode is independent on the ambient refractive index, the wavelength shift of the interference fringe in the reflection spectrum due to the ambient refractive index change is given as:

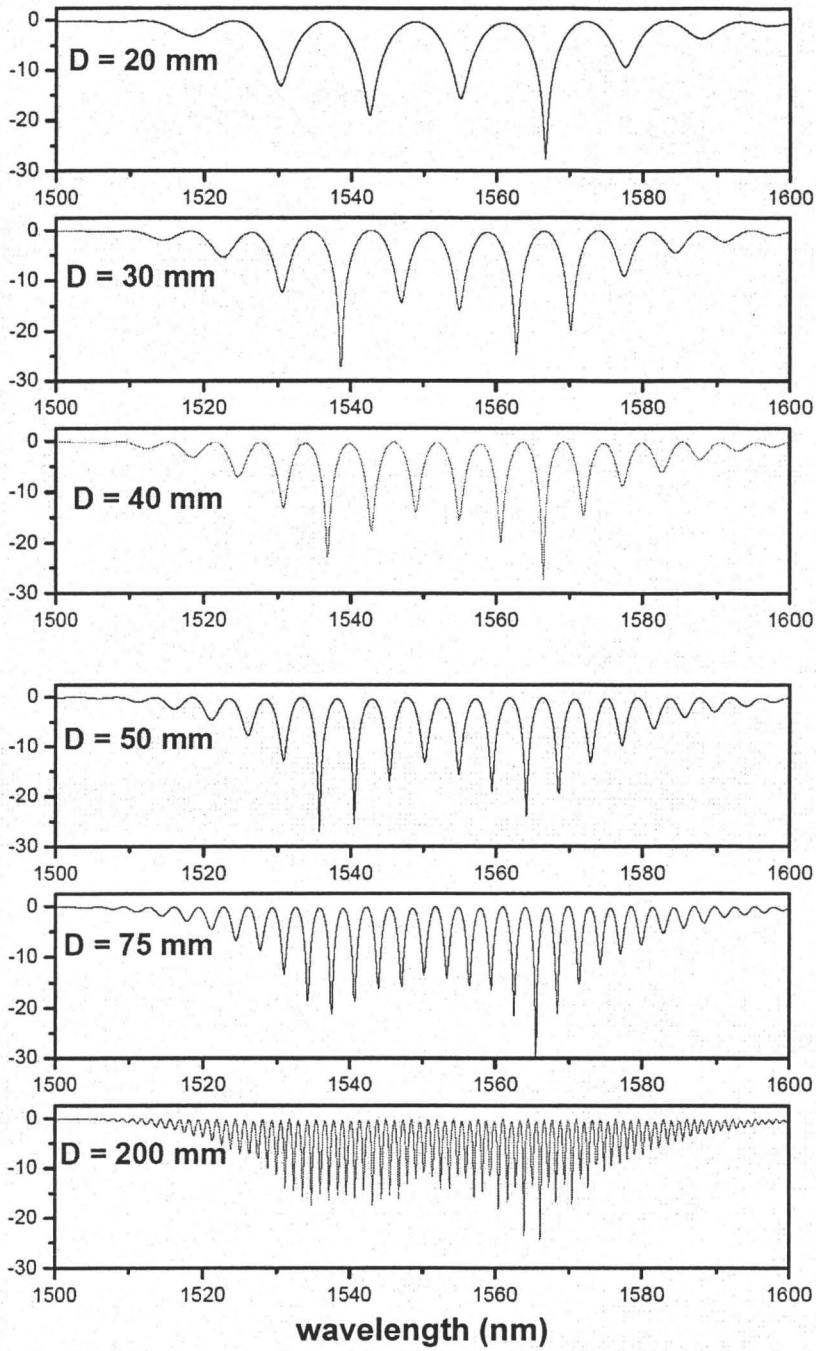

Figure 4.3 Reflectance fringe simulated with transfer matrix method for the HE_{18} cladding mode resonance notch in a long period grating in-fiber Michelson interferometer with different cavity length.

$$\Delta\lambda = \frac{\Delta\Psi}{2\pi}\cdot S = \frac{-\Delta\beta_{cl}}{\frac{d(\beta_{co}-\beta_{cl})}{d\lambda}} \tag{4.18}$$

Taking differential on both side of Eq. 4.18, the sensitivity of the interferometer fringe's shift towards shorter wavelength to the ambient refractive index change can be expressed as:

$$\frac{d\Delta\lambda}{dn_{amb}} = -\frac{1}{\frac{d(\beta_{co}-\beta_{cl})}{d\lambda}}\cdot\frac{d\beta_{cl}}{dn_{amb}} \tag{4.19}$$

Figure 4.3 shows the reflection fringes forming on the HE_{18} cladding mode resonance notch in the spectrum of a long period grating in-fiber Michelson interferometer synthesized with transfer matrix method. The parameters used in the simulation are: $\Lambda = 275\mu m$, $L = 10mm$, $\Delta n_{DC} = 1\times10^{-4}$, $\Delta n_{AC} = 1.5\times10^{-3}$, $R = 100\%$, $\alpha = 0$. The synthesized long period grating has a resonance notch of $3.6dB$ with center wavelength at $1551.21nm$. In order to study the dependence of the fringe spacing on the Michelson interferometer cavity length, we change the cavity length D from $20mm$ to $200mm$. It is very obvious that as the cavity length of the Michelson interferometer increases, the reflectance fringe becomes denser, i.e. the fringe space is proportional to the reverse of the cavity length of the interferometer.

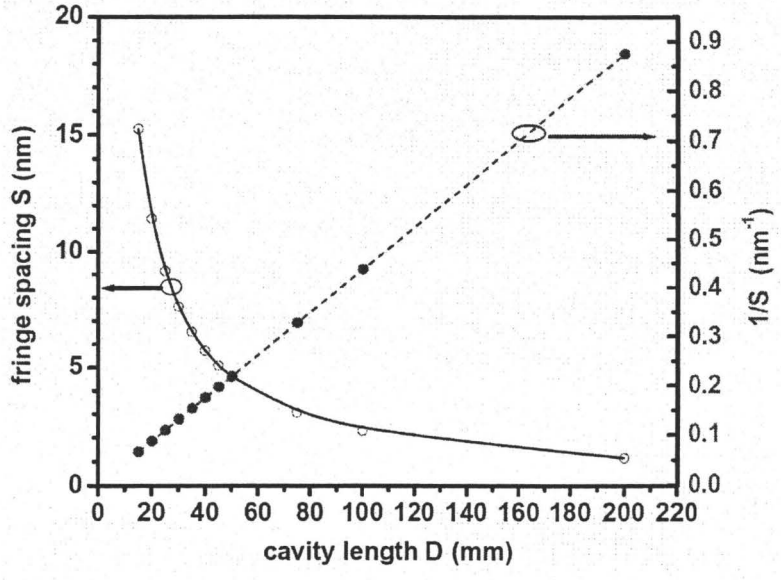

Figure 4.4 Fringe spacing S of the reflectance spectrum of a long period grating in-fiber Michelson interferometer and the reverse of the fringe spacing as a function of the cavity length D.

As a comparison to Eq. 4.17, Fig. 4.4 plotted the fringe spacing of the reflection spectra shown in Fig. 4.3 v.s. the cavity length as open dots. The fringe spacing

calculated from Eq. 4.17 (solid line) fits the result obtained with transfer matrix method well. The reverse of the fringe spacing ($1/S$) is proportional to the cavity length.

When the parameter of the long period grating and the cavity length are fixed, according to Eq. 4.18 and Eq. 4.19, the wavelength shift of the interference fringe is proportional to the change of the cladding mode propagation constant $\Delta\beta_{cl}$ and the reverse of the differential of the difference between the core mode propagation constant and the

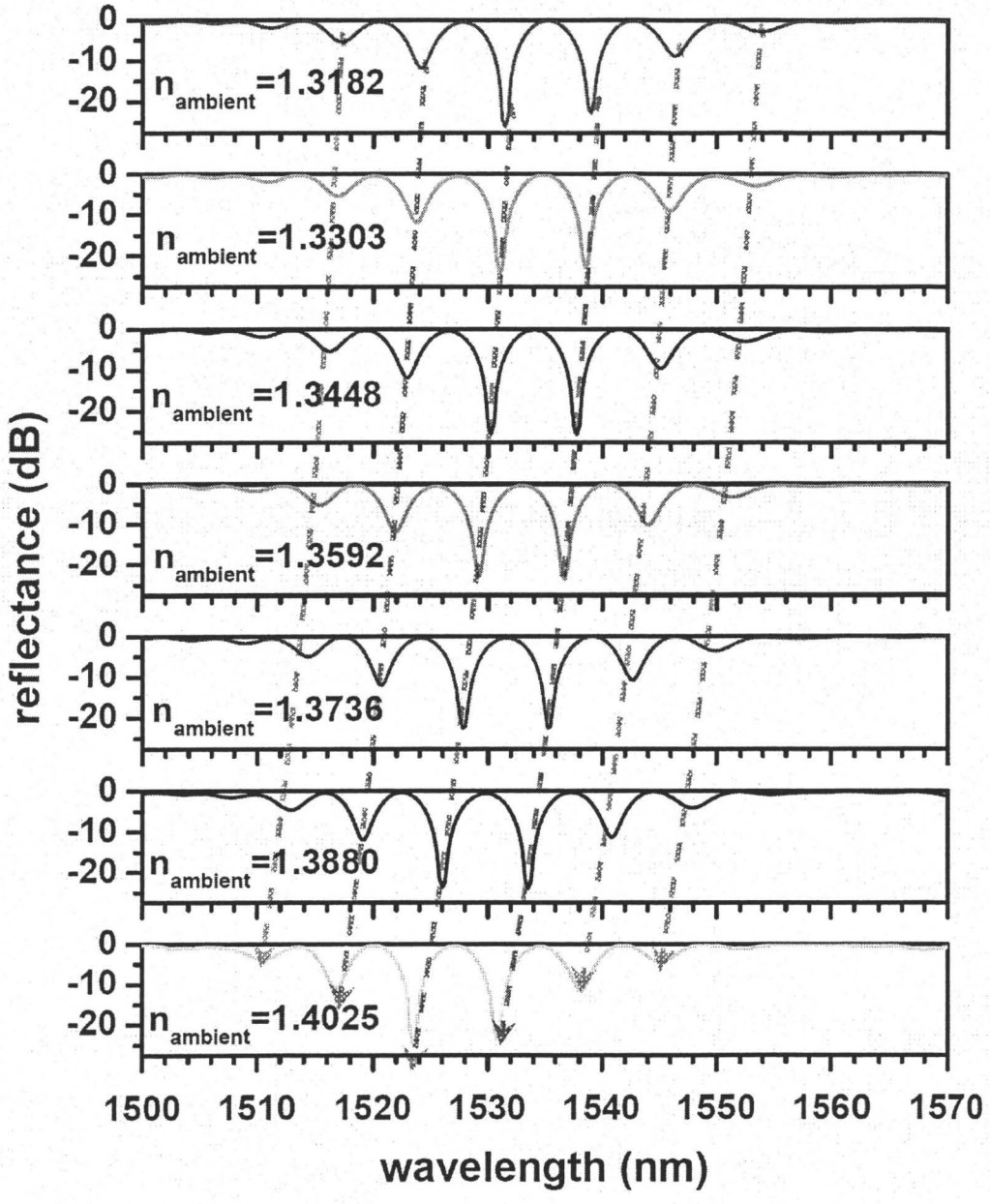

Figure 4.5 Evolution of reflection fringe of a long period grating in-fiber Michelson interferometer with different ambient refractive index with transfer matrix method.

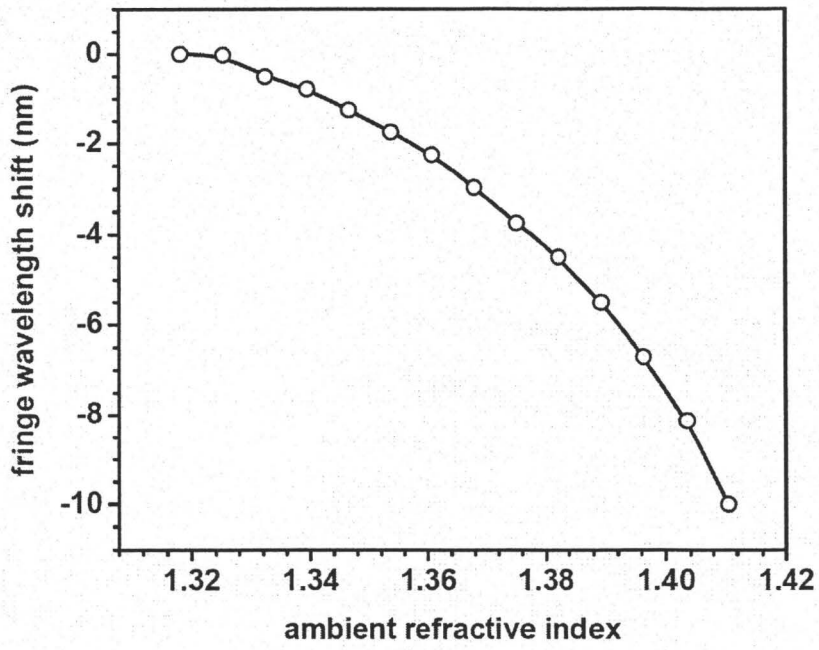

Figure 4.6 Wavelength shift of a long period grating in-fiber Michelson interferometer as a function of the ambient refractive index.

cladding mode propagation constant over wavelength $d\left(\beta_{co}-\beta_{cl}\right)/d\lambda$. Fig. 4.5 shows the evolution of the reflection interference fringe from a long period grating in-fiber Michelson interferometer simulated with transfer matrix method. The parameters used in the simulation were the same as those listed in the simulation presented in Fig. 4.3 except that the cavity length of the interferometer was fixed at $40mm$ and the refractive index of the ambient was varied from 1.3182 to 1.4025. From Fig. 4.5, one can find that as the refractive index of the ambient medium increases from low to high, the interference fringes shift to lower wavelength side. Plotting the fringe's shift towards shorter wavelength as a function of the ambient refractive index (see Fig. 4.6), as expected, the shift of the fringe wavelength is slow when the ambient refractive index is low and shift faster and faster as the ambient refractive index approaches the index of the cladding. The steepness of the $\Delta\lambda - n_{amb}$ reflects the proportional relation between the wavelength shift and the cladding mode propagation constant change related to the ambient refractive index.

So far, we have described the working principle of long period grating in-fiber Michelson interferometer and studied in theory the behavior of the reflection spectrum interference fringe and its dependence on the cavity parameter and the ambient refractive index change.

4.3 Experimental realization of long period grating in-fiber Michelson interferometer

4.3.1 General procedure for the long period grating in-fiber interferometer construction

The long period grating in-fiber Michelson interferometer studied above can be realized with various construction procedures. In this study, we adopt the method of forming the long period grating and the Michelson interferometer cavity mirror separately, followed by splicing the two pieces. In order to demonstrate enhancement of the sensitivity of the interferometer based refractive index sensor, the sensor cavity mirror section was etched to reduce the cladding layer radius. In this section, the detail of the construction of long period grating in-fiber Michelson interferometer will be given. First, section 4.3.1 will introduce fabrication of long period grating via side exposure of conventional optical fiber to UV laser beneath an amplitude mask. Section 4.3.2 describes the process to construct a long period grating in-fiber Michelson interferometer with and without reducing the cladding diameter of the cladding of the fiber cavity a bare fiber to form a taper on the diameter of the fiber cladding and to form a metallic reflector on the distal end of the fiber. At last, Section 4.3.3 shows the experimental characterization of the in-fiber interferometer device and discusses the result obtained.

4.3.2 Formation of long period grating with UV side exposure

A Corning™ SMF-28 fiber was hydrogen-loaded at room temperature for 672 h at 120 bar, to allow the hydrogen diffuse into the matrix of the fiber core material and enhance its photosensitivity to UV laser beam [79]. After the fiber was removed from the high pressure loading chamber, the fiber was then stored in deep freezer at $-30^{\circ}C$ to retard the out diffusing of the hydrogen molecule from the fiber before it was used to make fiber gratings within two weeks. During long period grating fabrication, the acrylic coating of the optical fiber is removed with a fiber jacket stripper to open a window for the UV side exposure. The fiber is then fixed on a fiber holder of a fiber grating inscribing setup for side exposure to UV radiation. Fig. 4.7 depicts the experimental apparatus for the formation of long period grating in an optical fiber with side exposure technique. The UV laser beam from an Excimer laser (GSI Lumonics IPEX 848, wavelength $248nm$, 130mJ/pulse , 20pulse/sec , beam dimensions $26mm \times 12mm$), is focused by a plano-convex cylindrical lens (CVI lasers, $f = 400mm$) into a focal line. At an amplitude mask made of copper, part of the laser beam is blocked by the amplitude mask and the remainder of the beam is radiated on the Ge doped core of the optical fiber behind the amplitude mask. Under intense UV radiation, a periodical refractive index modulation along the fiber axis is generated in the Ge doped fiber core, which is defined by the openings of the amplitude mask. The mechanism of the refractive index modulation in the fiber core by the UV radiation is based on the photorefractive effect of the Ge doped fused silica under intense UV radiation.

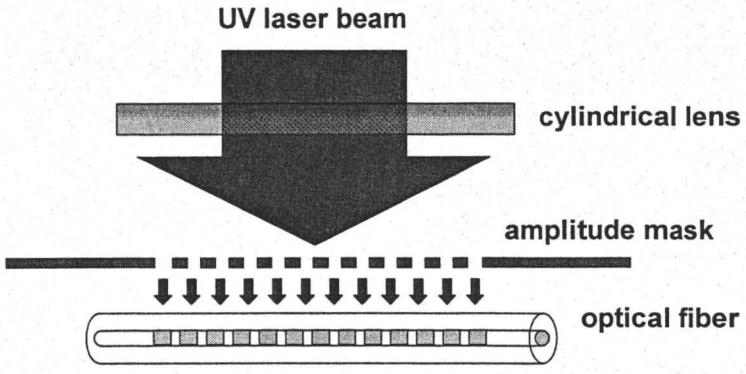

(a) Top View

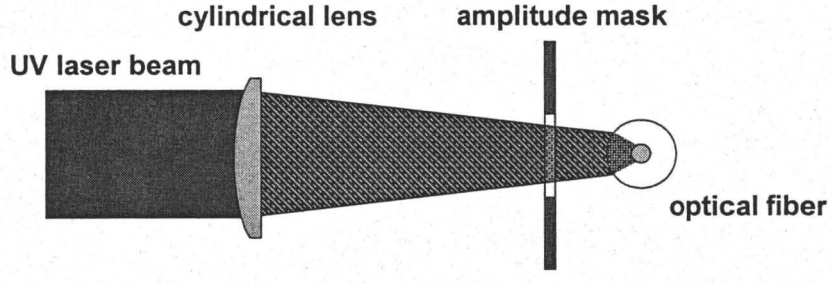

(b) Side view

Figure 4.7 Schematic of experimental apparatus for recording of long period grating in a optical fiber with side exposure to UV laser beam.

The photorefractive effect involved in the refractive index change is a multi-mechanism process, which involves both thermo-driven formation of germanium oxygen deficiency center and (Si)OH in the silica matrix of the fiber core with the existence of hydrogen. This process is followed by a UV quenching of the germanium oxygen deficiency center into deep UV absorbing center [79]. As a consequence, the fused silica in the fiber core has a high absorption peak in the deep UV range, which contributes to the refractive index change in the infrared wavelength according to the Kramer-Kronig relation.

The transmission spectrum of the long period grating was monitored in real-time with the measurement setup shown in Fig. 4.8. A halogen tungsten bulbs based white light sources was coupled to a $9/125\mu m$ fiber patch cord, the hydrogen loaded fiber was mounted on a fiber holder in the grating formation apparatus, and one end of the fiber under test was then connected with the fiber patch cords with a bare fiber adapter. The transmission output of the long period grating was send to an optical spectrum analyzer (ANDO AQ6317) to record the transmission spectrum. To make a precise measurement of the long period grating spectrum, ratio metric measurement was taken to eliminate the effect of the non-flatness on the output spectrum of the light source. To do so, the fiber grating to be tested was first by-passed with a patch cord (dashed line in Fig. 4.8) and the emission spectrum of the light source was measured and stored in the spectrum analyzer. When the long period grating under test was connected, the intensity spectrum obtained

by the optical spectrum analyzer was divided by the emission spectrum of the light source stored in the instrument to generate the transmission spectrum of the long period grating.

Since the long period grating was formed by side exposure of the hydrogen loaded fiber to intense UV laser radiation, it is expected that there would be a grating strength growing process. Fig. 4.9 recodes the evolution of the transmission spectrum in the process of a long period grating formation. The transmission spectrum is recorded at 60 second (Fig. 4.9a), 120 second (Fig. 4.9b) and 180 second (Fig. 4.9c) respectively. A synthesized transmission spectrum of the corresponding long period grating is plotted in the same graph (dotted line) as well. Prolonged UV radiation creates two effects in the

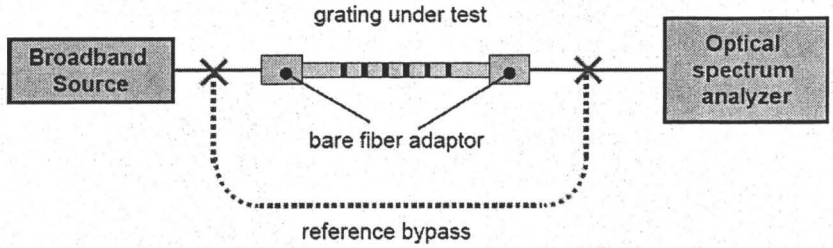

Figure 4.8 Schematic of the experimental setup for long period grating transmission spectrum measurement.

fiber core: First, the strength of the alternative component of the refractive index Δn_{AC} modulation increases, which is reflected in the growth of the notch depth. According to Eq. 2.50, the transmission of a long period grating is $T_{\min}^{11-1m} = 1-\sin^2 \kappa_{11-1m} L$, where $\kappa_{1m-11}^{cl-co}(z) = \frac{\omega \varepsilon_0 n_1^2 \sigma(z)}{2} \int_0^{2\pi} d\phi \int_0^{r_1} r dr \left(E_r^{v,cl} E_r^{co*} + E_\phi^{v,cl} E_\phi^{co*} \right)$, i.e.: $\kappa_{11-1m} \propto \Delta n_{AC}^2$. In Fig. 4.9a, Δn_{AC} is small ($\Delta n_{AC} = 8.5\times10^{-4}$ in simulation) so that $\kappa_{11-1m} L < \frac{\pi}{2}$ for all the cladding mode resonance, and the notch depth of all the cladding modes keep growing with Δn_{AC}. Given the fact that when the cladding mode order $m < 10$, the overlap integral between the core mode and the cladding mode (i.e. $\int_0^{2\pi} d\phi \int_0^{r_1} r dr \left(E_r^{v,cl} E_r^{co*} + E_\phi^{v,cl} E_\phi^{co*} \right)$ increases with the mode order, the notch depth of the cladding mode resonance increases with the mode order. As Δn_{AC} increases further (see Fig. 4.9b, where $\Delta n_{AC} = 1.26\times10^{-3}$ in simulation), the coupling strength of the HE_{17} and HE_{16} cladding mode resonance $\kappa_{11-1m} L > \frac{\pi}{2}$, thus the depth of HE_{17} and HE_{16} cladding mode resonance drops while the lower order cladding modes keep increasing. As Δn_{AC} increases further (where $\Delta n_{AC} = 1.62\times10^{-3}$ in simulation), as can be seen in Fig. 4.9c, the HE_{17} and HE_{16} cladding mode resonance notch depth keeps dropping with the HE_{15} cladding mode joining the notch depth dropping as well. However, the notch depth of the lower order cladding modes keeps growing with Δn_{AC}, since $\kappa_{11-1m} L$ is still less than $\pi/2$ for theses modes.

In the mean while, it is clear that the center wavelength of resonance wavelength of all the cladding modes keep shifting to the longer wavelength in the whole grating forming procedure. This is because that the averaged refractive index of the fiber core increases as a result of the refractive index modulation induced by the UV radiation. As a consequence, the effective index of the core mode increases and thus the cladding mode resonance wavelength has a red shift.

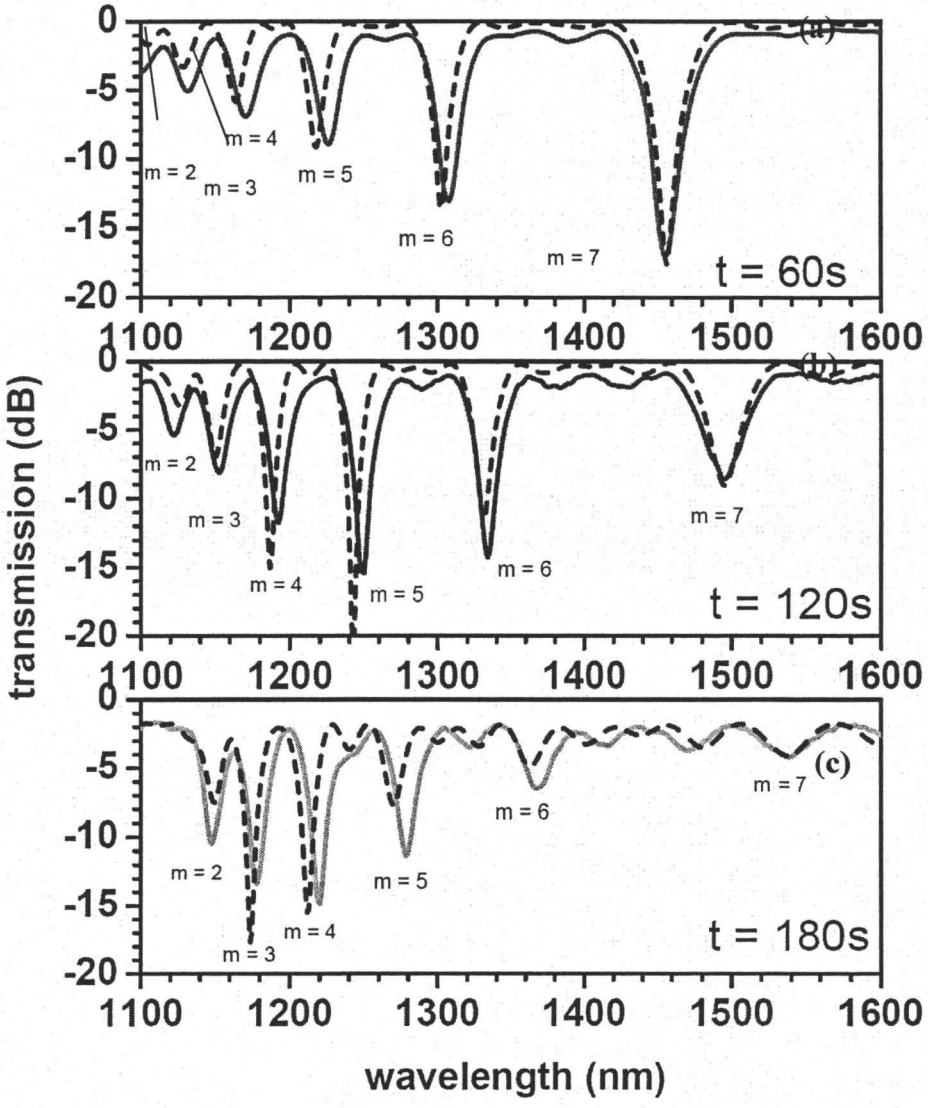

Figure 4.9 Evolution of the transmission spectrum of a long period grating in the process of grating formation

After the side exposure of the fiber under the UV laser radiation to form the long period grating, the grating was baked in an oven (Fisher Scientific, Isotemp 851F) at 110°C for 12 hours to remove the temporal refractive index change induced by the UV

radiation and stabilized the transmission spectrum of the long period grating. The high temperature baking also functions as a degassing process for the hydrogen molecule loaded in the fiber.

With careful control of the grating length as well as the UV exposure strength and time, the transmission spectrum of the long period grating in the C-band wavelength is trimmed to a wide notch with a depth of $3dB$, and thus ideal as a beam coupler for the in-fiber Michelson interferometer.

4.3.3 Formation of cladding tapered Michelson interferometer arms

In order to demonstrate the effect of the cladding reducing on enhancing the sensitivity of the cladding mode evanescent wave based refractive index sensor, two types of Michelson interferometer in-fiber arms are constructed. In the first type, a pristine fiber is used without modification of the cladding layer. In the second type of in-fiber arms the fiber cladding is reduced to small diameter to improve the sensitivity of the device to the ambient refractive index change. Because of the difference between these two in-fiber arms, different processing procedure is adopted to fabricate these two types of in-fiber arms.

The fiber arm without cladding reduction is relative simple, which involves only the formation of a high quality gold mirror at the distal end of an optical fiber. Fig. 4.10 schematically illustrates the processing steps. A piece of Corning™ SMF-28 fiber was first dipped in photoresist to form a layer of coating on top of the fiber surface. The coating film was then backed at 110°C to get the film hardened. The fiber tip was bring to a precision fiber cleaver (Fujikura CT-07BS High Precision Fiber Cleaver) and cleaved into a flat and perpendicular surface. The fiber tip was then inserted into a glass sleeve and loaded into an e-beam evaporation machine with the cleaved end facing the evaporation direction. A layer of Ti of $10nm$ was first deposited at the speed of $0.2nm/\text{sec}$ on the silica surface of the fiber as adhesion promotion layer. A layer of high quality Au film was then formed on top of the cleaved surface as high reflectivity film and the photoresist (300 *nm* at 1 *nm/sec*). Once the fiber was removed from the evaporation machine, the fiber tip was dipped in acetone to lift off the Au film deposited on the photoresist and thus leaves only the Au reflection film deposited on the distal end of the optical fiber.

Because of the small diameter of the cladding reduced fiber, the process to make cladding reduced in-fiber Michelson interferometer arms is more complex. First, Corning™ SMF-28 fiber was chemically etched in buffered hydrofluoric acid (BHF) or hydrofluoric acid (HF) solution to bring down the diameter of the fiber cladding. Chemical etching is a simple and stable fabrication technique, which is widely used in large scale at low cost. The process relies on the chemical interaction between HF/BHF and the pure silica, which can be expressed as:

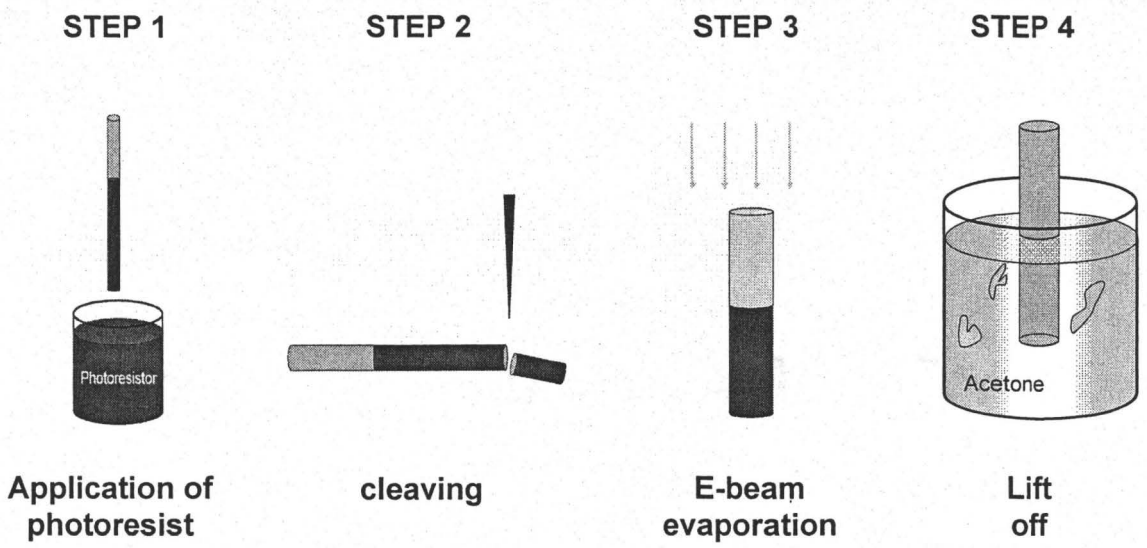

Figure 4.10 Schematic steps of the formation of gold mirror at the distal end of a fiber as the arms of an in-fiber Michelson interferometer.

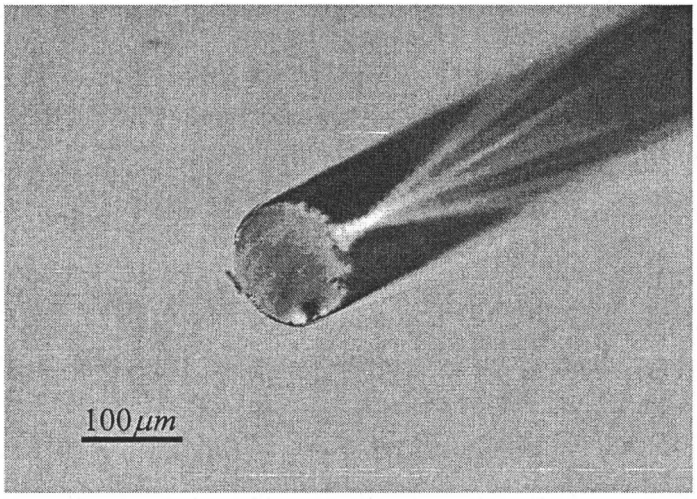

Figure 4.11 Microscope image of a high reflectivity metallic mirror formed on the tip of an optical fiber as the arms of in-fiber Michelson interferometer.

$$SiO_2 + 4HF \rightarrow SiF_4 + 2H_2O$$
$$SiO_2 + 4HF + 2NH_4F \rightarrow (NH_4)_2 SiF_6 + 2H_2O \quad (4.20)$$

The etching speed depends on the concentration of HF in the solution and the temperature of the solution. For consistency, all the experiments were carried on at a room temperature 22°C ± 1°C. Since the diameter of the fiber cladding could not be monitored in real time in the process. We first tested the etching speed of three etchant

solutions for the cladding reduction: 40% HF solution, 20% HF solution and saturated BHF solution. Changing of the HF concentration in the etchant solution was used to alter the etching speed while existence of saturated NH_4F buffer in the solution reduces the F^- concentration due to its reaction with silica and keeps the etching speed constant. The 40% HF solution, 20% HF solution was prepared by dilute concentrated HF (49%) with deionized water (DI Water) to the desire concentration. The BHF solution was prepared by dissolve 40g of NH_4F crystal in 60 *ml* of DI water followed by adding 60 *ml* of 49% HF solution.

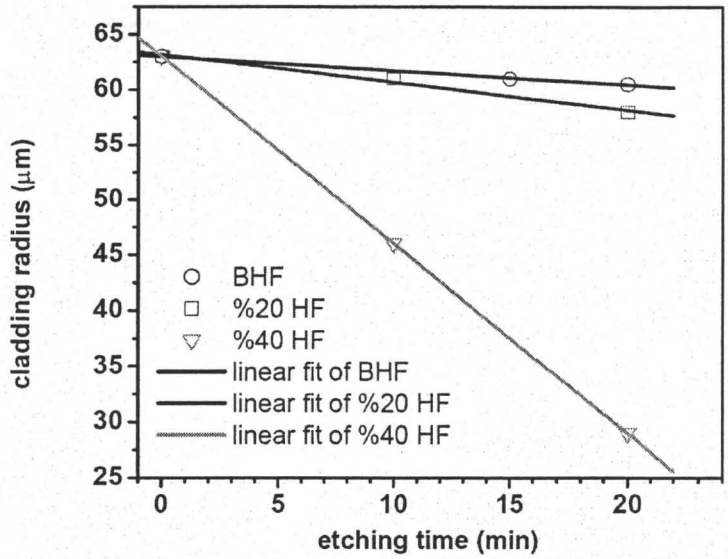

Figure 4.12 Calibration of the etching speed of the cladding layer of Corning™ SMF-28 fiber in different etchant solution.

Figure 4.12 shows the results of the etching rate. With linear fit of the experimental data, it is found that, at 22°C, the etching rate of fiber cladding in the etchant solution are: $1700nm/\text{min}$ for 40% HF solution, $250nm/\text{min}$ for 20% HF solution, and $127nm/\text{min}$ for BHF solution, respectively.

After the etching rate of the fiber cladding was calibrated, a fiber was etched in the etchant as the interferometer arm. In order to couple the light wave of cladding mode in the cladding unreduced fiber to the cladding reduced fiber and thus reserve the intensity of the cladding mode, it is necessary to form a taper on the fiber cladding between the cladding unreduced fiber and the cladding reduced fiber. The requirement of the taper is that: First it must be an adiabatic taper [80], which couples the cladding mode in the cladding unreduced fiber to the cladding mode of the same order in the cladding reduced fiber without coupling to the radiation mode or any other order of cladding modes. Second, the surface of the taper section must be smooth enough to reduce the propagation loss due to scattering at the interface between the cladding and the ambient medium. An experimental apparatus was designed to control the etching of the optical fiber in the etchant and form the taper required above. Fig. 4.13 shows a schematic diagram of the experimental setup. The optical fiber to be etched was mounted on a fiber holder fixed to a motorized linear stage. The linear stage was controlled by a computer

through a motion controller. The lower section of the fiber was immersed in the etchant in a polypropylene beaker and was gradually drawn out of the etchant solution under precise control of computer with a LabVIEW™ program. After the fiber was inserted into the etchant solution, a layer of mineral oil of 1 inch thick was carefully applied on top of the etchant. The mineral oil has two functions: First, it drives away the residue of the etchant on the surface of the fiber cladding and prevents forming a rough fiber cladding surface due to the residue etchant on top of the cladding. The mineral oil also isolates the etchant from the air flow in the fume hood in which the etching was carried out. It was found that strong air flow in the fume hood made the etchant evaporate very fast and leaves a salt crest at the interface. The capillary effect within the salt crest suck the etchant around the fiber in air at the proximity of the etchant-air interface makes the cladding surface coarse, and thus induces big loss in the cladding propagation and greatly weakens the mechanical strength of the fiber.

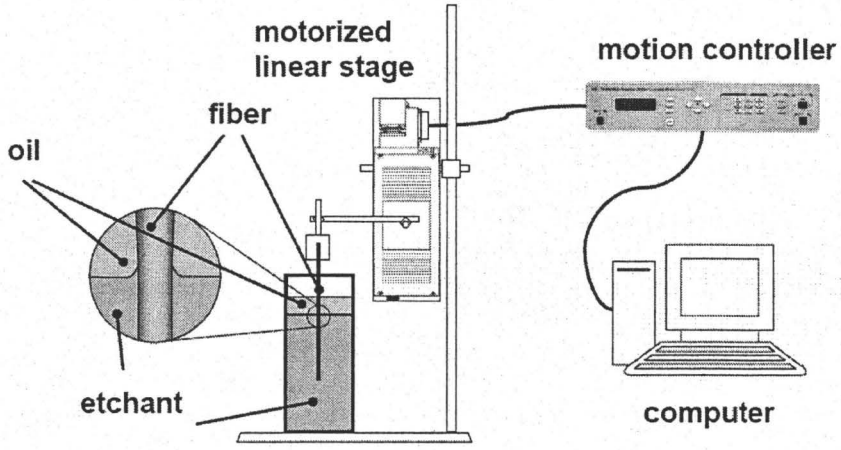

Figure 4.13 Schematic diagram of the experimental apparatus for cladding reduction and formation of high quality taper on the fiber cladding.

The most challenging step in making the cladding reduced fiber arms of the in-fiber Michelson interferometer lies in obtaining a high quality cleavage of the cladding reduced optical fiber and forming a high quality reflective metallic film on the distal end as the cavity mirror. When the fiber cladding diameter is reduced, the conventional fiber cleaver cannot hold the cladding reduced fiber to provide the tension for breaking the fiber. In addition, due to the reduced diameter of the fiber cladding, the photoresist used in conventional fiber process does not have the plasticity for the extension applied to the quartz fiber. As a consequence, the photoresist shatter into debris when tension is applied to the fiber. To overcome the problem above, numerous processing proceed was tried with the following procedure fixed as the best for the cladding reduced fiber arms preparation. The processing procedure of the fiber arms is schematically shown in Fig. 4.14.

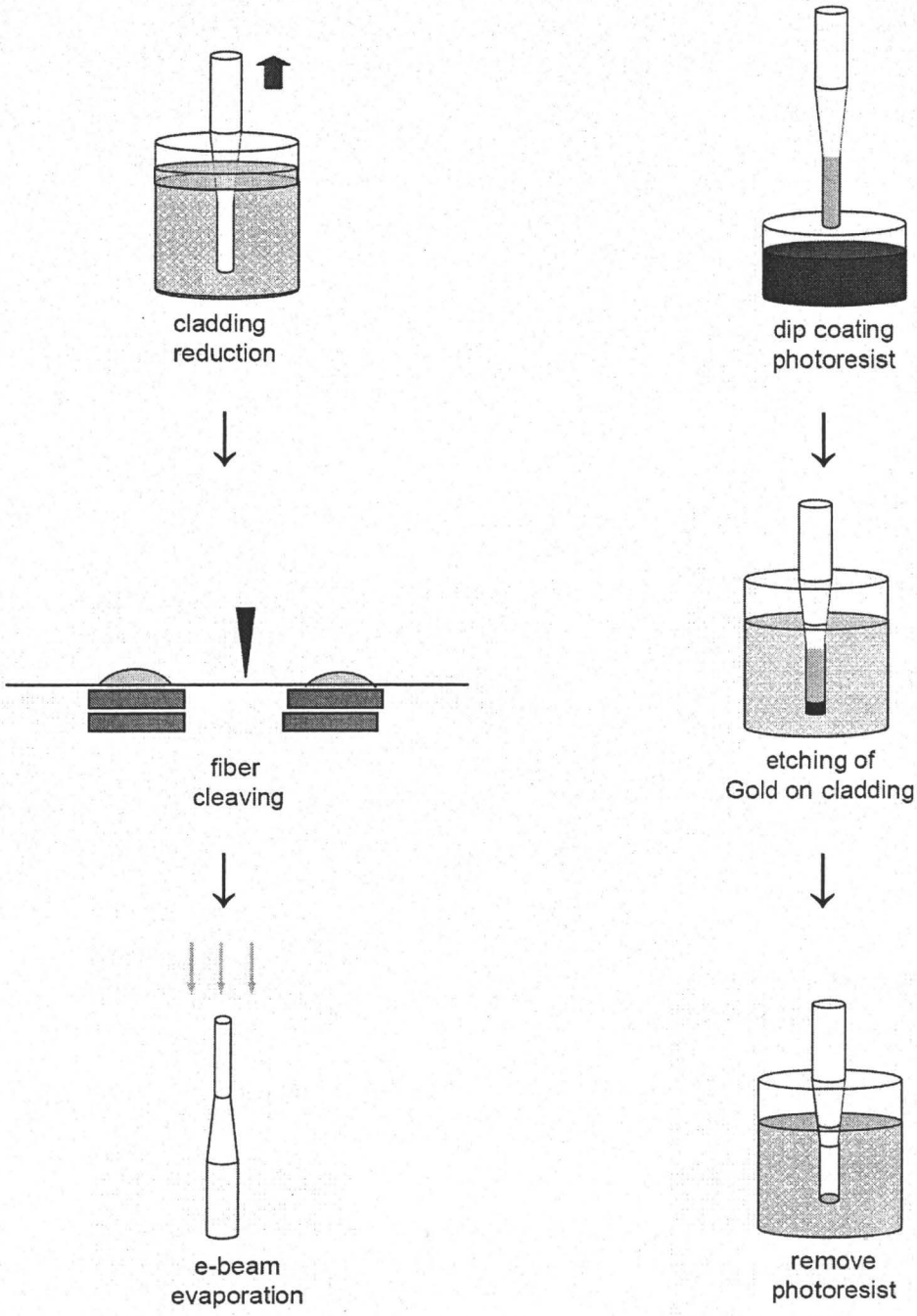

Figure 4.14 Schematic steps of fiber cladding reduction, taper formation and gold mirror coating at the distal end of a fiber as the arms of an in-fiber Michelson interferometer.

The cladding reduced fiber was first glued on a translation stage. Then the translation stages were moved to apply small tension on the fiber. After that, a special home-made fiber cleaver consists of a tungsten carbide blade and a piezoelectric actuator

was used to cleave the fiber. The tungsten carbide blade was attached on the tip of the piezoelectric actuator. When the piezoelectric actuator is driven by a high frequency driving voltage, the carbon nitride oscillates with the piezoelectric actuator at high frequency. When the carbon nitride blade moved in touch with the optical fiber, the high acceleration associated with the ultrasonic motion of the blade posed strong mechanical impact on the fiber and created a microscopic fracture on the fiber cladding. Under the tension applied, the fracture developed through the whole cross section of the optical fiber and a high quality flat surface perpendicular to the fiber axis was formed. The cleaved fiber was then inserted into a jig with the distal end face upward. After the e-beam evaporation step high reflectivity metallic film was formed on the whole tip of the optical fiber. After the e-beam evaporation, the tip of the fiber was dipped into photoresist. The dipping was extremely carefully controlled to allow only a very short ($< 200 \mu m$) of the fiber tip been coated with photoresist. After baking of the photoresist coated fiber and the photoresist hardened, the fiber tip was immersed into gold etchant to remove the unwanted gold film deposited on top of the cladding layer. At last, the fiber tip was soaked in acetone to remove the protective photoresist layer.

Figure 4.15 and Figure. 4.16 are pictures of a cladding reduced fiber with the cladding taper under a microscope (Keyence, Canada VHX-600) focused at the metallic mirror at the distal end of the fiber, and sideview of the tip respectively. Fig. 4.17 shows the side view of the whole cladding reduced fiber taken by the microscope mentioned

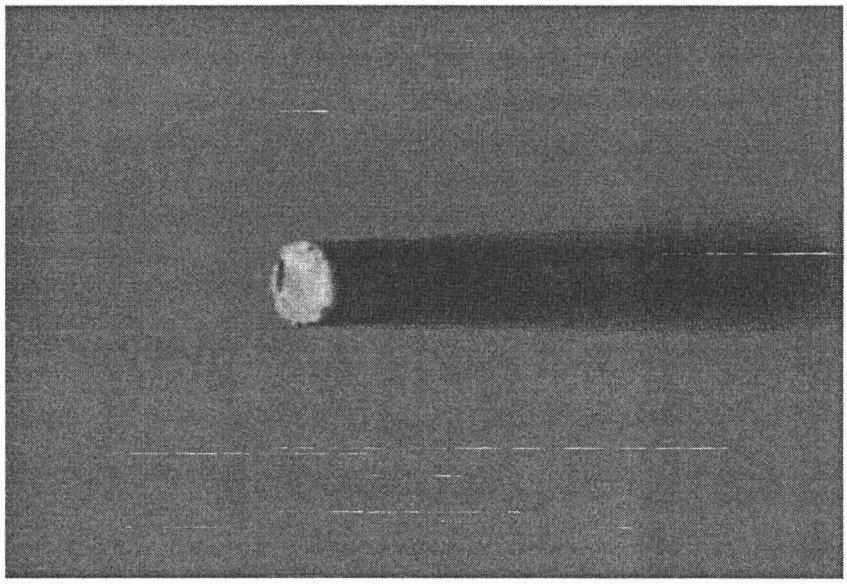

Figure 4.15 Picture of the metallic reflective mirror formed on the distal end of cladding reduced fiber.

above. In order to show the cladding reduction and the taper clearly, the pictures of the sideview were compressed by 38 fold in the horizontal direction and stitched together. The fiber cladding radius profile as a function of the axial position along the optical fiber was measured with a Nikon Eclipse E200, which was equipped with a reticule. The test results are presented in Fig. 4.18. As can be seen from Fig. 4.17 and Fig. 4.18, the fiber

arms formed in this process has a total length of 40 *mm*, which consist of 10 *mm* of unreduced fiber, 16 *mm* of taper section and 14 *mm* of cladding reduced fiber with uniform cladding diameter. The cladding unreduced section was on purposely reserved

for future splicing with a long period grating. The16*mm* long taper section formed by gradually drawing the fiber out of the etchant solution, was found to be strictly linear and the taper angle was small enough to guarantee that the mode coupling between the unreduced fiber section and the cladding reduced fiber section is adiabatic so that the mode order can be reserved in the transition.

At last the cladding reduced fiber arms was spliced with the long period grating to form a long period grating based in-fiber Michelson interferometer.

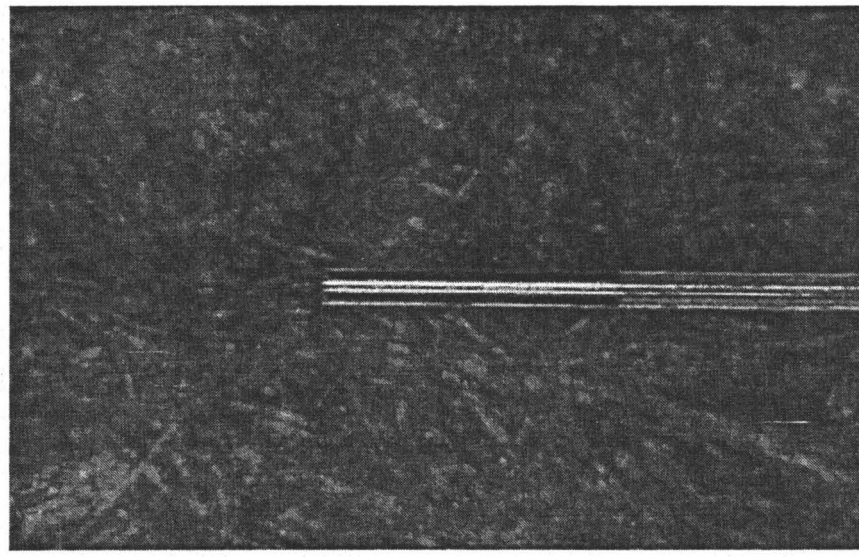

Figure 4.16 Side view of the gold coated fiber tip of the in-fiber Michelson interferometer arms.

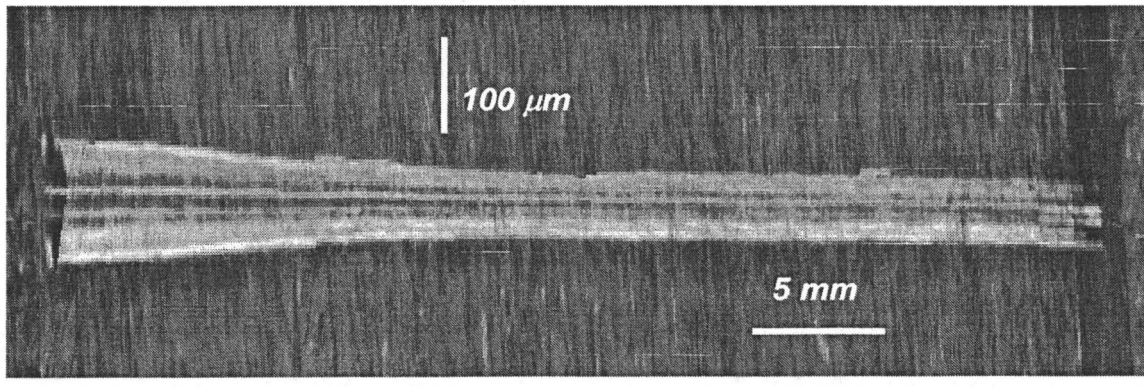

Figure 4.17 Side view of the cladding reduced fiber with a taper on the fiber cladding.

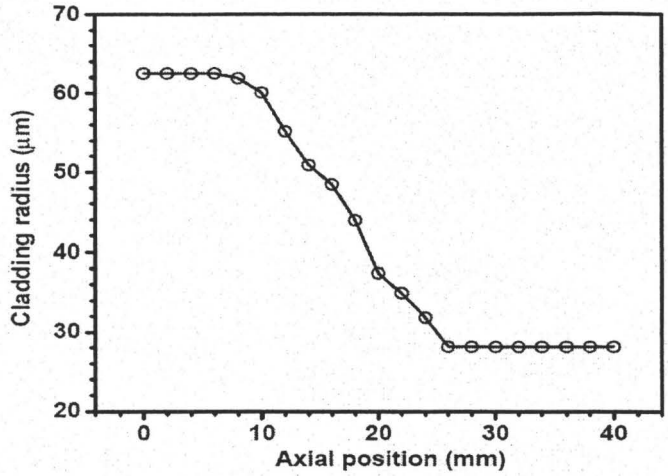

Figure 4.18 Cladding radius as a function of the axial position on a cladding reduced fiber.

4.4 Experimental test of the long period grating in-fiber Michelson interferometer

4.4.1 Experimental setup

Experimental characterization of the long period grating in-fiber Michelson interferometer depends on measuring the reflectance spectrum of the interferometer. Fig. 4.19 shows the schematic diagram of a reflectance spectrum interrogation setup. Lightwave from an amplified spontaneous emission broadband source (BBS, JDS Uniphase, BBS1550+2FA00) with an output spectrum covering $1527-1568nm$ wavelength range is injected into a long period grating in-fiber Michelson interferometer through a fiber optic circulator. When the light reflected back from the in-fiber Michelson interferometer hits the optical circulator, the reflection is redirected to the optical spectrum analyzer (OSA, Ando AQ6317). In order to eliminate the spectral non-uniformity of the BBS output, the output spectrum of the BBS is measured and stored in the OSA first, subsequent measurement of the reflected light from the long period grating in-fiber interferometer is divided by the output spectrum of BBS to obtain the reflection spectrum of the interferometer.

Fig. 4.20 shows a typical reflection spectrum measured from a long period grating in-fiber Michelson interferometer. The grating length was 25 mm. and the LPG transmission spectrum has a notch structure with its center wavelength at 1527 nm and has a notch depth of 3.2 dB. The interferometer has a cavity length of $50mm$ and the diameter of the cladding reduced fiber is $55\mu m$. It can be seen from Fig. 4.20 that the reflection fringes have a fringe spacing of 3.58 nm and a fringe contrast of 6.0dB.

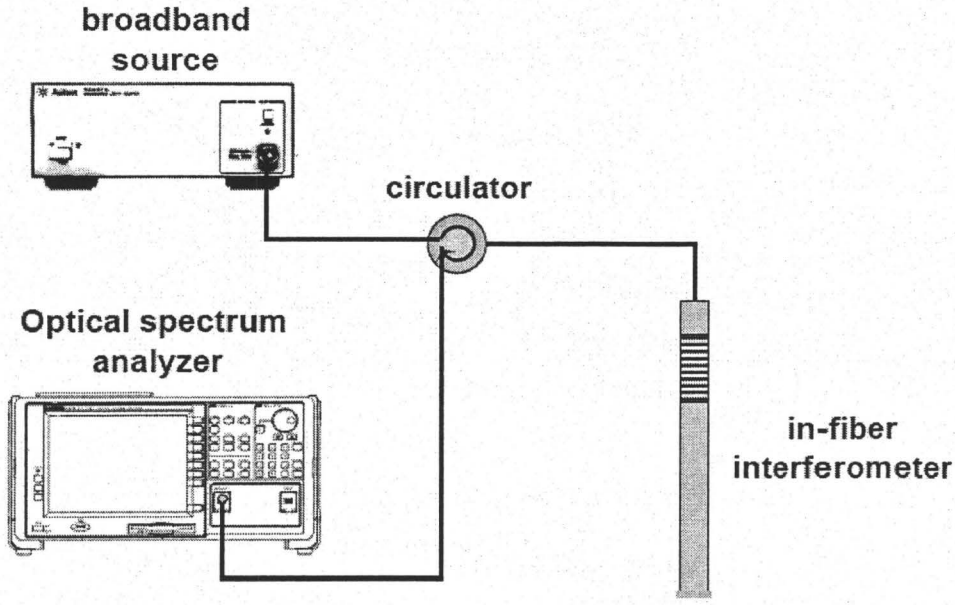

Figure 4.19 Schematic of the experimental setup for the long period grating in-fiber Michelson interferometer interrogation.

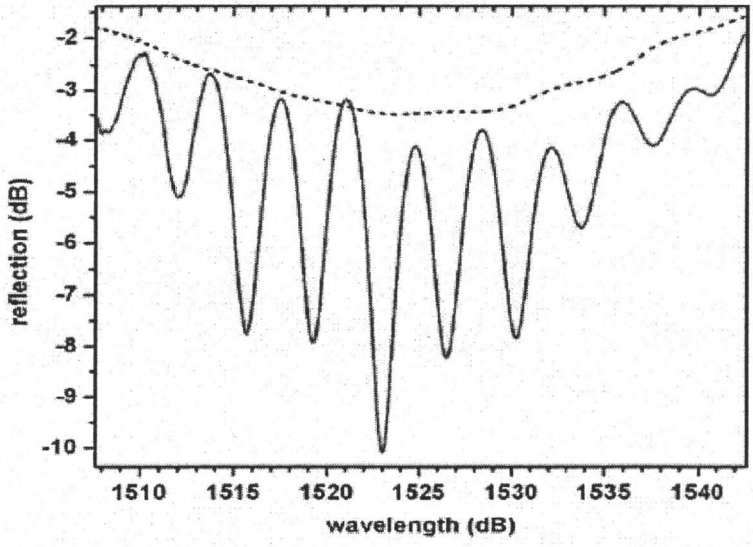

Figure 4.20 Reflection spectrum of the cladding tapered fiber Michelson interferometer in air, the transmission spectrum of the LPG used as the beam splitter in the interferometer is plotted as the reference in dotted line.

As illustrated in Fig. 4.21, an experimental setup was constructed to allow precise control of the dipping of the long period grating in-fiber Michelson interferometer into the analyte with high stability and high precision. The in-fiber interferometer was mounted on a fiber holder attached to a motorized linear translation stage so that it can vertically move in and out of the measuring cylinder containing the glycerin solution. By setting the travel position of the translation stage, the length of the interferometer arm immersed in the glycerin solution can be set at different values.

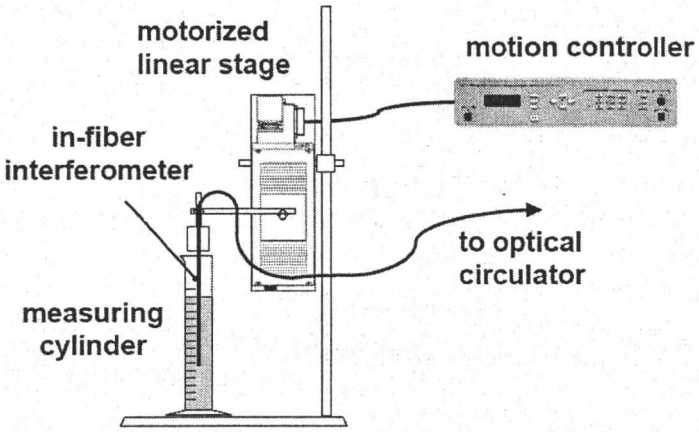

Figure 4.21 Experimental setup for measuring the response of long period grating in-fiber Michelson interferometer to the ambient refractive index and liquid level of immersion.

4.4.2 Dependence of the fringe shift vs. the immersion depth

We first studied the dependence of the wavelength of the reflection interference fringe on the immersion depth of the interferometer arms in the solution tested. An in-fiber Michelson interferometer with its long period grating center wave length located at $1525nm$ and interferometer cavity length $L = 50mm$ was mounted on a motorized linear translation set at the highest position. In order to eliminate the influence of the ambient refractive index on the transmission spectrum and thus the beam splitting and phase retardation in the long period grating, a protective silver film was formed on top of the long period with silver mirror reaction to shield the ambient solution away from the cladding layer of the long period grating. A measuring cylinder filled with deionized water to an appropriate level was placed below the fiber interferometer. Under the control of the motion controller, the fiber arms of the in-fiber interferometer moved down towards the water surface with the motorized linear translation stage. Right before the tip of the interferometer touched the water surface, a reflectance spectrum was recorder. After that, the fiber was transport down at an increment of $5mm/step$. Each time the interferometer was displaced, the reflectance spectrum was recorded till the water surface reaches the long period grating. Data processing was then carried out by tracking the

wavelength shift of an interference fringe in the reflectance spectrum, which is presented in Fig. 4.22. As the immersion length of the in-fiber Michelson interferometer arms increases, the wavelength of the interference fringes move towards shorter wavelength till the water level reaches the long period grating. Linear fit of the wavelength shift vs. immersion depth shows that as long as the water level is below the location of the long period grating, the fringe's shift towards shorter wavelength is linear to the immersion depth of the fiber arms in the water.

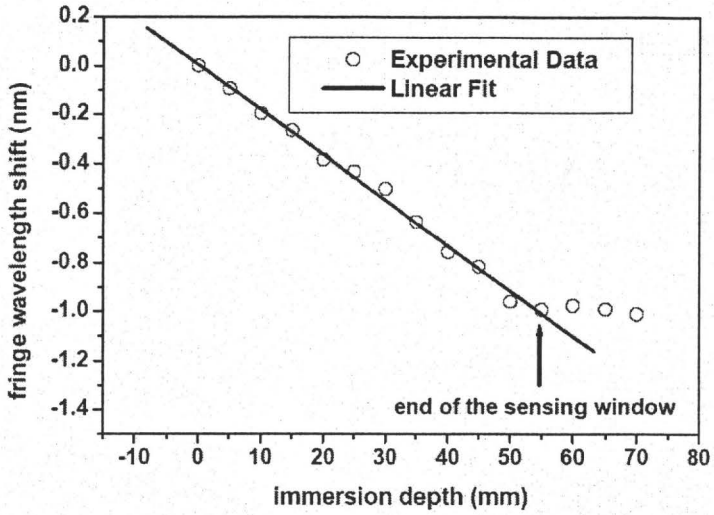

Figure 4.22 Dependence of the fringe's shift towards shorter wavelength as a function of the immersion depth of the fiber arms of the in-fiber interferometer in water.

Because of the existence of the immersion depth dependence of the fiber arms in the analyte solution, it is necessary to eliminate the cross interference of the immersion depth on the fringe's shift towards shorter wavelength. There are two ways to solve this problem: As has been described above, the first method is to define a determined length of fiber exposure to the ambient solution with a shielding metallic film. This configuration isolates the long period grating from the ambient and thus avoids phase shift induced in the long period grating, which is different from the phase shift induced in the cladding mode propagation. However, two problems associate with this configuration: 1. because the eigen cladding mode of the metal film coated fiber is different from the eigen cladding mode in the solution, high loss of the cladding mode exists at the edge of the metallic film due to the mode mismatch between the two sections. As a consequence the reflection spectrum has high loss and low visibility; 2. The silver film is chemically incompatible with the chemical protocol of the bio-recognition film immobilization. In the second configuration, the whole interferometer including the long period grating is immersed in the analyte solution and the reflectance spectrum is recorded. This configuration is simple and straight forward but the long period grating itself is exposed to the ambient solution. As a result, the transmission notch wavelength and the phase delay induced in the long period grating are modulated by the ambient solution, which increases the complexity of the signal processing. Nevertheless, in biosensing applications, the change of the refractive index and/or thickness of the bio-recognition

film in the assay are small, and thus the wavelength shift of the transmission notch wavelength and the phase delay induced in the long period grating is negligible. In the rest of this chapter, our study on the response of the long period grating in-fiber Michelson interferometer will adopt the first configuration. The second configuration will be discussed in Chapter 5, where biosensing application will be studied.

4.4.3 Interference fringe's shift towards shorter wavelength induced by the ambient refractive index change

To study the sensitivity of the cladding reduced fiber Michelson interferometer on ambient refractive index, the in-fiber Michelson long period grating interferometer was immersed in a mixture of pure water and glycerin. By changing the ratio of the glycerin in pure water from 0% v/v to 100% v/v, the refractive index of the solution can be adjusted. Taking into account of the dispersion of the glycerin and water, the refractive index of the aqueous solution of glycerin at different wavelength from 1000 *nm* to 1700 *nm* with concentration from 0% to 100% at a step of 10% is given in Table 4.1.

The long period grating in-fiber Michelson interferometer was dipped into the glycerin-water solution and the reflection spectrum was scanned 5 times with the OSA. After each measurement, the interferometer was rinsed in anhydrous ethanol twice and then dried in air for the next measurement. Fig. 4.23 shows the evolution of the interference fringe obtained from the long period grating in-fiber Michelson interferometer with a reduced cladding diameter $d = 55\mu m$ against the ambient solution refractive index change. In order to obtain a clear picture of the fringe's shift towards shorter wavelength, the reflectance spectrum obtained in solutions with different concentrations was vertically shifted to allow the detail of the entire interference fringe visible. As can be seen from Fig. 4.23, when the ambient refractive index increases, all the fringes shift towards shorter wavelengths (i.e. blue shift), representing a phase difference shift between the core mode and the cladding as a function of the ambient refractive index. In addition, the visibility of the fringe drops off. When the solution refractive index is close to the refractive index of the cladding layer, the interference fringe diminishes because as the cladding mode is approaching the cutoff value, the cladding mode is strongly attenuated by the ambient medium and infringes the insensitivity equality condition required for high contrast interference between the core mode and the cladding mode.

By tracing the wavelength shift of the interference fringe, we were able to study the dependence of the fringe's shift towards shorter wavelength on the change of the solution refractive index with different cladding radius. It is worth noting that due to the cladding reduction, the cladding mode dispersion is a function of the cladding diameter. According to Eq. 4.17 and Eq. 4.18, when the arm length of an interferometer is fixed, the change in the dispersion will change the interference fringe spacing and subsequently the wavelength shift of the fringe. To solve this problem, the wavelength shift of the fringes obtained with in-fiber Michelson interferometers of different cladding diameter was converted to phase shift of the fringes with:

Table 4.1 Refractive index of aqueous solution of glycerin at different wavelength with different concentration

Wavelength (nm) / Concentration (%)	1000	1100	1200	1300	1400	1500	1600	1700
0	1.32674	1.32547	1.32411	1.32264	1.32100	1.31916	1.31708	1.31470
10	1.34042	1.33919	1.33790	1.33651	1.33499	1.33330	1.33140	1.32923
20	1.35411	1.35291	1.35168	1.35039	1.34898	1.34744	1.34571	1.34376
30	1.36779	1.36663	1.36546	1.36426	1.36298	1.36158	1.36003	1.35829
40	1.38148	1.38035	1.37925	1.37813	1.37697	1.37572	1.37435	1.37282
50	1.39516	1.39407	1.39303	1.39201	1.39096	1.38986	1.38866	1.38735
60	1.40885	1.40779	1.40681	1.40588	1.40496	1.40400	1.40298	1.40188
70	1.42253	1.42151	1.42060	1.41976	1.41895	1.41814	1.41730	1.41641
80	1.43622	1.43523	1.43438	1.43363	1.43294	1.43228	1.43162	1.43094
90	1.44990	1.44895	1.44817	1.44751	1.44693	1.44642	1.44593	1.44547
100	1.46359	1.46267	1.46195	1.46138	1.46093	1.46056	1.46025	1.46000

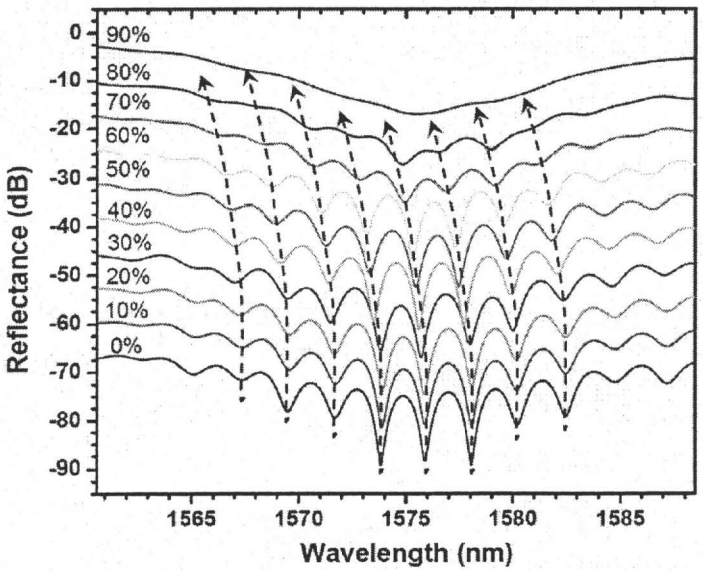

Figure 4.23 Evolution of the reflection fringe of the cladding tapered Michelson interferometer against the concentration of glycerin in water.

$$\Delta\Psi = \frac{2\pi\Delta\lambda}{S} \tag{4.21}$$

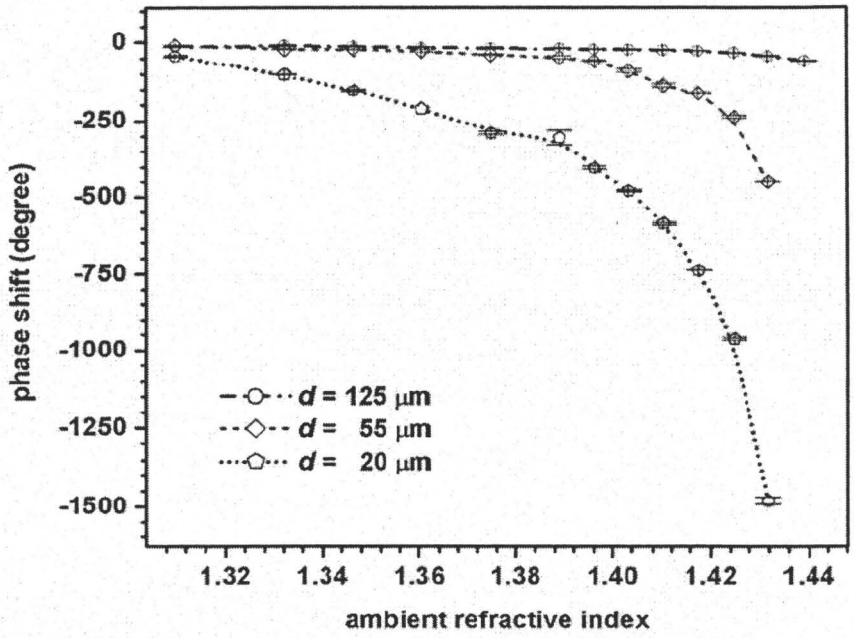

Figure 4.24 Experimental phase shift of an in-fiber LPG Michelson interferometer with different cladding diameter as a function of the ambient refractive index.

In Fig. 4.24, the phase shift values of the cladding reduced fiber Michelson interferometer with a cladding diameter of 55 μm and 20 μm are plotted as diamond and pentagon, respectively. As a comparison, response of a long period grating in-fiber Michelson interferometer without cladding reduction is shown in the same figure (circle). As expected, the phase shift of the fiber Michelson interferometer with cladding reduction is significantly enhanced as compared to the conventional long period grating in-fiber Michelson interferometer without the cladding reduction. The thinner the cladding layer, the larger the wavelength shift is for the same solution refractive index change. However, the cladding diameter cannot be reduced without restriction. When the cladding diameter is below 20 μm, the cladding mode reaches its cutoff condition at lower solution refractive index values and thus reduces the measuring range of the refractive index sensor. Nevertheless, for the cladding diameter of the fiber being reduced to $20\mu m$ in this paper, a fringe phase shift vs. solution refractive index sensitivity (defined as phase shift divided by the solution refractive index change) of 73138°/RI is demonstrated. Comparing to the sensitivity of conventional in-fiber LPG Michelson interferometer (1822°/RI) without cladding reduction, this represents a sensitivity enhancement of 40 fold. Check theoretical simulation result presented in Section 3.1, when the radius of a fiber cladding is reduced from 62.5 μm to 20 μm, the dependence of the HE_{17} mode on the ambient refractive index is boosted by 44.6 fold. The experimental result matches well with the experimental simulation well. To calculate the ambient refractive index resolution of this sensing scheme, the phase stability of the interferometer (error bar in Fig. 4.24) is divided by the phase sensitivity of the device. It

is found that the ARI resolution of the interferometer with a 20 μm cladding diameter is $7.7\times10^{-5}RI$. It is worth noting that, in this experimental study, an OSA with a resolution of 16 pm is used as an interrogation instrument. If an interrogation instrument with higher wavelength resolution is used, higher ARI resolution can be achieved.

In summary, the fundamental and performance of long period grating assisted in-fiber Michelson interferometer has been investigated in this chapter. Numerical study of the interferometer characteristics has reveled that interference between the core mode and cladding mode within the cladding mode resonance band produces an interference fringe in the reflectance spectrum. The spacing of the interference fringe is a dependent of the core mode and cladding mode dispersion as well as the interferometer arm length. With careful engineering, long period grating in-fiber Michelson interferometer was constructed. By adopting the cladding reduction method proposed in Chapter 3, the sensitivity of the interference fringe phase shift vs. the solution refractive index change was enhanced by 40 folds as compared to the conventional cladding unreduced interferometer.

Chapter 5

Long Period Grating Based Fiber Optic Biosensor

5.1 Introduction

As has been described in Chapter 1, a successful construction of optical biosensors relies on four parts: the bio-recognition mechanism, the physico-chemical transducer, the interrogation system and data processing, and the bio-recognition film immobilization technique. Thanks to the development of biotechnology, the bio-recognition mechanism has been well developed, which has been briefly reviewed in Chapter 1. A class of fiber optic evanescent wave sensing device built on long period grating based photonic device has been studied in Chapter 3 and Chapter 4 of this thesis. With the target of constructing a biosensing device, in this chapter, we investigate the immobilization of the bio-recognition material on top of the fiber cladding and test the performance of the biosensor. The studies on the interrogation system and data processing have gone beyond the sensing device and thus will be reserved for future investigation.

The text of this chapter is organized in the following way: In Section 5.2, different strategy of biomolecule immobilization on the fiber cladding surface is described. Section 5.3 presents immobilization of a single strand deoxynucleic acid (ssDNA) on the surface of a conventional long period grating and its hybridization with its complementary deoxynucleic acid (cDNA). A fiber optic immunosensor based on long period grating in-fiber Michelson interferometer is described in Section 5.4, in which goat anti-human Immunoglobulin G (IgG) as an antibody is immobilized on top of the cladding layer of the fiber cavity of an in-fiber Michelson interferometer and its hybridization with a human IgG is studied. Following the sensitivity enhancement strategy proposed in Chapter 3, sensitivity enhancement of the biosensor is demonstrated by reducing the radius of the cladding of the fiber as the interferometer arms.

5.2 Strategy for bio-recognition film immobilization

Immobilization of sensing biomolecule to fiber optic sensor surface is a key step in the construction of a fiber optic biosensor. Selection of immobilization strategy depends on the biomolecule to be immobilized (e.g. protein i.e. antibody, enzyme, nucleic acid, cell etc.), the nature of the immobilization substrate (fused silica in fiber

optic biosensor), and the physico-chemical transducing mechanism. A good immobilization strategy yields an appropriate immobilization density, gives strong affinity of the biorecognition molecule on the fiber surface and reserves the function of the biomolecule in biorecognition.

The immobilization strategies of biomolecule immobilization can be classified into four categories [81]:

1. physical adsorption of biomolecule in the solid phase;
2. physical encapsulation of the biorecognition molecule in host matrix, such as Sol-Gel technology;
3. chemical attachment of the biomolecule to the solid phase either directly or via a polymer metal or protein bridge;
4. covalent, site-directed attachment of the biomolecule directly to the solid phase.
5.

In our study, two types of biomolecule, i.e. ssDNA and antibody, were tested for biosensing. The immobilization strategies are thus designed for immobilization of these two molecules to the fused silica surface of the optical fiber.

5.2.1 Description of the biomolecule used in the study

a. Single strand DNA [82]

Single strand DNA is a long polymer of nucleotides. A nucleotide is a chemical compound that consists of three portions: a heterocyclic base, a sugar, and one or more phosphate groups. In DNA, the heterocyclic base is a derivative of purine or pyrimidine, which depends on the structure of the ring structure, are called Adenine (A), Guanine (G), Cytosine (C) and Thymine (T). The sugar is the pentose (five-carbon sugar) deoxyribose. A phosphate group is attached to the C-5 hydroxyl of the sugar residue in an ester (anhydride) linkage while the associate based is attached to the deoxyribose through formation of an *N*-glycosidic bond between the No.1 nitrogen of pyrimidine base or the No. 9 nitrogen of purine base and the No.1 carbon of the mono saccharide derivative. When polynucleotide is formed, the phosphate groups in turn links to the sugar group of the neighboring nucleotide through their 3′-ribosyl hydroxyl to create the backbone of the oligonucleotide polymer (see Fig. 5.2). The result is a linear sequence linked by the sugar-phosphate chain, while the four types of base unit protrude out from the backbone create the unique genetic code.

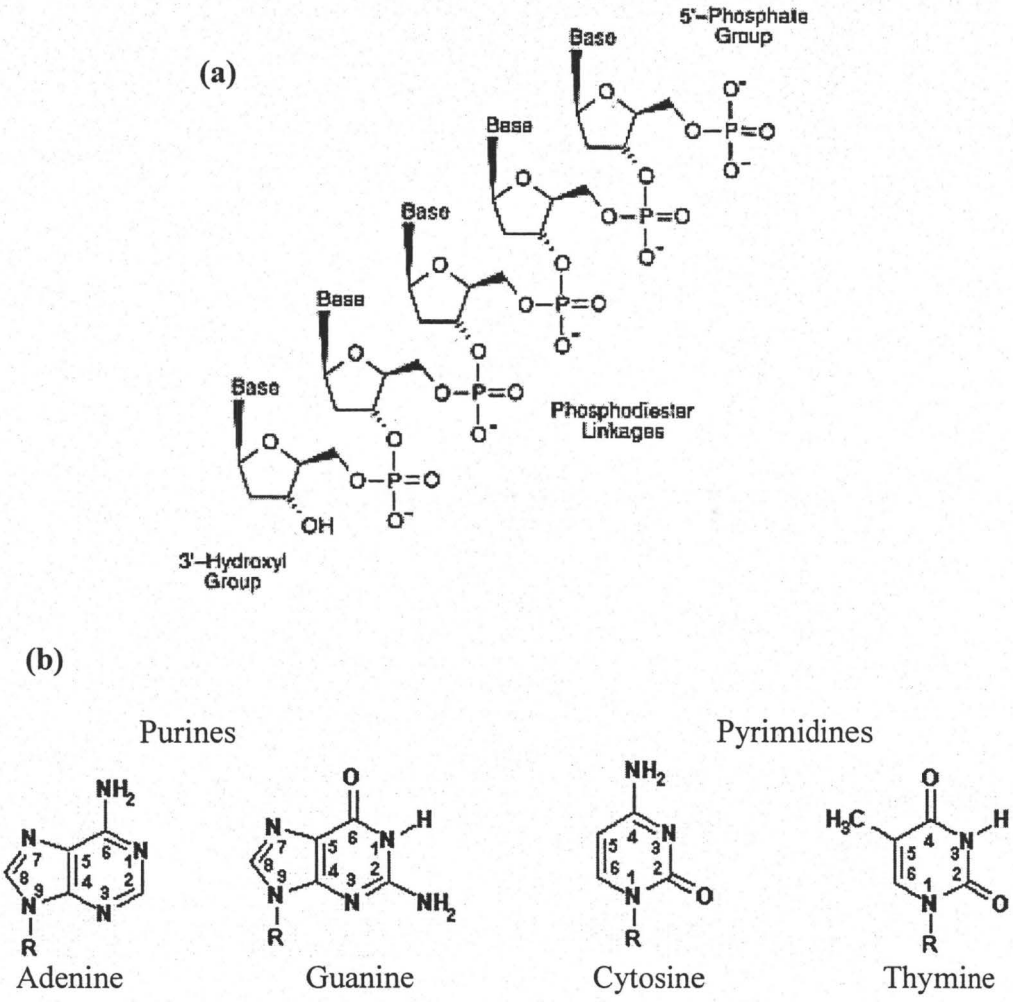

Figure 5.1 Schematic structure of (a) polynucleotide and (b) the four bases appear in ssDNA. [82]

b. Immunoglobulin G antibody [82]

Immunoglobulin G are Y-shaped proteins that are found in blood or other bodily fluids, and are used by the immune system to identify and neutralize foreign objects like bacteria and viruses. As illustrated in Fig. 5.2, the most basic immunoglobulin is composed of two light and two heavy polypeptides chains. The light chains are bond to the heavy chains in the C_L and C_H1 region by disulfide bonds, while the heavy chains are bonded with each other in the hinge regions. The tips of the Y shaped protein contain the sites which recognize specific foreign objects. This region of the antibody is called the Fab (fragment, antigen binding) region. It is composed of one constant and one variable domain from each heavy and light chain of the antibody. The base of the Y shaped protein plays a role in modulating immune cell activity. This region is called the Fc (Fragment, crystallizable) region.

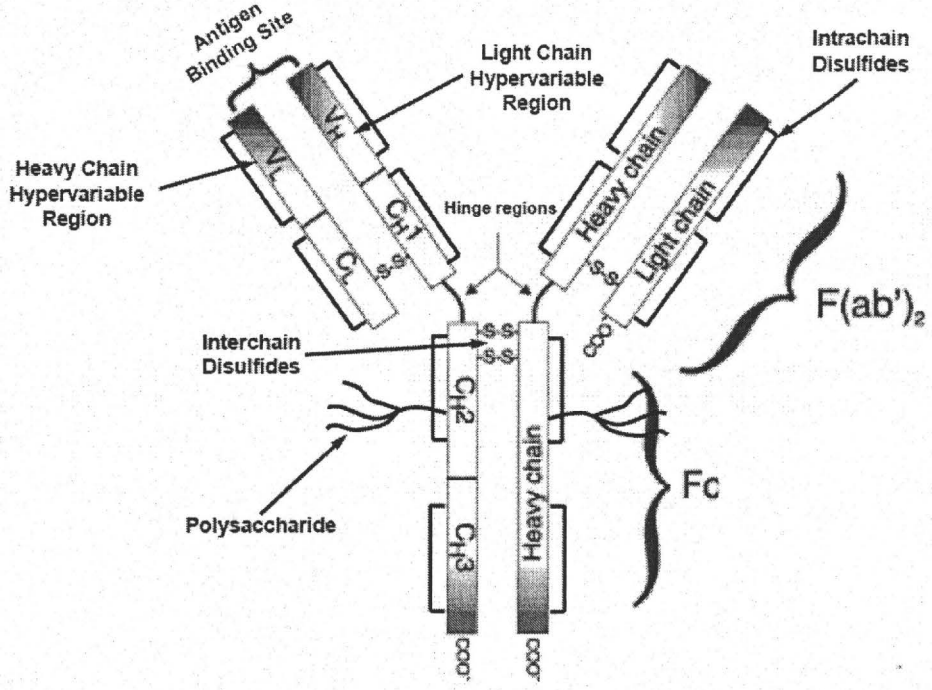

Figure 5.2 Detailed structure of an immunoglobulin G antibody molecule.

5.2.2 Surface modification of the fiber surface

To immobilize the biomolecule on the optical fiber, the fused silica surface of the optical fiber must first be chemically modified. The key here is to form a covalent bond between the organic molecule and inorganic silica surface. Usually this is done by silanize the silica surface with silane. Fig. 5.1 illustrates the principle of depositing a silane on the silica surface through hydrolytic deposition [83]. First, the alkoxy groups of the trialkoxysilanes are hydrolyzed to form silane-containing species and then condensed into oligomers. When getting in touch with silica surface, hydrogen bond is formed between the oligomers and the -OH groups on the surface of the silica. At last, in the process of drying or curing, the saline is covalently linked to the silica surface. The result is a monolayer or multilayer polysilane film covalently bonded to the silica surface with the function group exposing on the top of the film available for further modification. In this project, we use 3-aminopropyltriethoxysilane (APTs) as the silane coupling agent, which yield amino function groups on top of the silane film.

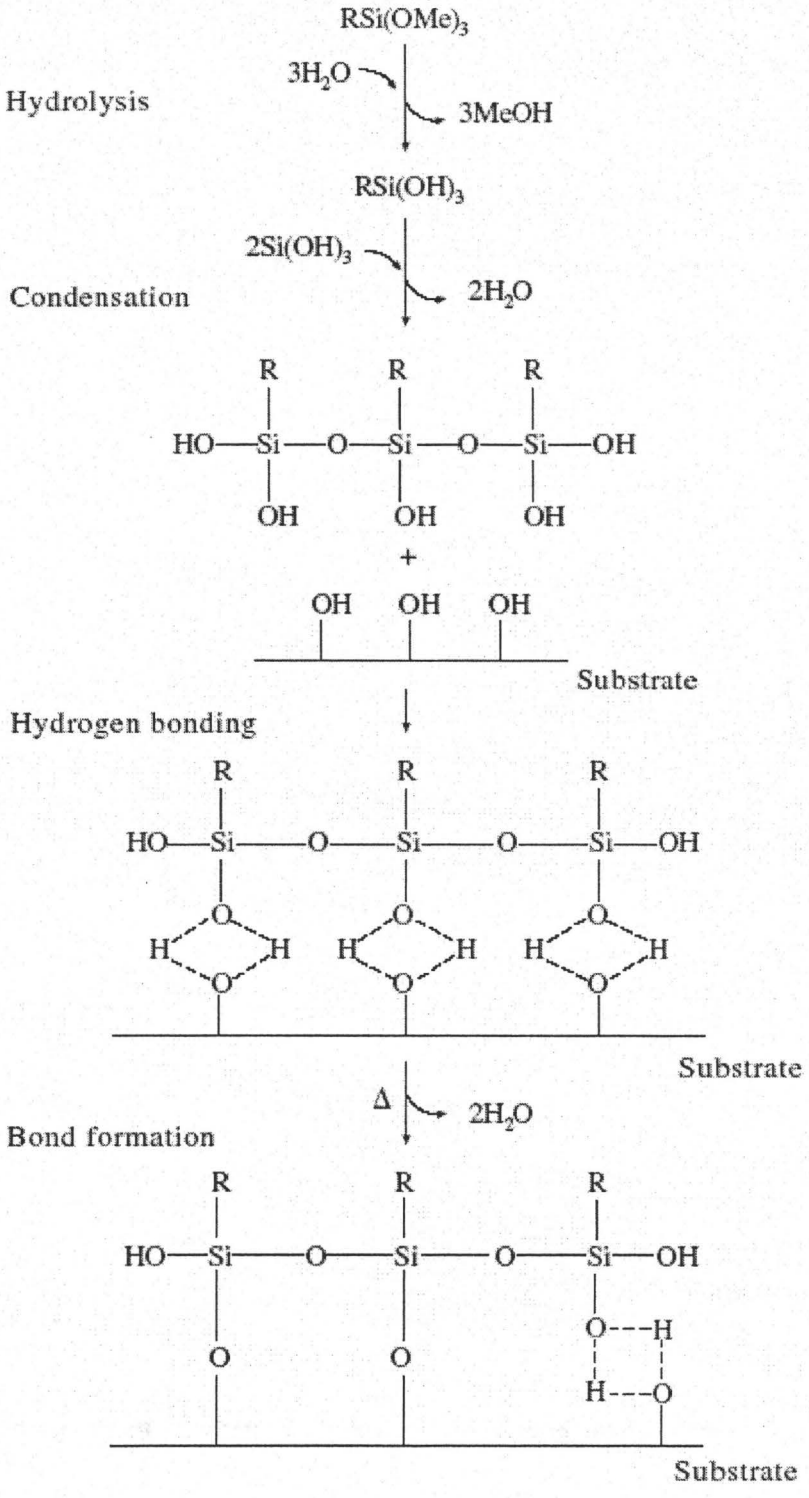

Figure 5.3 Modification of silica surface with hydrolytic deposition of silane

5.2.3 Cross link for biomolecule immobilization

Immobilization of the biomolecule on the surface modified silica surface is achieved by conjugating the biomolecule with the function group on top of the silane film. Given the difference in nature between antibody (protein) and ssDNA, the cross link used to conjugate these two types of molecules to the amino groups on the silane film are different.

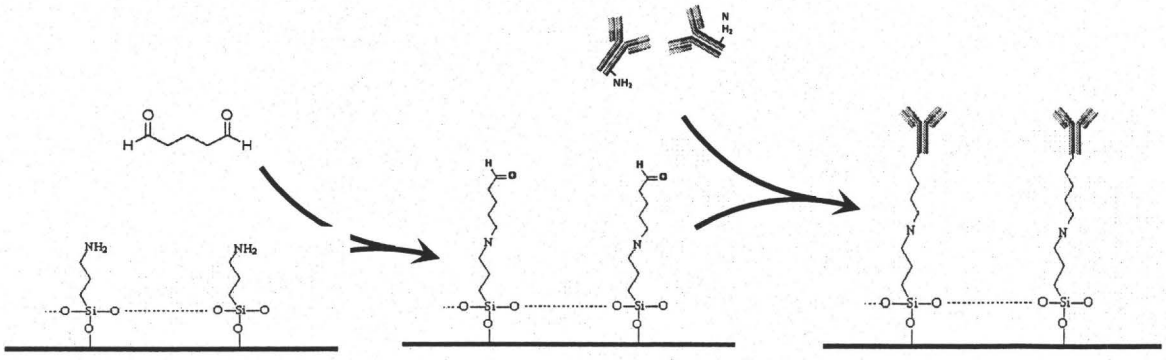

Figure 5.4 Schematic illustration of two-step conjugation of IgG on an amine modified silica surface

a. Immobilization of antibody through covalent bond

The immobilization strategy we adopted in immobilizing the antibody molecule to the silica surface utilizes the amino group on the surface of the antibody. We use a two-step glutaraldehyde-mediated conjugation to conjugate the two amino groups located on the silane film surface and the antibody surface. As illustrated in Fig. 5.4, glutaraldehyde solution is first added to the amino silane film surface, formation of Schiff based between the amine compound and the aldehyde group of at one end of glutaraldehyde happens, leaving the other aldehyde terminal of the glutaraldehyde available for further interaction. The fiber surface covered with the aldehyde groups are then incubated in antibody solution where Schiff base formation happens again and the antibodies are conjugated to the fiber surface through the amino group on its surface.

b. Immobilization of ssDNA through biotin-avidin bridge

To immobilize the ssDNA on the silica surface we utilized the biotin-avidin bridge system. In general, a biotin derivative, Sulfo-NHS-LC-Biotin (Sulfosuccinimidyl-6-(biotinamido) hexanoate), was immobilized on the surface of the silica surface, which results in an active biotin group on top of the cross link film. The fiber was then incubated in avidin solution. With high affinity to biotin, the avidin molecules were attached to the fiber surface through one of their four binding sites to biotin while leaving

others available for further reaction. To be immobilized on the silica surface through the biotin-avidin bridge, ssDNA must be conjugated with biotin before immobilization. Since the biorecognition based on ssDNA relies on hybridization between the ssDNA with its complementary oligonucleotide through hydrogen bond interaction between the base pairs, any derivation of the ssDNA should avoid modification of the base. In fact, derivatization at the 3′ hydroxyl end or the 5′ phosphate group is proved effective for minimum or no interference in hybridization. A most widely used biotinylation method is through enzymatic incorporation of a biotin-labeled deoxyuridine triphosphate (dUTP), which can be prepared from the reaction of an amin-modified dUTP with amine-reactive biotinylation regent such as Sulfo NHS-LC-biotin. Once the ssDNA is conjugated with biotin, it can be directly immobilized to the avidin through the biotin-avidin bridge.

In summary, in this section we make a brief review the biochemical nature of ssDNA and IgG. Based on their chemical composition and the surface property of silica surface, immobilization strategy of IgG through covalent bond and ssDNA through biotin-avidin is discussed.

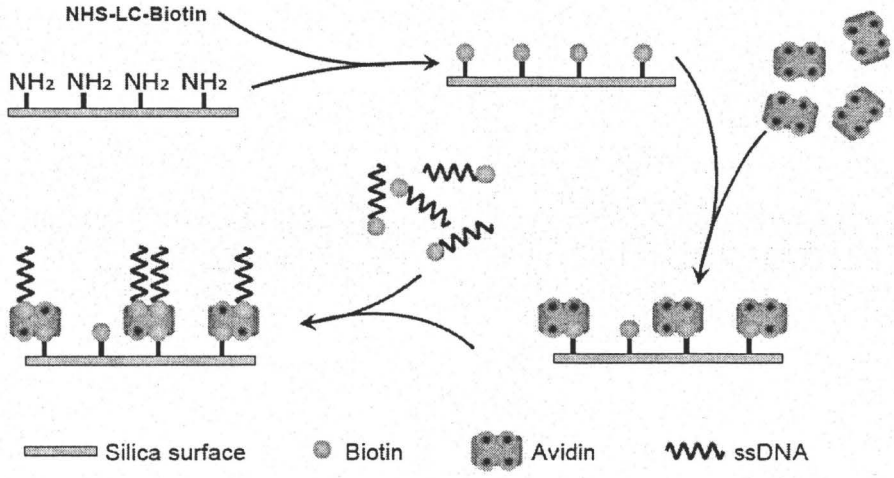

Figure 5.5 Schematic illustration of conjugation of ssDNA on an amine modified silica surface through the avidin-biotin bridge.

5.3 Fiber optic DNA sensor directly based on long period grating

After the long period grating based photonic physico-chamical transducer and the bio-recognition molecules are discussed, we now study the long period grating based fiber optic biosensor by combine the technologies described above. The most direct application of long period grating as fiber optic biosensor is to immobilize the bio-recognition molecule directly on top of the fiber cladding. DeLisa et al [53] has

demonstrated a fiber optic immunosensor by directly immobilizing Goat anti-human IgG on the fiber cladding and investigated its specific antibody-antigen binding. In this section we directly immobilize ssDNA on the fiber cladding and use it to detect the existence of its anti-sense.

5.3.1 Preparation of the long period grating

To manufacture a long period grating, Corning SMF-28 single mode fiber was hydrogen loaded at 120 bar for 14 days at room temperature. Jacket removed fiber were exposed to focused KrF excimer laser ($\lambda = 248nm$) beam through a metallic amplitude mask made of bronze. The length of the exposure area was 25mm where the period of the amplitude mask was $258\mu m$ with a modulation duty cycle of 50%. A typical exposure condition, i.e. energy 250mJ/pulse, pulse repetition rate 10Hz, was used. The transmission spectrum of the long period grating was monitored when the grating was written. Typical peak attenuation for the notch band is about 15-20dB. After the UV writing procedure, the long period grating was annealed at 110°C for 11 hours to remove the residue hydrogen and stabilize the transmission spectrum.

5.3.2 DNA Immobilization on long period grating

a. Chemicals and materials

Chemicals used in the experiments are: tween 20 (Prod # 28320), 3-aminopropyltrirthoxysilane (APTs) (Prod # 80370), Sulfo-NHS-LC-Biotin (Sulfosuccinimidyl-6-(biotinamido) hexanoate) (Prod #21335), and ImmunoPure™ Streptavidin (Prod # 21125) are from Pierce, Rockford, IL ,USA;. The fluorescent (FGG15A) and biotinylated fluorescent (BFGG15A) oligonucleotides were synthesized at W. M. Keck Facility at Yale University, New Haven, CT. The unmodified DNA PCC15A was synthesized at MOBIX Facility, McMaster University. Prior to use, the modified oligonucleotides were purified by HPLC and the unmodified oligonucleotide by 10% polyacrylamide gel electrophoresis.

b. Chemical treatment of the long period grating (LPG)

The long period gratings (LPGs) mounted on the grating holder were first ultrasonic bathed in 65% HNO_3 for 30 min, then rinsed in deionized water (DI water) to neutral pH. The LPG surfaces were then silanized for 15min in a solution containing 300mL toluene, 30μL of Tween 20, 300μL of DI water and 300μl of APTs. The silanized LPGs were then rinsed in water for 20 min. Next, the LPGs were incubated in a solution made of $0.1mg \cdot mL^{-1}$ NHS-LC-biotin in 0.1M bicarbonate buffer (pH 8.5) for 3 hours. Then the LPG was rinsed with DI water. Avidin was attached to the LPG surface by incubating the LPG in 1mL solution of $2.5mg \cdot mL^{-1}$ avidin in 50mM Tris HCl buffer (pH

8.3) for one night. The LPG was rinsed in Tris HCl buffer solution (pH 8.3) first and then in DI water to remove the unbound avidin. The gratings were then incubated in the 1 μM solution of BFGG15A ssDNA in 50mM Tris HCl buffer for 6 Hours. To confirm the avidin-biotin bridge immobilization, an oligonucleotide lacking biotin (FGG15A) was used as a control. The presence of the biotinylated fluorescent DNA BFGG15A and the absence of the non-biotinylated fluorescent DNA FGG15A on the LPG fibers was verified by fluorescence imaging. The avidin-biotin interaction was performed by exposing the fibers to 1μM BFGG15A (or FGG15A for the control) solution containing 200mM NaCl, 10mM MgCl2 and 50mM TrisHCl pH 8.3 for 90 minutes. After the DNA treatment, the LPGs were washed with the same buffer solution to remove the unbound DNA. The LPG is then air-dried, and scanned by Typhoon™ Fluorescence imager (Amersham Biosciences). The fluorescent image demonstrated 10 fold contrasts between the sample incubated with biotinynated BFFGG15A ssDNA and the sample incubated in the FFGG15A. This shows that the immobilization of the ssDNA was due to the avidin-biotin bridge, instead of the physical absorption. The LPG sensor coated with the BFFGG15A sensor layer was then incubated in the solution of the complementary ssDNA (PCC15A) solution. After that the LPG sample was rinsed in 50mM Tris HCl, pH 8.3 followed with rinsed in DI water. The sample was then air dried and ready for measurement.

c. Measurement

At each step of the LPG chemical treatment, the wavelength shift of the LPG notch band is monitored with a broadband source (BBS) and an optical spectrum analyzer (OSA). The light from the BBS was coupled to the optical fiber with a LPG inscribed in. The coupled out light wave was coupled into OSA. Because of the limited bandwidth of the BBS, only the spectrum in the 1490-1610 nm wavelength range was monitored. The transmission spectrum of the LPG sensor was recorded and analyzed with LabVIEW™ program. The central wavelength of the notch band was obtained automatically by the program. In the process of the hybridization of the ssDNA to its complimentary ssDNA, one LPG with avidin bonded on its surface was monitored at the same time as a control.

5.3.3 Experimental Results and Discussions

The experimental results of the transmission spectrum of the LPG biosensor and a LPG without DNA immobilized on its surface as the control are shown in Fig. 5.6, where the insertion is the zoom in of the bottom of the notch band. Note that signals of the DNA hybridization are modulated on wavelength shift of the absorption notch upon hybridization between BFGG15A (ssDNA) and PCC15A (cDNA), it can be found that the notch wavelength of the grating with BFGG15A immobilized on and the grating as a control both shift to longer wavelength, indicating capturing of certain molecule. By locating the center wavelength of the notch band, Fig. 5.7 shows the wavelength of the notch band of the BFGG15A immobilized LPG sensor before and after hybridization with its complementary ssDNA (Fig. 5.7a) and the wavelength of the notch band of the

LPG without DNA immobilized as a control. We found that for the LPG biosensor with DNA immobilized on the LPG surface, there is a red shift of the wavelength of 0.178 nm, while for the LPG as control only 0.03nm red shift is observed. The red shift observed with the long period grating as the control is due to the physical adsorption of the cDNA and thus been regarded as non-specific signal. Comparing the hybridization signal to the reference, such sensor demonstrates a 6-fold specific binding to non-specific binding contrast. At last it should mention that, given the broadband feature of the notch structure on the transmission spectrum (~20nm at 3dB), a notch wavelength shift of 0.178nm is very small. As a consequence, interrogation of such sensing device turns out to be a great

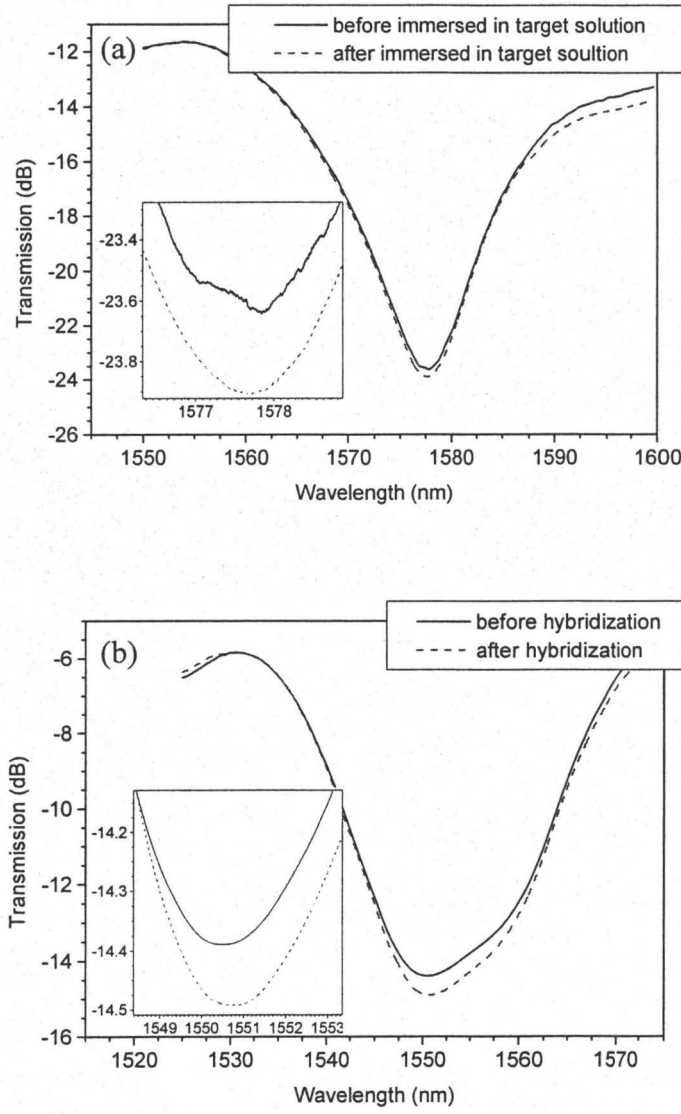

Figure 5.6 transmission spectrum of a DNA immobilized LPG biosensor (b) and a LPG without DNA immobilized on its surface (a) as the control in air before and after soaked in the solution of the target of the immobilized DNA.

challenge since intensity noise of the broadband source or the detection noise from the optical spectrum analyzer will contribute to the notch wavelength error. As has been stated in Chapter 4, the solution to this problem lies in utilizing the long period grating in-fiber Michelson interferometer as the platform, which will be given in the next section.

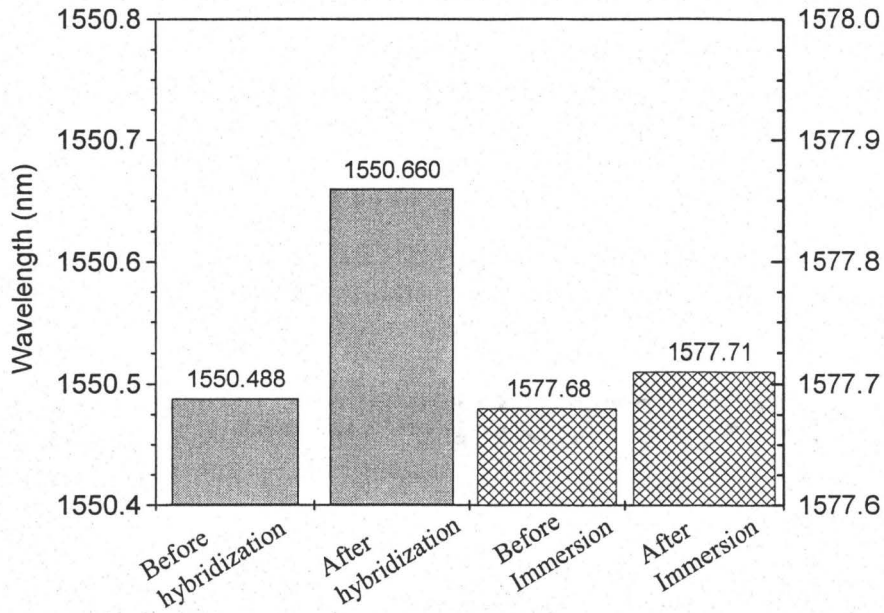

Figure 5.7. Wavelength shift of the center wavelength of the notch band of DNA immobilized long period grating sensor (grey column) and a long period grating without DNA immobilized as a control (hatched column).

5.4 Fiber optic immunosensor based on long period grating in-fiber Michelson interferometer

5.4.1. Preparation of the long period grating in-fiber Michelson interferometer

Long period gratings inscribed Corning ™ SMF-28 fiber were purchased from JC Optronics Ltd, Hong Kong. The period of the LPGs is 400 μm and grating length is 10 mm. The coupling between the HE_{11} core mode and the HE_{14} cladding mode has a coupling strength of $4.6dB$ at a center wavelength of 1525 nm. Two long period grating in-fiber Michelson interferometers were assembled following the procedure specified in Section 4.4.3. Both of the formed interferometers have an arm length of $4cm$ while the cladding diameter of one of the interferometer arms is reduced and the other is not

reduced. The axial distribution of the cladding radius of the cladding diameter reduced fiber arms has been depicted in Fig.4.18. The cladding diameter reduced fiber arms consist of three sections: a cladding unreduced section, a cladding taper and a uniform cladding diameter reduced fiber section of $10mm$, $15mm$ and $15mm$ respectively. The uniform cladding diameter reduced fiber has a cladding radius of $28.1\mu m$.

5.4.2. Calibration of the interferometer sensitivity

The Michelson interferometer sensor was characterized by measuring the reflection spectrum of the interferometer in glycerin solution. Fig. 5.8 and Fig. 5.9 show the evolution of the interference fringe and the phase shift of the interferometers respectively. When the concentration of glycerin increases, the interference fringes in the reflection spectrum shifts toward shorter wavelengths (i.e. blue shift), indicating a change in the effective index of the cladding mode as a function of the solution RI. In Fig. 5.9, the calibrated glycerin concentration-RI data is used to plot the measured fringe's shift towards shorter wavelength with ambient RI (open triangles). As a comparison, the wavelength shift of an interferometer without cladding reduction is plotted in the same figure (open circles). We theoretically calculated the effective index of the HE_{14} cladding mode as a function of the cladding radius and the solution refractive index in order to simulate the wavelength shift of the fringes. The simulation is carried out by integrating the effective index of the cladding mode over the length of the interferometer, taking into account the cladding radius profile (Fig. 4.18), and converting it to a phase shift:

$$\delta\phi(n_{amb}) = \frac{2\pi}{\lambda}\int_0^L \left[n_{eff}\left(r_{cl}(z), n_{amb}\right) - n_{eff}\left(r_{cl}(z), 1.318\right)\right] dz \qquad (5.1)$$

In Eq. 5.1, $\delta\phi(n_{amb})$ is the fringe pattern phase shift, λ is the center wavelength of the HE_{14} cladding mode resonance band. The simulation result is plotted as continuous curves in Fig. 5.9. The phase shift of the interference fringe obtained in theoretical simulation matches well with the interference fringe phase shift extracted from the experimental measurement. The long period grating in-fiber Michelson interferometer with a 28.1 μm reduced cladding radius demonstrates an averaged 10-folds sensitivity enhancement as compared to its non-diameter-reduced counterpart. It is worth mentioning that we did not reduce the fiber cladding to 20 μm as demonstrated in Chapter 4. For practical applications, a trade off was made between sensitivity enhancement, mechanical strength, and measurement stability of the interferometer.

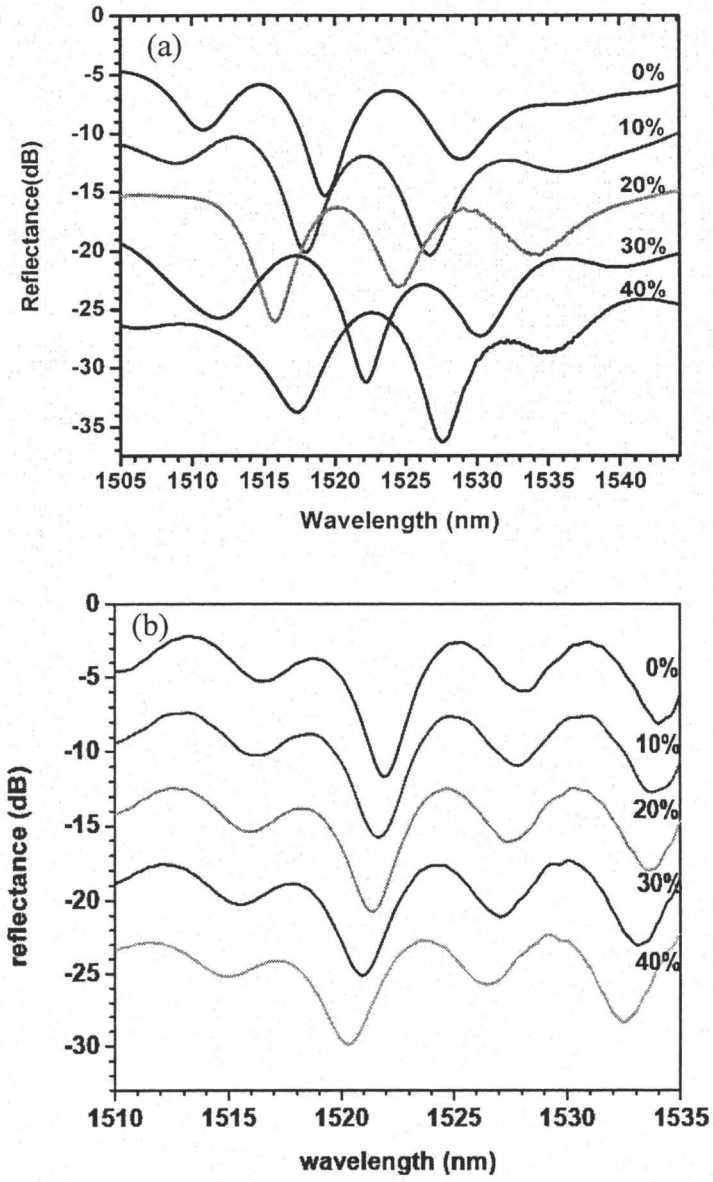

Figure 5.8 Reflection spectra of long period grating in-fiber Michelson interferometer (a) with cladding reduction and (b) without cladding reduction used in biosensor study.

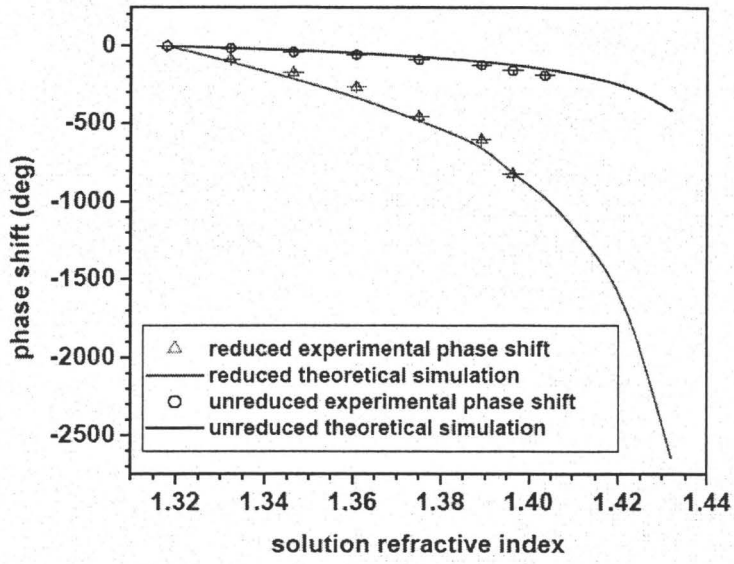

Figure 5.9 Experimental and theoretical simulation result of phase shift of in-fiber LPG Michelson interferometers with cladding diameter reduced to $28.1\mu m$ and without cladding reducing as a function of the calibration refractive index.

5.4.3. Immobilization of antibody on fiber surface and the immunoassay

a. Chemicals and materials

Sulfuric acid (Prod # 84721), hydrogen peroxide (Prod # H3410) (Tween 20 from Pierce, Rockford, IL ,USA (Prod # 28320); (3-aminopropyl)triethoxysilane (APTS) (Prod # A3648), glutaraldehyde (Prod # G4004), Human IgG (Prod # I4506), anti-Humane IgG Anti-Human IgG (whole molecule) antibody produced in goat (Prod # I4506) were purchased from Sigma-Aldrich Canada, Oakville, ON, Canada. Deioned water (DI Water) was obtained with Milli-Q® Ultrapure Water Purification Systems (Resistivity>18MW·cm). Phosphate buffered saline solution was prepared by solving Phosphate buffered saline tablet (Sigma-Aldrich Canada ,Prod # P4417) in DI water. All the regent were used as received, without further purification.

b. Immobilization of IgG on fiber surface

The long period grating in-fiber Michelson interferometers fabricated and calibrated in Section 5.4.1 and 5.4.2 were first cleaned by boiling in Pirahna solution ($H_2SO_4 : H_2O_2 = 3:1$) for 30 min followed by rinsing in DI water till pH became neutral.

The fiber interferometers were then dried in air. 2% APTs solution was prepared by dissolve APTs in 95% ethanol solution in water pH 4.5-5.5 adjusted with acetic acid. The solution was gently agitated for 5 min to allow for hydrolysis and silanol formation. The fiber interferometers were dipped in the solution for 2 min with vigorous agitation. They were then rinsed free of excess materials by dipping briefly in anhydrous ethanol, followed by curing in a convention oven (Fisher Isotemp™ Premium Lab Oven) at 110°C for 5-10 min to allow a mono layer of silane to be formed on top of the fiber surface. After the fibers were cooled down, they were treated with 1% (v/v) glutaraldehyde in water (pH 6-7) for 30 min at room temperature to modify the amino terminals on silane film into aldehyde terminals. Immediately after the terminal conversion was done, the interferometers were rinsed in 0.01 M PBS, pH 7.4 for 15min then incubated in 2 mL of $0.5mg \cdot mL^{-1}$ goat antihuman. IgG (antibody) in 0.01 M PBS, pH 7.4 overnight at 4°C to achieve the antibody immobilization on the fiber. In order to confirm the immobilization was successful, a group of bare fibers were chemical treated together with the fiber interferometers. An Enzyme-Linked ImmunoSorbent Assay (ELISA) [84] was carried out to on the bare fibers to confirm the immobilization. The result of the assay is presented in Fig. 5.10, after the fibers with the antibodies immobilized on the surface was incubated in the second antibody conjugated with horseradish peroxidase (HRP), the fibers caused a color change in the substrate. In contrast, without the covalent immobilized antibody, those fibers with physical absorbed antibody show no color change, indicating that the amount of antibody directly absorbed on the fiber surface was negligible.

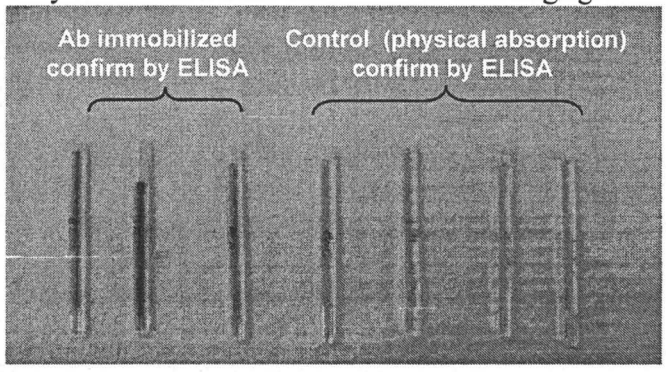

Figure 5.10 Picture of the color change of the substrate in an ELISA induced by covalently immobilized antibody on the fiber surface. The fibers with antibodies physically absorbed on the fiber surface did not cause any color change to the substrate.

c. Optical measurement setup.

The high dynamics in the biorecognition between antibody and antigen demands simultaneous measurement of the reflection spectrum of the in-fiber interferometer. In order to increase the synchronization between the two interferometers, we modified the interrogation setup shown in Fig. 4.19 to scan the two interferometers alternatively. The new experimental setup is illustrated in Fig. 5.11. An optical switch was inserted between the circulator and the interferometers. The OSA was kept scanning continuously. After each scan the reflection spectrum was recorded and the light path was switched to another

interferometer for the next scanning. After the measurement, the reflection spectra were processed and the fringe phase shift was extracted. In the whole process, the temperature variation in the laboratory was monitored to be within ±1°C to eliminate the cross interference from temperature variation.

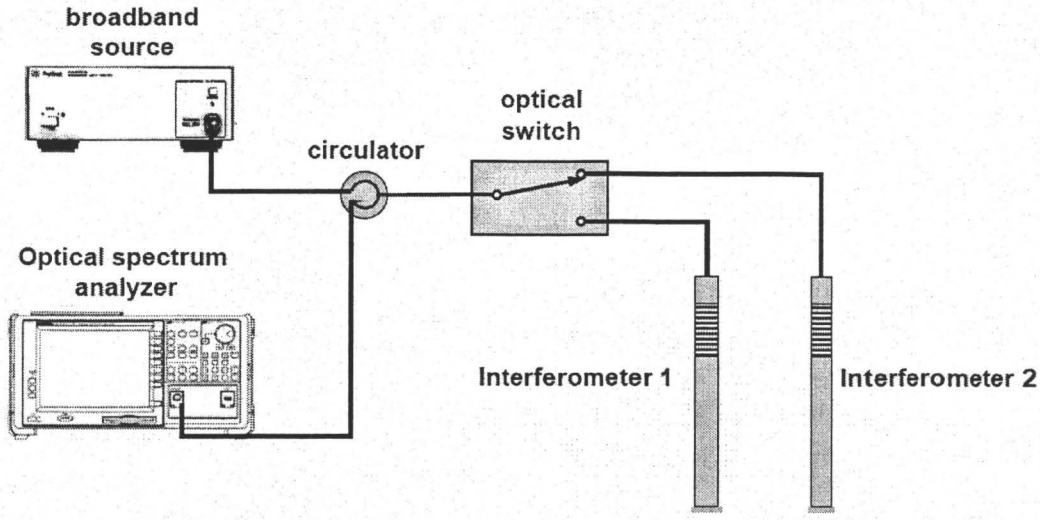

Figure 5.11 Schematic of the experimental setup for simultaneous interrogating of two long period grating in-fiber Michelson interferometers in immunoassays.

d. Immunoassays

The fiber interferometers with immobilized antibody were first soaked in $2mg \cdot mL^{-1}$ bovine serum albumin in 0.01 M PBS, pH 7.4 for 2 hours to block the free aldehyde sites not reacted with goat anti-human IgG. After blocking, non-specifc binding was tested by incubate the fiber interferometers in $50\mu g \cdot mL^{-1}$ anti-rabbit IgG solution for 2 hours. At last, specific bind was done by incubate the goat anti-human IgG immobilized fiber in human IgG.

Starting from the time point that the surface of the fiber was converted to aldehyde terminal, the interferometers were dipped into 0.01 M PBS, pH 7.4, and the reflection spectra of the interferometers were scanned for 5 times and recorded as reference. After that, five scans were made, i.e. after the antibody was immobilized, after blocking, after non-specific binding, and after the specific binding steps. After each corresponding processing, the interferometers were first rinsed in 0.01 M PBS, pH 7.4 for three times to removed the residues. Then the interferometers were inserted into 0.01 M PBS, pH 7.4 and the reflection spectra were scanned for 5 times. Fringe wavelength was then extracted from the spectrum and converted to phase shift. In the last step of the assay, where the specific binding between the immobilized goat anti-human IgG and human IgG happens, the interference fringes were recorded in real time in an alternative fashion as

has been described above. The fringe phase shifts were then plotted to study the bind dynamic of the binding.

5.4.4. Experimental results and discussions

Figure5.12 shows the fringe phase shifts of the two interferometers after each step in the immunoassays. It can be found that the interference fringes shift toward shorter wavelength at each step for interferometers with and without cladding reduction. For the interferometer with cladding diameter reduction, a wavelength shift of 0.45 nm is observed when the antibody is immobilized on top of the cladding, implying significant increases in the thickness and/or the RI of the bio-recognition film. After the sensor head surface is blocked with BSA, the observed fringe's shift towards shorter wavelength is small (0.05 nm), indicating that the density of immobilized antibodies on the sensor surface is high and only a few active aldehyde sites are available for attachment of other protein molecules. It is due to the same mechanism that the wavelength shift caused by non-specific binding to mouse IgG remains small (~ 0.05 nm). However, when the immobilized antibodies capture the antigens, the wavelength shift induced by the specific antigen-antibody binding is very large (0.9 nm), demonstrating the high specificity of the immunosensor. On the contrast, even though the phase shift of the long period grating in-fiber Michelson interferometer also shows shifts toward shorter wavelengths, the amplitudes of the wavelength shifts are much smaller (0.028 nm in Antibody immobilization, 0.011nm in BSA blocking, 0.015nm in non-specific binding and 0.106 nm respectively). Thus it is clear that by reducing the diameter of the cladding of the fiber down to $28.1\mu m$, the sensitivity of the interferometric fiber optic immunosensor is enhanced by 8.5 fold, which agrees well with the result obtained in the sensitivity enhancement calibration done with glycerin solution. To the best of our knowledge, the 0.9 *nm* fringe's shift towards shorter wavelength reported in this immunoassay study is the largest recorded for LPG in-fiber interferometric label-free biosensors.

To demonstrate the in situ assay and quick detection capability of the proposed fiber sensor, the real-time wavelength shift of the interference fringes due to antibody-antigen binding is studied. Fig. 5.13 depicts the wavelength shift as a function of the assay time. It can be seen that reducing the cladding of the interferometric fiber optic immunosensor not only shows higher sensitivity but also demonstrates faster response to the addition of the antigen. The enhancement of the detection dynamics with cladding reduction is due to the increase in the molecular motion of the antigen at the proximity of the sensor surface because of the smaller dimension of the optical fiber, which in turn boosts the binding between the antibody and antigen.

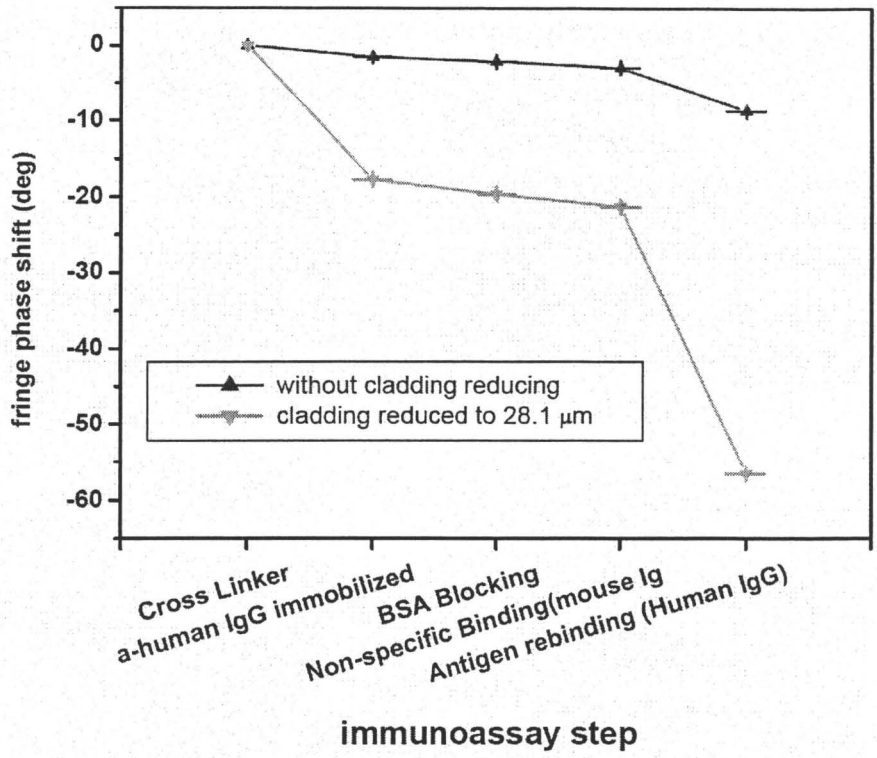

Figure 5.12 Fringe phase shift of LPG in-fiber Michelson interferometer immunosensor with and without cladding reducing at different step of immunoassay.

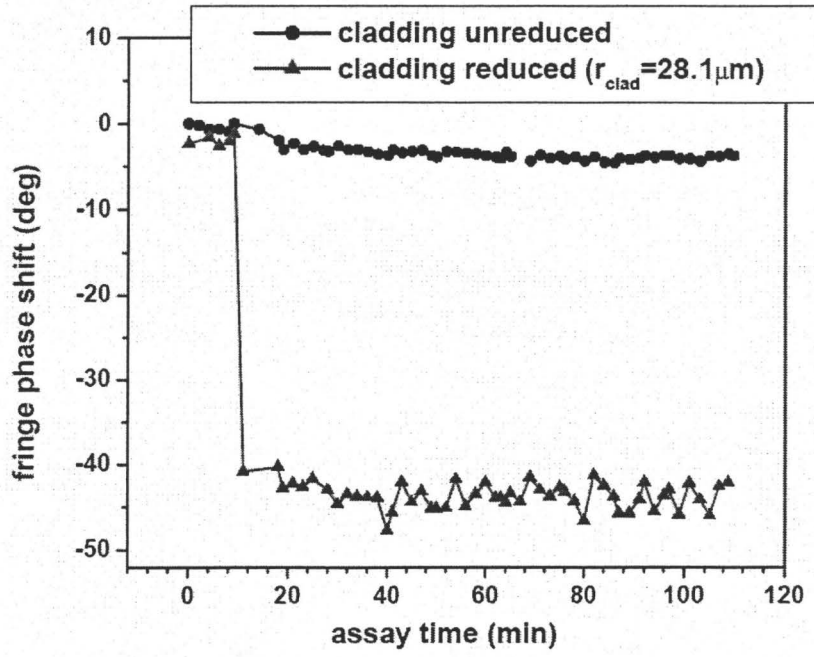

Figure 5.13. Dynamic fringe phase shift of LPG in-fiber Michelson interferometer with and without cladding reduction in immunoassay.

In summary, label-free biosensor based on long period grating photonic device has been studied in this chapter. Biorecognition molecules (ssDNA and IgG) of different chemical nature are immobilized on the surface of optical fiber with different immobilization strategy. When ssDNA is directly immobilized on long period grating, the long period grating DNA sensor demonstrates a wavelength shift of 0.178nm upon its hybridization with cDNA. This represents 6 times enhancement of specificity as compared to a long period grating without antibody immobilized on. However, due to the broadband spectrum feature of the long period grating, interrogation of the small wavelength shift of the broadband structure is a technical challenge in the measurement. By immobilizing goat anti-human IgG on the surface of long period grating in-fiber Michelson interferometers, we have demonstrated a fiber optic immunosensor. Cladding reduction has been utilized to enhance the sensitivity of a long period grating in-fiber Michelson interferometer to the changes in the ambient RI. By comparing the interferometer phase response, the proposed sensor structure demonstrates 8.5-folds sensitivity enhancement when the antibody-antigen immunosensor configuration is used.

Chapter 6

Conclusions

6.1 Summary of Research Contributions

The essential contributions of this research are to develop a fiber optic sensing platform for label-free biosensor application base on refractive index measurement of the biorecognition film. The response of the fiber optic biosensors is improved by modifying the fiber cladding structure and constructing long period grating based in-fiber Michelson interferometer.

First of all, simulation of the straight multi-layer fiber waveguide based on the full-vector model reveals that the dependence of the cladding mode effective index on the ambient refractive index is dependent on the radial refractive index profile of the fiber cladding. It has been found that by reducing the radius of the fiber cladding and thus decreasing the normalized frequency of the fiber cladding, the working condition of the cladding modes on the dispersion curve can be brought closer to the cutoff of the modes. As a consequence, the existence of the evanescent wave of the modes in the ambient medium is promoted, resulting stronger dependence of the cladding layer refractive index on the change of the ambient medium. It has also been found that application of a high refractive index overlay on top of the fiber cladding provides extra waveguiding of light wave in the fiber cladding. When the refractive index and thickness of the overlay is chosen properly, mode reorganization happens, in which the effective indices of the cladding modes moves up quickly to the value of the adjacent lower order cladding mode before mode reorganization. Study of the radial distribution of the cladding mode intensity shows that the existence of the evanescent wave in the ambient medium reaches its maximum in mode reorganization. In turn, the high refractive index overlay application brings in high dependence of the cladding mode effective index on the ambient refractive index change. As an application of the cladding mode simulation, a long period grating refractive index sensor with an overlay applied on top of radius reduced cladding was studied. By taking into consideration of the cladding mode dispersion and the cladding mode resonance condition, we suggest a new design procedure to enhance the sensitivity of long period grating refractive index sensor by simultaneously reducing the cladding diameter and applying a high refractive index overlay. By setting the long period grating period as an adaptive parameter and utilizing low order cladding mode, both enhanced sensitivity to the ambient refractive index and expanded operation range on the refractive index axis is predicted. The procedure

presented in this paper provides a guideline in the design of the high sensitivity long period grating refractive index sensor.

Secondly, a long period grating in-fiber Michelson interferometer has been studied in detail. Based on the interference between the cladding mode and the core mode in a single fiber, the reflection of a long period grating in-fiber Michelson interferometer has narrow structure in the broad notch band, which is favorable to the signal interrogation. Because the in-fiber Michelson interferometer is a single end device with the phase modulation occurring in the fiber arm, long period grating in-fiber Michelson interferometer is highly suitable for the development of disposable bio-probe. Numerical study of the interferometer characteristics shows that the spacing of the interference fringe is a dependent on the core mode and cladding mode dispersion as well as the interferometer arm length. With careful engineering, long period grating in-fiber Michelson interferometer has been constructed. The spectrum characteristic of the interference fringe obtained through theoretical simulation matches well with the parameters extracted from experimental data. Further, cladding reduction is applied to the fiber arms to increase the sensitivity of the interferometer to the refractive index change. By reducing the fiber cladding radius down to $10\mu m$, the phase shift sensitivity of a long period grating in-fiber Michelson interferometer to ambient refractive index change is enhanced by 40-fold.

At last, label-free biosensors based on long period grating photonic device have been studied. When ssDNA is directly immobilized on the cladding of a long period grating, the long period grating DNA sensor demonstrates a wavelength shift of 0.178nm upon its hybridization with cDNA. Compare to a long period grating without antibody immobilized on, this represents a 6 times of specificity. However, due to the broadband spectrum feature of the long period grating, interrogation of the small wavelength shift of the broadband structure is a technical challenge in the measurement. By immobilize goat anti-human IgG on the surface of long period grating in-fiber Michelson interferometers, a fiber optic immunosensor has been demonstrated. Cladding reduction has been utilized to enhance the sensitivity of the long period grating in-fiber Michelson interferometer to changes in the ambient RI. In comparison with the interferometer phase response of the conventional in-fiber Michelson interferometer without cladding reduction, the proposed sensor structure demonstrated 8.5-folds sensitivity enhancement when it is used in the antibody-antigen immunosensor configuration. The reported shifts are the largest obtained by an in-fiber interferometric label-free immunosensor. It has also been found that improved binding dynamics of the immobilized antibody and the target antigen can be achieved by employing the proposed biosensor, which allows detection of the target in a relatively short assay time. Thus the reported biosensor may find important applications in real-time immunoassays based on detection of fringe's shift towards shorter wavelengths.

The essential contributions of this research are to develop the techniques for optimizing the performance of the long period grating based photonic device for biosensing:

1. In parallel with other researcher, the author of this thesis independently proposed and theoretically studied utilization of high refractive index overlay on enhancing the dependence of the cladding mode effective index

on the refractive. Based on the mode reorganization induced by the high refractive index overlay, tuning of the cladding mode into the mode reorganization zone with the thickness and refractive index of the overlay is proposed to enhance the dependence of the cladding mode effective index on the surrounding medium refractive index.

2. For the first time, we proposed that reduction of the cladding underneath the high refractive index overlay increase the effective index interval between neighboring cladding mode. As a result, the effective index shift of the cladding modes in mode reorganization are enlarged, which result larger operation of the cladding mode reorganization and stronger dependence of the cladding mode effective on the surrounding medium refractive index change.
3. We first applied reduction of the cladding diameter of the fiber arm on a long period grating interferometer to enhance its sensitivity to surrounding medium refractive index change.
4. Based on the cladding reduction technique, we demonstrated a fiber optic label-free immunosensor based on antibody-antigen interaction. To the best of our knowledge, the fringe's shift towards shorter wavelength achieved in the assay is the highest wavelength shift obtained with fiber optic label-free biosensor reported.

6.2 Suggestion for Future Research

As a new sensor application, a full fiber optic bio-sensing platform needs a fiber optic sensor device, a signal interrogation system and a suitable bio-recognition system. Each of them presenting research opportunities.

6.2.1 Realization of high refractive index overlay coated fiber structure

The theoretical study of the cladding mode effective index dependence on the ambient refractive index change has revealed that the dependence can be promoted by either reducing the fiber cladding radius or by applying high refractive index. While the enhancement of the sensitivity of long period grating in-fiber Michelson interferometer to refractive index change through cladding reduction has been demonstrated in this work, application of high refractive index overlay structure has not been realized for various reasons. It has been reported that, by the layer-by-layer polyelectrolyte self-assembly technique and silver nano-particle formation, a highly uniform organic film can be realized. We consider that the reported nano-polymer film can be implemented in the proposed sensors as a high refractive index overlay and its thickness and refractive index (between 1.7 and 2.0) ca be controlled in a highly controllable fashion. With the successful formation of the overlay, further sensitivity enhancement of the long period grating based fiber refractive index sensor can be expected.

6.2.2 Development of phase carrier based interrogation system

In this research, interrogation of the in-fiber Michelson interferometer has been carried out by measuring the reflection spectrum of the interferometer with a broadband light source and an optical spectrum analyzer. Even though this method is very versatile and thus popular in laboratory, because of its slow scanning speed, limited resolution, large size and high cost, optical spectrum analyzer based interrogation technique is not practical in the application of bio-sensing. Interrogation of fiber interferometer based on homodyne demodulation [85] has been used in extracting the phase of a long period grating in-fiber Mach-Zehnder interferometer [58]. The suggested system consists of only electro optic and fiber optic component without any opto-mechanic mechanism and thus compact and low cost while having high refractive index resolution down to 10^{-6}. Given the similarity between the reflection spectrum of an in-fiber Michelson interferometer and a in-fiber Mach-Zehnder interferometer, application of the phase carrier based homodyne interrogation technique will give unprecedented performance of the system.

6.2.3 Study of biorecognition system and immobilization strategy for high sensitivity refractive index based label free sensing

At last, a long period grating in-fiber Michelson interferometer only provides a plateform for biosensing based on refractive index measurement. The performance of a fiber optic biosensor is strongly dominated by the biorecognition system and the immobilization strategy. For the evanescent wave based long period grating in-fiber Michelson interferometer, the figure of merit for choosing the biorecognition system and corresponding immobilization strategy is quite different from those of the conventional labeling based technique. In this aspect, the biochemistry and surface chemistry utilized in surface plasmon resonance technology is a good source for reference since it is very similar to the evanescent wave based sensing used in fiber sensor.

References:

[1] L. C. Clark, Jr. and C. Lyons, "Electrode systems for continuous monitoring in cardiovascular surgery," *Ann N Y Acad Sci*, **102**, pp. 29-45, 1962.

[2] Razvan Nutiu, Lieven P. Billen, and Y. Li., "Fluorescence-Signaling Nucleic Acid-Based Sensors," in *Nucleic Acid Switches and Sensors*, S. K. Silverman, Ed., 1st ed. New York, N.Y. : Springer Science+Business Media, 2006, pp. 48-74.

[3] D. R. Thevenot, K. Toth, R. A. Durst, and G. S. Wilson, "Electrochemical biosensors: Recommended definitions and classification - (Technical Report)," *Pure and Applied Chemistry*, **71**, pp. 2333-2348, 1999.

[4] M. M. F. Choi, "Progress in enzyme-based biosensors using optical transducers," *Microchimica Acta*, **148**, pp. 107-132, 2004.

[5] K. R. Rogers, "Principles of affinity-based biosensors," *Molecular Biotechnology*, **14**, pp. 109-129, 2000.

[6] C. L. Morgan, D. J. Newman, and C. P. Price, "Immunosensors: Technology and opportunities in laboratory medicine," *Clinical Chemistry*, **42**, pp. 193-209, 1996.

[7] N. K. Navani and Y. F. Li, "Nucleic acid aptamers and enzymes as sensors," *Current Opinion in Chemical Biology*, **10**, pp. 272-281, 2006.

[8] T. Vo-Dinh and B. Cullum, "Biosensors and biochips: advances in biological and medical diagnostics," *Fresenius Journal of Analytical Chemistry*, **366**, pp. 540-551, 2000.

[9] A. Hulanicki, S. Glab, and F. Ingman, "Chemical Sensors Definitions and Classification," *Pure and Applied Chemistry*, **63**, pp. 1247-1250, 1991.

[10] M. P. Byfield and R. A. Abuknesha, "Biochemical Aspects of Biosensors," *Biosensors & Bioelectronics*, **9**, pp. 373-400, 1994.

[11] S. B. Adeloju, S. J. Shaw, and G. G. Wallace, "Polypyrrole-Based Potentiometric Biosensor for Urea .1. Incorporation of Urease," *Analytica Chimica Acta*, **281**, pp. 611-620, 1993.

[12] S. B. Adeloju, S. J. Shaw, and G. G. Wallace, "Polypyrrole-Based Potentiometric Biosensor for Urea .2. Analytical Optimization," *Analytica Chimica Acta*, **281**, pp. 621-627, 1993.

[13] R. Koncki, P. Leszczynski, A. Hulanicki, and S. Glab, "Urea Sensors Based on Glass Ph Electrodes with Physically Immobilized Urease," *Analytica Chimica Acta*, **257**, pp. 67-72, 1992.

[14] T. Ruzgas, E. Csoregi, J. Emneus, L. Gorton, and G. MarkoVarga, "Peroxidase-modified electrodes: Fundamentals and application," *Analytica Chimica Acta*, **330**, pp. 123-138, 1996.

[15] X. J. Wang, S. V. Dzyadevych, J. M. Chovelon, N. J. Renault, C. Ling, S. Q. Xia, and J. F. Zhao, "Conductometric nitrate biosensor based on methyl viologen/Nafion (R)/nitrate reductase interdigitated electrodes," *Talanta*, **69**, pp. 450-455, 2006.

[16] W. Y. Lee, S. R. Kim, T. H. Kim, K. S. Lee, M. C. Shin, and J. K. Park, "Sol-gel-derived thick-film conductometric biosensor for urea determination in serum," *Analytica Chimica Acta*, **404**, pp. 195-203, 2000.

[17] S. V. Dzyadevych, A. P. Soldatkin, Y. I. Korpan, V. N. Arkhypova, A. V. El'skaya, J. M. Chovelon, C. Martelet, and N. Jaffrezic-Renault, "Biosensors based on enzyme field-effect transistors for determination of some substrates and inhibitors," *Analytical and Bioanalytical Chemistry*, **377**, pp. 496-506, 2003.

[18] C. K. O'Sullivan, R. Vaughan, and G. G. Guilbault, "Piezoelectric immunosensors - Theory and applications," *Analytical Letters*, **32**, pp. 2353-2377, 1999.

[19] R. L. Bunde, E. J. Jarvi, and J. J. Rosentreter, "Piezoelectric quartz crystal biosensors," *Talanta*, **46**, pp. 1223-1236, 1998.

[20] C. Ziegler, "Cantilever-based biosensors," *Analytical and Bioanalytical Chemistry*, **379**, pp. 946-959, 2004.

[21] K. A. Marx, "Quartz crystal microbalance: A useful tool for studying thin polymer films and complex biomolecular systems at the solution-surface interface," *Biomacromolecules*, **4**, pp. 1099-1120, 2003.

[22] C. K. O'Sullivan and G. G. Guilbault, "Commercial quartz crystal microbalances - theory and applications," *Biosensors & Bioelectronics*, **14**, pp. 663-670, 1999.

[23] F. S. Ligler and C. A. R. Taitt, *Optical Sensors: Present & Future*, 1 ed. Amsterdam: Elsevier Sciences B.V., 2002.

[24] T. H. Maiman, "Optical maser action in ruby," *Br. Commun. Electron.*, **7**, pp. 674-675, 1960.

[25] K. C. Kao and G. A. Hockham, "Dielectric-fibre surface waveguides for optical frequencies," *Proc. Inst. Electr. Eng.,*, **113**, pp. 1151-1158, 1966.

[26] A. Weber and J. S. Schultz, "Fiberoptic Fluorometry in Biosensors - Comparison between Evanescent Wave Generation and Distal-Face Generation of Fluorescent Light," *Biosensors & Bioelectronics*, **7**, pp. 193-197, 1992.

[27] T. Vo-Dinh, J. P. Alarie, B. M. Cullum, and G. D. Griffin, "Antibody-based nanoprobe for measurement of a fluorescent analyte in a single cell," *Nature Biotechnology*, **18**, pp. 764-767, 2000.

[28] J. Homola, S. S. Yee, and G. Gauglitz, "Surface plasmon resonance sensors: review," *Sensors and Actuators B-Chemical*, **54**, pp. 3-15, 1999.

[29] J. F. Masson, Y. C. Kim, L. A. Obando, W. Peng, and K. S. Booksh, "Fiber-optic surface plasmon resonance sensors in the near-infrared spectral region," *Applied Spectroscopy*, **60**, pp. 1241-1246, 2006.

[30] R. C. Jorgenson and S. S. Yee, "A Fiberoptic Chemical Sensor-Based on Surface-Plasmon Resonance," *Sensors and Actuators B-Chemical*, **12**, pp. 213-220, 1993.

[31] C. RonotTrioli, A. Trouillet, C. Veillas, and H. Gagnaire, "Monochromatic excitation of surface plasmon resonance in an optical-fibre refractive-index sensor," *Sensors and Actuators a-Physical*, **54**, pp. 589-593, 1996.

[32] J. Homola and R. Slavik, "Fibre-optic sensor based on surface plasmon resonance," *Electronics Letters*, **32**, pp. 480-482, 1996.

[33] Y. J. Rao, "Recent progress in applications of in-fibre Bragg grating sensors," *Optics and Lasers in Engineering*, **31**, pp. 297-324, 1999.

[34] S. W. James and R. P. Tatam, "Optical fibre long-period grating sensors: Characteristics and application," *Measurement Science & Technology*, **14**, pp. R49-R61, 2003.

[35] A. D. Kersey, M. A. Davis, H. J. Patrick, M. LeBlanc, K. P. Koo, C. G. Askins, M. A. Putnam, and E. J. Friebele, "Fiber grating sensors," *Journal of Lightwave Technology*, **15**, pp. 1442-1463, 1997.

[36] V. Bhatia and A. M. Vengsarkar, "Optical fiber long-period grating sensors," *Optics Letters*, **21**, pp. 692-694, 1996.

[37] H. J. Patrick, A. D. Kersey, and F. Bucholtz, "Analysis of the response of long period fiber gratings to external index of refraction," *Journal of Lightwave Technology*, **16**, pp. 1606-1612, 1998.

[38] X. W. Shu and D. X. Huang, "Highly sensitive chemical sensor based on the measurement of the separation of dual resonant peaks in a 100-mu m-period fiber grating," *Optics Communications*, **171**, pp. 65-69, 1999.

[39] Z. Y. Wang and S. Ramachandran, "Ultrasensitive long-period fiber gratings for broadband modulators and sensors," *Optics Letters*, **28**, pp. 2458-2460, 2003.

[40] X. F. Chen, K. M. Zhou, L. Zhang, and I. Bennion, "Dual-peak long-period fiber gratings with enhanced refractive index sensitivity by finely tailored mode dispersion that uses the light cladding etching technique," *Applied Optics*, **46**, pp. 451-455, 2007.

[41] K. S. Chiang, Y. Q. Liu, M. N. Ng, and X. Y. Dong, "Analysis of etched long-period fibre grating and its response to external refractive index," *Electronics Letters*, **36**, pp. 966-967, 2000.

[42] X. Chen, K. Zhou, L. Zhang, and I. Bennion, "Optical chemsensors utilizing long-period fiber gratings UV-Inscribed in D-Fiber with enhanced sensitivity through cladding etching," *Ieee Photonics Technology Letters*, **16**, pp. 1352-1354, 2004.

[43] S. C. Kim, Y. C. Jeong, S. W. Kim, J. J. Kwon, N. K. Park, and B. H. Lee, "Control of the characteristics of a long-period grating by cladding etching," *Applied Optics*, **39**, pp. 2038-2042, 2000.

[44] N. D. Rees, S. W. James, R. P. Tatam, and G. J. Ashwell, "Optical fiber long-period gratings with Langmuir-Blodgett thin-film overlays," *Optics Letters*, **27**, pp. 686-688, 2002.

[45] A. Cusano, A. Iadicicco, P. Pilla, L. Contessa, S. Campopiano, A. Cutolo, and M. Giordano, "Mode transition in high refractive index coated long period gratings," *Optics Express*, **14**, pp. 19-34, 2006.

[46] A. Cusano, A. Iadicicco, P. Pilla, L. Contessa, S. Campopiano, A. Cutolo, M. Giordano, and G. Guerra, "Coated long-period fiber gratings as high-sensitivity optochemical sensors," *Journal of Lightwave Technology*, **24**, pp. 1776-1786, 2006.

[47] A. Cusano, A. Iadicicco, P. Pilla, A. Cutolo, M. Giordano, and S. Campopiano, "Sensitivity characteristics in nanosized coated long period gratings," *Applied Physics Letters*, **89**, 2006.

[48] A. Cusano, P. Pilla, L. Contessa, A. Iadicicco, S. Campopiano, A. Cutolo, M. Giordano, and G. Guerra, "High-sensitivity optical chemosensor based on coated long-period gratings for sub-ppm chemical detection in water," *Applied Physics Letters*, **87**, 2005.

[49] I. Del Villar, I. R. Matias, and F. J. Arregui, "Deposition of coatings on long-period fiber gratings: tunnel effect analogy," *Optical and Quantum Electronics*, **38**, pp. 655-665, 2006.

[50] I. Del Villar, I. R. Matias, and F. J. Arregui, "Enhancement of sensitivity in long-period fiber gratings with deposition of low-refractive-index materials," *Optics Letters*, **30**, pp. 2363-2365, 2005.

[51] I. Del Villar, I. R. Matias, F. J. Arregui, and P. Lalanne, "Optimization of sensitivity in long period fiber gratings with overlay deposition," *Optics Express*, **13**, pp. 56-69, 2005.

[52] Z. Y. Wang, J. R. Heflin, R. H. Stolen, and S. Ramachandran, "Highly sensitive optical response of optical fiber long period gratings to nanometer-thick ionic self-assembled multilayers," *Applied Physics Letters*, **86**, 2005.

[53] M. P. DeLisa, Z. Zhang, M. Shiloach, S. Pilevar, C. C. Davis, J. S. Sirkis, and W. E. Bentley, "Evanescent wave long period fiber Bragg grating as an immobilized antibody biosensor," *Analytical Chemistry*, **72**, pp. 2895-2900, 2000.

[54] J. E. Martin, "Composite Films for Modifying Evanescent Wave Characteristics in Long-Period Grating Biosensors", Master of science,Chemical Engineering,Virginia Polytechnic Institite and State University,2001

[55] J. L. Tang, S. F. Cheng, W. T. Hsu, T. Y. Chiang, and L. K. Chau, "Fiber-optic biochemical sensing with a colloidal gold-modified long period fiber grating," *Sensors and Actuators B-Chemical*, **119**, pp. 105-109, 2006.

[56] M. E. Jones, K. A. Murphy, J. L. Elster, M. F. Gunther, and T. A. Wavering, "Single-ended long period grating optical device", US Patent. 6,275,628 1999

[57] E. M. Dianov, S. A. Vasiliev, A. S. Kurkov, O. I. Medvedkov, and V. N. Protopopov, "In-fiber Mach–Zehnder interferometer basedon a pair of long-period gratings," presented at Proceedings of European Conference on Optical Communication, Interuniversity Microelectronics Center, Ghent, Belgium, 1996.

[58] T. Allsop, R. Reeves, D. J. Webb, I. Bennion, and R. Neal, "A high sensitivity refractometer based upon a long period grating Mach-Zehnder interferometer," *Review of Scientific Instruments*, **73**, pp. 1702-1705, 2002.

[59] T. Allsop, K. Chisholm, I. Bennion, A. Malvern, and R. Neal, "A strain sensing system using a novel optical fibre Bragg grating sensor and a synthetic heterodyne interrogation technique," *Measurement Science & Technology*, **13**, pp. 731-740, 2002.

[60] P. L. Swart, "Long-period grating Michelson refractometric sensor," *Measureament Science and Technology*, **15**, pp. 1576-1580, 2004.

[61] P. L. Swart, "Athermal sensing with optical fibre Bragg gratings and long-period gratings," *South African Journal of Science*, **101**, pp. 278-281, 2005.

[62] F. F. T. Allsop, K. P. Jedrzejewski, P. V. S. Marques, R. Romero, D. J. Webb,, I. Bennion, "Spectral Characteristics of Tapered LPG Device as a Sensing Element for Refractive Index and Temperature," *JOURNAL OF LIGHTWAVE TECHNOLOGY,*, **24**, pp. 870-878, 2006.

[63] F. F. T. Allsop, K. Jedrzejewski, P. Marques, and D. W. a. I. B. R. Romero, "Refractive index sensing with long-period grating fabricated in biconical tapered fibre," *ELECTRONICS LETTERS*, **41**, 2005.

[64] J. F. Ding, A. P. Zhang, L. Y. Shao, J. H. Yan, and S. L. He, "Fiber-taper seeded long-period grating pair as a highly sensitive refractive-index sensor," *Ieee Photonics Technology Letters*, **17**, pp. 1247-1249, 2005.

[65] S. W. James, I. Ishaq, G. J. Ashwell, and R. P. Tatam, "Cascaded long-period gratings with nanostructured coatings," *Optics Letters*, **30**, pp. 2197-2199, 2005.

[66] D. W. Kim, Y. Zhang, K. L. Cooper, and A. Wang, "Fibre-optic interferometric immuno-sensor using long period grating," *Electronics Letters*, **42**, pp. 324-325, 2006.

[67] K. O. Hill, Y. Fujii, D. C. Johnson, and B. S. Kawasaki, "Photosensitivity in Optical Fiber Waveguides - Application to Reflection Filter Fabrication," *Applied Physics Letters*, **32**, pp. 647-649, 1978.

[68] G. Meltz, W. W. Morey, and W. H. Glenn, "Formation of Bragg Gratings in Optical Fibers by a Transverse Holographic Method," *Optics Letters*, **14**, pp. 823-825, 1989.

[69] K. O. Hill, B. Malo, K. A. Vineberg, F. Bilodeau, D. C. Johnson, and I. Skinner, "Efficient Mode Conversion in Telecommunication Fiber Using Externally Written Gratings," *Electronics Letters*, **26**, pp. 1270-1272, 1990.

[70] P. Yeh, A. Yariv, and E. Marom, "Theory of Bragg Fiber," *Journal of the Optical Society of America*, **68**, pp. 1196-1201, 1978.

[71] A. Bjarklev, "Microdeformation Losses of Single-Mode Fibers with Step-Index Profiles," *Journal of Lightwave Technology*, **4**, pp. 341-346, 1986.

[72] A. Yariv, "Coupled-mode theory for guided-wave optics," *Ieee Journal of Quantum Electronics*, **QE-9**, pp. 919-933, 1973.

[73] T. Erdogan, "Cladding-mode resonances in short- and long-period fiber grating filters," *Journal of the Optical Society of America a-Optics Image Science and Vision*, **14**, pp. 1760-1773, 1997.

[74] A. Cusano, A. Iadicicco, P. Pilla, L. Contessa, S. Campopiano, A. Cutolo, and M. Giordano, "Cladding mode reorganization in high-refractive-index-coated long-period gratings: effects on the refractive-index sensitivity," *Optics Letters*, **30**, pp. 2536-2538, 2005.

[75] J. W. Fleming, "Dispersion in Geo2-Sio2 Glasses," *Applied Optics*, **23**, pp. 4486-4493, 1984.

[76] T. Erdogan, "Fiber crating spectra," *Journal of Lightwave Technology*, **15**, pp. 1277-1294, 1997.

[77] D. W. Kim, Y. Zhang, K. L. Cooper, and A. B. Wang, "In-fiber reflection mode interferometer based on a long-period grating for external refractive-index measurement," *Applied Optics*, **44**, pp. 5368-5373, 2005.

[78] B. H. Lee and J. Nishii, "Dependence of fringe spacing on the grating separation in a long-period fiber grating pair," *APPLIED OPTICS*, **38,**, pp. 3450, 1999.

[79] R. M. Atkins, P. J. Lemaire, T. Erdogan, and V. Mizrahi, "Mechanisms of Enhanced Uv Photosensitivity Via Hydrogen Loading in Germanosilicate Glasses," *Electronics Letters*, **29**, pp. 1234-1235, 1993.

[80] R. J. Black, S. Lacroix, F. Gonthier, and J. D. Love, "Tapered Single-Mode Fibers and Devices .2. Experimental and Theoretical Quantification," *Iee Proceedings-J Optoelectronics*, **138**, pp. 355-364, 1991.

[81] M. Nisnevitch and M. A. Firer, "The solid phase in affinity chromatography: strategies for antibody attachment," *Journal of Biochemical and Biophysical Methods*, **49**, pp. 467-480, 2001.
[82] G. T. Hermanson, *Bioconjugate Techniques*. San Diego Academic Press, 1996.
[83] "Gelest Silane Coupling Agents," Gelest Inc. Morrisville, PA, 2004.
[84] E. Engvall and P. Perlman, "Enzyme-linked immunosorbent assay (ELISA). Quantitative assay of immunoglobulin G," *Immunochemistry*, **8**, pp. 871-4, 1971.
[85] A. Dandridge, A. B. Tveten, and T. G. Giallorenzi, "Homodyne Demodulation Scheme for Fiber Optic Sensors Using Phase Generated Carrier," *IEEE Journal of Quantum Electronics*, **18**, pp. 1647-1653, 1982.

Appendix A

LIST OF PUBLICATIONS RELATED TO THE THESIS

Refereed Journals:

[1] **J. Yang**, P. Sandhu, W. Liang, C.-Q. Xu and Y. Li, "Label-Free Fiber Optic Biosensors with Enhanced Sensitivity," Accepted (July 31, 2007) by "IEEE Journal of Selected Topics in Quantum Electronics".

[2] **Yang, J.**, Yang, L., Xu, C-Q., Huang, W. and Li, Y.. "Optimization of cladding structure modified long-period grating refractive index sensors," Journal of Lightwave Technology. **25** 372-380 (2007).

[3] **J. Yang**, L. Yang, C. -Q. Xu, C. Xu, W. Huang, and Y. Li, "Long-period grating refractive index sensor with a modified cladding structure for large operational range and high sensitivity," Applied Optics. **45**, 6142-6147 (2006).

Conference papers:

[4] **J. Yang**, P. Sandhu, W. Liang, C.-Q. Xu, and Y. Li, "Cladding Reduced Long-Period Grating In-Fiber Michelson Interferometer as Immunosensor," in *2007 Bragg Gratings, Photosensitivity and Poling Topical Meeting* (Optical Society of America, Washington, DC, 2007), BTuE5.

[5] **J. Yang**, W Liang, C.-Q. Xu, and Y. Li, "High Sensitivity Long-Period Grating Michelson Refractometer with Reduced Fiber Cladding," in *18th International Optical Fiber Sensors Conference Technical Digest* (Optical Society of America, Washington, DC, 2006), TuE93.

[6] **J. Yang**, L Yang, C.-Q. Xu, and Y. Li, "High-sensitivity refractive index sensor based on low order cladding mode resonance in long-period grating with high refractive index coating", Photonics North 2006, International Conference on Application of Photonic Technology, June 5-8, 2006, Quebec City.

[7] **J. Yang**, C.-Q. Xu, Y. Li, "Sensitivity enhanced long-period grating refractive index sensor with refractive index modified cladding layer," Photonics North 2004: Photonic Applications in Devices and Communication Systems; edited by Peter Mascher, Andrew P. Knights, John C. Cartledge, David V. Plant; Eds. Proc. of SPIE Vol. 5970 (SPIE, Bellingham, WA, 2005);

[8] **J. Yang**, Chang-Qing Xu, Razvan Nutiu, Yingfu Li, "Immobilized DNA Biosensor based on evanescent wave long period fiber gratings," Photonics North 2004: Photonic Applications in Astronomy, Biomedicine, Imaging, Materials Processing, and Education, September 27-29, 2004, Ottawa, edited by J. C. Armitage, R. A. Lessard, G. A. Lampropoulos, Proc. of SPIE Vol. 5578 (SPIE, Bellingham, WA, 2004)